Implications of ice-bedrock dynamics at Ullstorp, Scania, southern Sweden

Oscar Juliusson

Dissertations in Geology at Lund University,
Master's thesis, no 626
(45 hp/ECTS credits)

Department of Geology
Lund University
2021

Implications of ice-bedrock dynamics at Ullstorp, Scania, southern Sweden

Master's thesis
Oscar Juliusson

Department of Geology
Lund University
2021

Contents

Cover Picture: Lunch break at the study site.

Implications of ice-bedrock dynamics at Ullstorp, Scania, southern Sweden

OSCAR JULIUSSON

Juliusson, O., 2021: Implications of ice-bedrock dynamics at Ullstorp, Scania, southern Sweden. *Dissertations in Geology at Lund University*, No. 626, 53 pp. 45 hp (45 ECTS credits).

Abstract: The field of Quaternary science has, through a long history of high-quality research, produced a vast record of evidence regarding ice sheet dynamics. Consequently, our understanding of such processes and their effects are well understood. However, historically the predominant focus has been of a loose sediment perspective, which has resulted in limited insight into ice-bedrock dynamics. This is interesting due to the inherent importance of such processes for the production of loose sediment. In order to add to the knowledge and to better understand the implications of ice-bedrock interactions, a field study was conducted at a limestone quarry situated at Ullstorp, Scania, southern Sweden. At the study site, the limestone bedrock houses an expansive system of fractures with characteristic infilled material that has been determined to have formed through the process of hydrofracturing. When analysing these fractures in relation to the regional geomorphology, insights have been gained regarding the implications of ice-bedrock dynamics. First, topography seems to largely control the generation and propagation of structures and landforms that are intimately linked to subglacial water pressure. Secondly, hydrofracturing seems to exert a crucial control on bedrock liberation. In turn, this has implications for the production of loose sediments, the till continuum, and landscape evolution.

Keywords: Ice-bedrock dynamics, Hydrofracturing, Bedrock liberation, Plucking, Sediment production, Till continuum, Geomorphology
Supervisor: Dr. Sven Lukas

Subject: Quaternary Geology

Oscar Juliusson, Department of Geology, Lund University, Sölvegatan 12, SE-223 62 Lund, Sweden. E-mail: os5765ju-s@student.lu.se

Följder av interaktioner mellan inlandsis och berggrund i Ullstorp, Skåne, södra Sverige

OSCAR JULIUSSON

Juliusson, O., 2021: Följder av interaktioner mellan inlandsis och berggrund i Ullstorp, Skåne, södra Sverige. *Examensarbeten i geologi vid Lunds universitet*, Nr. 626, 53 sid. 45 hp.

Sammanfattning: Den kvartärgeologiska forskningsgrenen härstammar från en lång historia av högkvalitativa undersökningar vilket har resulterat i en omfattande kunskapsbank avseende inlandsisar och deras dynamik. Vår förståelse av dessa processer och de resulterande effekterna är därför stor. Historiskt sett har dock fokusområdet till största grad dedikerats de lösa sediment som avlagras och omarbetas i samband med dessa processer. Följaktligen är vår förståelse av interaktionerna mellan inlandsisar och berggrund begränsad. Detta är intressant med tanke på hur väsentliga de processerna är för produktionen av lösa sediment. För att bidra till förståelsen av dessa interaktioner och deras effekter har en fältstudie genomförts i ett kalkbrott beläget i Ullstorp, Skåne, södra Sverige. Där uppvisar kalkberggrunden ett omfattande spricksystem i vilket sprickorna är ifyllda med karaktäristiska sediment. Spricksystemet som kan följas genom brottet bedöms ha bildats genom hydraulisk spräckning. En påföljande analys av detta spricksystem, i förhållande till den regionala geomorfologin, har gett ökad insikt gällande effekterna som resulterar från interaktionerna mellan inlandsisar och underliggande berggrund. Resultaten visar att topografi tycks vara en viktig kontroll för initierandet och den fortsatta uppbyggnaden av strukturer och landformer som är beroende av subglaciala vattentryck. Dessutom tycks hydraulisk spräckning utgöra en viktig process som styr frigörandet av berggrund, vilket i sin tur har en stark påverkan på sedimentproduktion, sedimentkontinuet och evolutionen av landskap.

Nyckelord: Inlandsis-berggrundsdynamik, Hydraulisk spräckning, Berggrundsnedbrytning, Berggrundserosion, Sedimentproduktion, Geomorfologi
Handledare: Dr. Sven Lukas

Ämnesinriktning: Kvartärgeologi

Oscar Juliusson, Geologiska institutionen, Lunds Universitet, Sölvegatan 12, 223 62 Lund, Sverige. E-post: os5765ju-s@student.lu.se

1 Introduction

Ice dynamics and their effects on landscape geomorphology, landscape evolution, sediment assemblages and sediment characteristics is a field of research with a well-documented history (Clarke 1987; Benn & Evans 2010; Cuffey & Paterson 2010; Evans & Benn 2014a). As a result, the collective knowledge of the implications of ice dynamics within the realm of unconsolidated sediments is extensive. However, the predominant focus has historically been that of a loose sediment perspective, resulting in limited insight into the dynamics of ice bedrock interactions (Krabbendam & Glasser 2011). Even though ice bedrock interactions have been documented and described, the details of these processes have been overwhelmingly unexplored (Glasser & Bennett 2004). This is interesting considering the undeniable importance of these processes, both regarding the generation and evolution of unconsolidated sediments, as well as for landscape geomorphology and landscape evolution. This is especially true regarding bedrock liberation and its role within the till continuum (Evans et al. 1998; Evans et al. 2006b). These dynamics have only in recent years started to be appreciated within the field of Quaternary science through the works of authors such as Krabbendam & Glasser (2011), Phillips et al. (2013), Juliusson (2019), and Evans et al. (2021).

To understand the processes related to ice-bedrock dynamics, the subglacial environment in which they operate needs to be considered. The subglacial realm contains a vast array of processes that gives rise to an equally vast array of depositional environments and sedimentary structures. This results in a complex mix of processes, all that work towards mobilization and final deposition of sediments. This includes processes such as deformation, sliding, lodgement, flow, and ploughing, just to name a few (Evans et al. 2006b). Due to the complex imprints exerted by the different processes and their extensive spatial and temporal variability, glaciologists have started to move away from the traditional process-specific description method to instead adopt a more encompassing mosaic model of the process-continuum operating within the subglacial realm (Piotrowski & Kraus 1997; Boyce & Eyles 2000; van der Meer et al. 2003; Piotrowski et al. 2004; Evans et al. 2006b; Lee & Phillips 2008; Meriano & Eyles 2009). These models have been shown to constitute an important tool, as the traditional process-specific classification approach within the subglacial continuum has proven virtually impossible to implement (Evans et al. 2006b). These models have further served to introduce the concept of subglacial traction till, which attempts to better encompass the conceptual models regarding subglacial till deformation (Fig. 1) (Evans et al. 2006b). In turn, this has highlighted the dynamics and importance of water pressure within the subglacial realm.

Subglacial water pressure, or more precisely the degree of porewater pressure (Boulton et al. 2001), exerts a controlling factor that determines the characteristics of the aforementioned encompassing models. Higher porewater pressures are believed to weaken electrostatic bonds between sedimentary particles, leading to increased distances between clasts, sediment dilation, porewater migration, and consequently a reduction of the cohesive and frictional strength of the material (Evans et al. 2006b). This creates an active zone of displacement where sediments are more easily mobilised during shear (Fig. 1) (Dowdeswell 1993). In turn, this correlates with the findings that finite strains within subglacial sediments are much lower than initially expected (Evans et al. 2006b). An insufficient drainage system within the subglacial environment would result in an increase of porewater pressures and possibly cause the water-saturated sediments to enter a liquified state. Such conditions would entail a major increase of the sediment volume and a major decrease of its cohesive and frictional strength (van der Meer et al. 1999; Evans et al. 2006b). The idealized distribution of porewater content and subsequent porewater pressure display a gradual increase from the sediment-bedrock interface towards the sediment-ice interface. This is coupled with increased deformation due to the progressive degradation of a coherent till-matrix framework due to increasing porewater pressure (Fig. 1) (Evans et al. 2006b).

Porewater pressures have been shown to have a dramatic effect on both unconsolidated sediments and bedrock within the subglacial realm. If elevated porewater pressures are coupled with inhibited porewater migration due to impermeable material, e.g. impermeable sediments, bedrock, or permafrost, the pressure conditions can become unsustainable and initiate the process of hydrofracturing (Åmark 1986; van der Meer et al. 1999). Hydrofractures, also referred to as clastic-dykes and water escape features, form in response to marked fluctuations of the hydrogeological system within the subglacial realm, as porewater pressure exceeds the tensile strength of the host sediment/rock (Ravier et al. 2015). They form through fracturing and pene-contemporaneous widening and filling of the fracture (Phillips et al. 2013), described by Larsen & Mangerud (1992) as instantaneous cut and fill. These features have been documented in both unconsolidated sediments and bedrock within both glacial and palaeo-glaciated settings (Åmark 1986; Phillips et al. 2013; Ravier et al. 2015). Furthermore, depending on the degree of consolidation and history of the host sediment/rock, closed fractures may constitute pre-existing features. In such instances, these pre-existing planes of weakness are reactivated by the elevated hydrostatic pressures associated with hydrofracturing (Phillips et al. 2013). Hydrofractures can propagate as dykes either downwards (*per-*

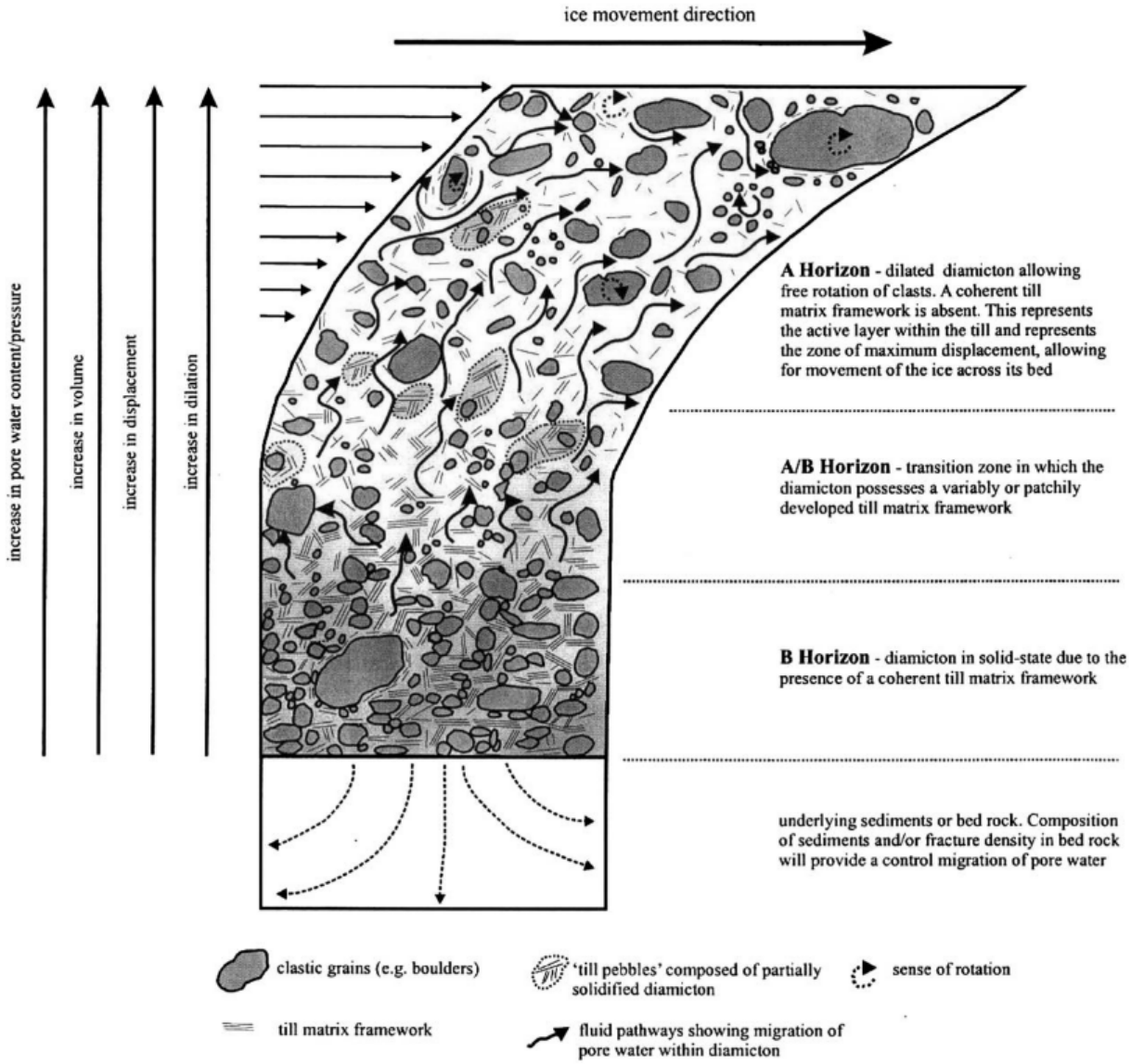

Figure 1: Idealised construction of a subglacial deforming till layer with associated development of porewater migration pathways, till-matrix framework, till pebbles, and the relationships of these factors with regards to horizon development and geotechnical properties (Evans et al. 2006b).

descensum), upwards (*per-ascensum*) or laterally as sills (van der Meer et al. 2009; Ravier et al. 2015). Field studies have shown that hydrofracture propagation follows a typical pattern which in turn has resulted in conceptual models for hydrofracture generation and propagation within glacial environments (Fig. 2). These illustrate how differential loading by overlying ice exert the primary control on hydrofracture propagation and fluid migration within the subglacial to proglacial system, as a response to diminishing ice-thickness towards the ice-margin (Piotrowski 2007; Phillips et al. 2013; Ravier et al. 2015). The infilled material in hydrofractures display characteristic structures. These typically exhibit varying laminations of different grain-sizes that are evenly distributed across the width of the hydrofracture, i.e. coarser grain-sizes concentrate in the middle of the fractures whilst finer material concentrate along the fracture walls and tip. This is due to the inherent difference in erosion and sedimentation dynamics of different grain-sizes during elevated porewater pressures (Phillips et al. 2013; Ravier et al. 2015). However, this typical lamination structure can be deformed due to repeated episodes of hydrofracturing with concomitant infill (Phillips et al. 2013).

As presented above, ice-bedrock dynamics undoubtedly have the potential to exert a major influence on bedrock characteristics. However, the implications of such dynamics remain largely unexplored, especially regarding bedrock disintegration, bedrock plucking, and the influence on the till continuum. Therefore, this study is dedicated to the exploration of the implications of ice-bedrock dynamics through the investigation of the bedrock-sediment transition zone at the limestone quarry, commonly known as *Kalkan*, located at Ullstorp, Scania, southern Sweden. The

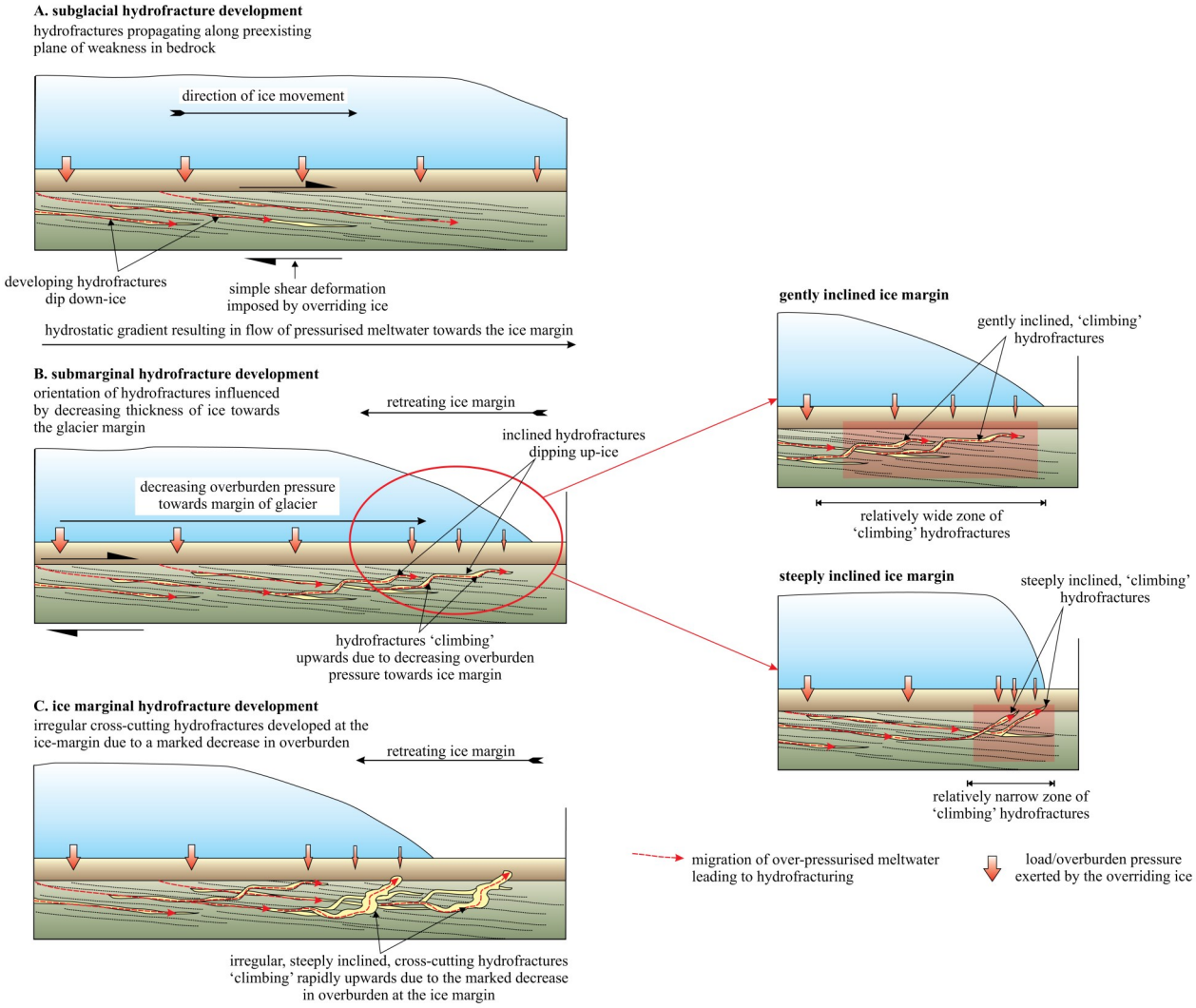

Figure 2: Conceptual model of hydrofracture propagation within subglacial to proglacial environments. a) Down-ice propagation of hydrofractures along pre-existing planes of weakness. b) Hydrofracture orientation influenced by reduced overburden pressures exerted by the ice, showing differences between gently and steeply inclined ice margins. c) Cross-cutting hydrofractures resulting from marked decrease in overburden pressure (Phillips et al. 2013).

quarry-related activity at the study site has resulted in an exposure of the local transition zone and this paper aims to investigate the contact and relation between the bedrock and overlying sediments to:

a) Record the sedimentological and structural evidence.

b) Identify the processes that have acted at the study site.

c) Analyse these findings in relation to the regional geological setting.

d) Discuss the importance of the results with regards to the implications of ice-bedrock dynamics.

2 Study area & study site

The study area is situated in the east of Scania and is roughly 55 x 47 km in size (Fig. 3). Within this area, the study site is situated in the limestone quarry commonly known as *Kalkan* at Ullstorp, Scania, southern Sweden, roughly 13 km WNW of Kristianstad. The coordinates of the exposure at the study site are latitude 56.062586 and longitude 13.955468 (Fig. 4). The study site is situated directly down-slope of the Nävlingeåsen Horst that is located SW of the quarry. The quarry itself is approximately 200 x 300 m in size and the exposure is situated in the SW quarry wall (Fig. 4).

2.1 Geological conditions

The regional and local geology of the study site is presented below. First, the regional bedrock conditions are addressed, followed by the local bedrock conditions of the study site. Secondly, the Quaternary geolo-

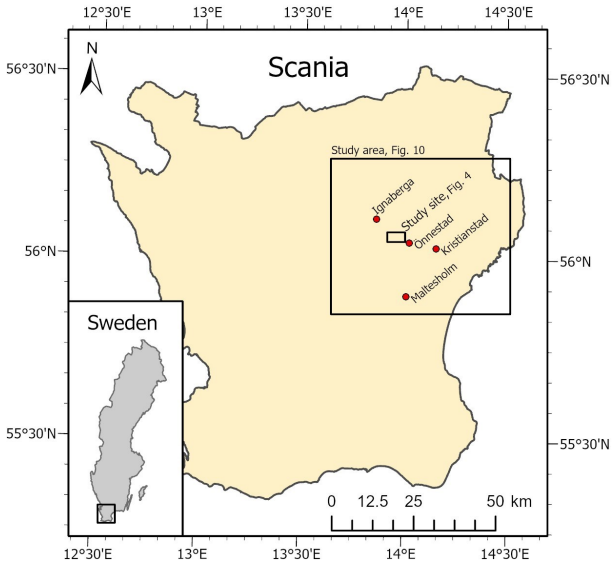

Figure 3: Situational map showing the extent of the study area, study site, locations mentioned in the text, and major neighbouring cities.

gy is addressed with regards to palaeo-ice-flow, stratigraphy, and sediment distribution. Additionally, the characteristics of the major Quaternary deposits are addressed. It is worth noting that the vast majority of the geological record for the area has been compiled by Ringberg (1991) and thus, the following information is heavily based on his work.

2.1.1 Regional bedrock conditions

The bedrock in the area consists of two major distinct terrains, an igneous/metamorphic terrain and a sedimentary terrain comprising the Kristianstad Basin (Fig. 5) (Ringberg 1991). The sedimentary bedrock in the area consists mainly of successions of Cretaceous limestone with a spatially varying degree of consolidation, loose sandstone, and layers of glauconite sand. The limestone primarily consists of muscle, shell, octopus, and sea urchin remnants (Ringberg 1991).

There are also local occurrences of residual kaolinite, formed by weathering of the local gneisses and granites. Kaolinite also occurs as reworked clay formed through erosion and reworking of residual kaolinite during the younger Cretaceous (Ringberg 1991). The kaolinite deposits contain varying amounts of gneiss and granite source clasts and are most readily found at the ground surface along the outer edges of the limestone deposits (Ringberg 1991).

There are two groups of dolerite dykes running through the area. The first group of dykes has a NW-SE orientation (Fig. 5). These dykes consist of dark-grey fine-grained material with associated quartz veins. The dykes are steep and reach thicknesses of up to 15 m. Only dykes readily visible in field have been mapped by Ringberg (1991) (Fig. 5) but he states that aeromagnetic measurements have revealed a large amount of additional dykes. The other collection of dolerite dykes has a SW-NE orientation. These consist of black fine-grained (< 1 mm) material in the smaller dykes and coarser grains (> 5 mm) in the wider dykes (Ringberg 1991).

To the NE the bedrock consists of fine-grained reddish-grey granite with local augen structures of microcline (Fig. 5). This granite is fairly homogenous and lacks fractures (Ringberg 1991). Bodies of coarser granite are also present. These consist of medium-grained reddish-grey material with augen structures of feldspar and are generally free of minor fractures (Ringberg 1991).

Within the area there are two distinct types of gneiss, fine-grained gneiss, and medium-grained gneiss (Fig. 5). Large parts of the surrounding area consist of fine to fine-medium-grained gneiss of granitic to granodioritic origin that sporadically display augen structures of microcline. The gneiss is fairly fracture resistant with the exception of the highly tectonic areas such as the Linderödsåsen and Nävlingeåsen Horsts (Ringberg 1991). To the NW, there is a segment of veined gneiss characterised by dark, fine-grained, hornblende-rich material that display a high degree of schistosity. In addition, it contains veins of gneiss-granite, granite, and pegmatite. This segment is characterised by zones of weakness and fractures at granite borders (Ringberg 1991). Lastly, there are bodies of fine-grained greyish-red gneiss, mainly located in the SW and NE. Along the Linderödsåsen Horst, this gneiss has a strong fracture imprint (Ringberg 1991).

2.1.1.1 Local bedrock conditions

The bedrock underlying the loose sediments within the Kristianstad Basin primarily consists of Cretaceous Campanian limestone (Fig. 5). It is worth noting that the following information is predominantly derived from Sandström (2001) who conducted a case study describing the Campanian depositional environment of a limestone quarry situated at Maltesholm (Fig. 3). However, Sandström (2001) describes that the same type of deposits are found at Ullstorp. Thus, the Campanian deposits described by Sandström (2001) are here considered equivalent to those of the study site.

The deposits are predominantly coarse-grained, poorly consolidated, ruditic grainstones with interbedded clay horizons. The grainstones mainly consist of coralline algae and quartz whilst being predominantly free of micrite and lime mud (Sandström 2001). The abundance of coralline algae and lack of micrite is indicative of a shallow, nearshore, high energy depositional environment (Erlström & Gabrielson 1986). In addition, two other main facies are distinguishable, i.e. fair weather facies containing abundant rudists and storm weather facies containing pebble and shell fragment conglomerates displaying scour and fill structures as well as hummocky crossbedding. Three types of conglomerates are defined within the Campa-

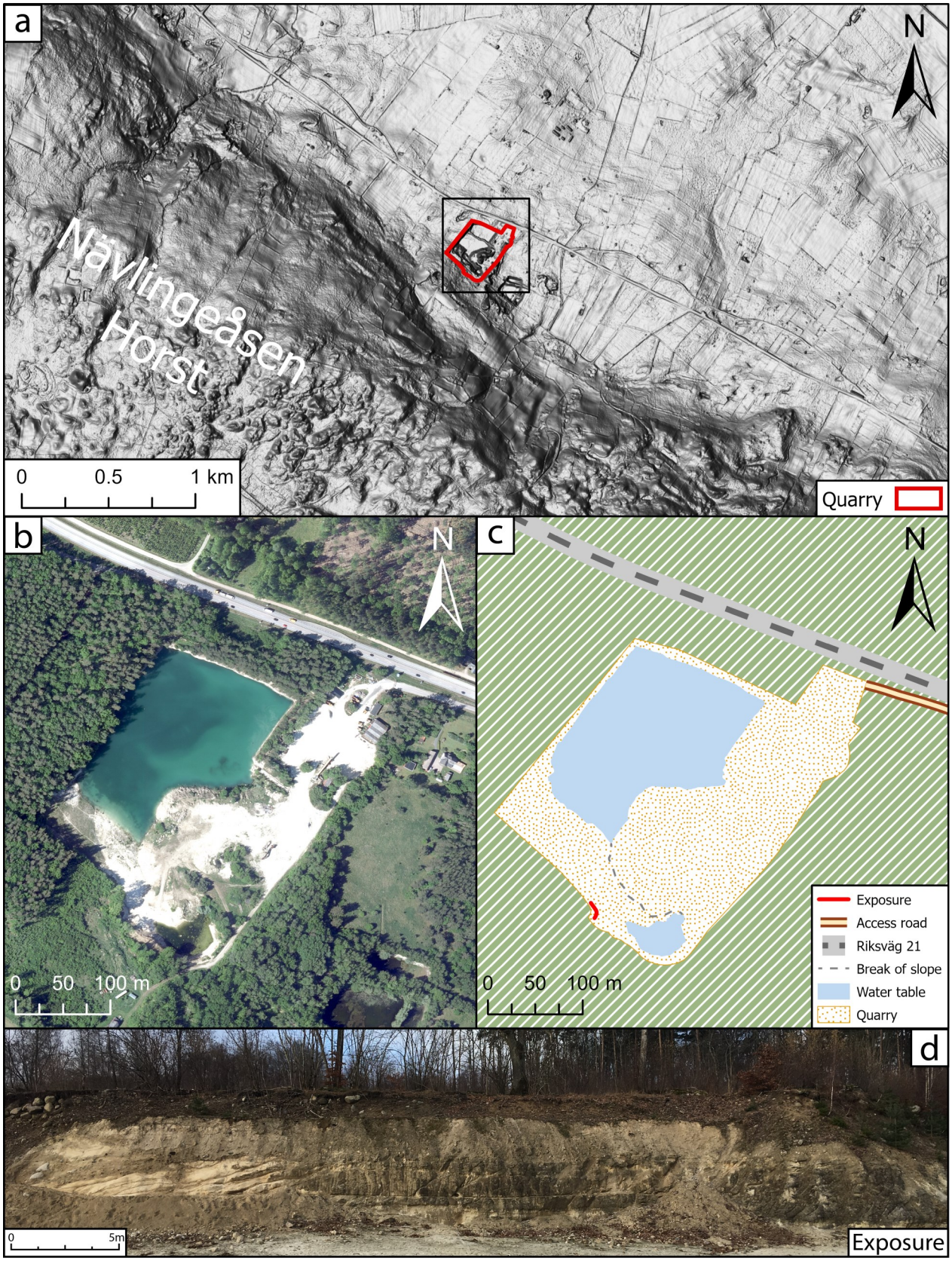

Figure 4: Situational maps of the quarry housing the investigated exposure, produced with data from the Swedish government agency Lantmäteriet (n.d.). a) A multidirectional hillshaded DEM with a 10X vertical exaggeration indicating the spatial relationship between the quarry and the Nävlingeåsen Horst. b) Orthophoto from 2019 showing the extent and structure of the quarry. c) Simplified layout map of the quarry displaying the location of the exposure and major surrounding features. d) Photograph of the exposure located at the study site.

nian deposits, i.e. pebble, intraclast, and shell fragment conglomerates (Hadding 1927; Lundegren 1934; Erlström et al. 1992; Sandström 2001). The pebbles in the conglomerate are well rounded and originate from Precambrian rocks, limonite nodules, and quartz. The fill between clasts is predominantly of the same material as the surrounding limestone, which consists of poorly consolidated calcirudites. The conglomerates often occur in association with hardgrounds (Sandström 2001). Palaeocurrent data derived from belemnite rostra are indicative of a NE or SW oriented storm driven current direction, which in turn is oriented perpendicular to an inferred shoreline (Sandström 2001).

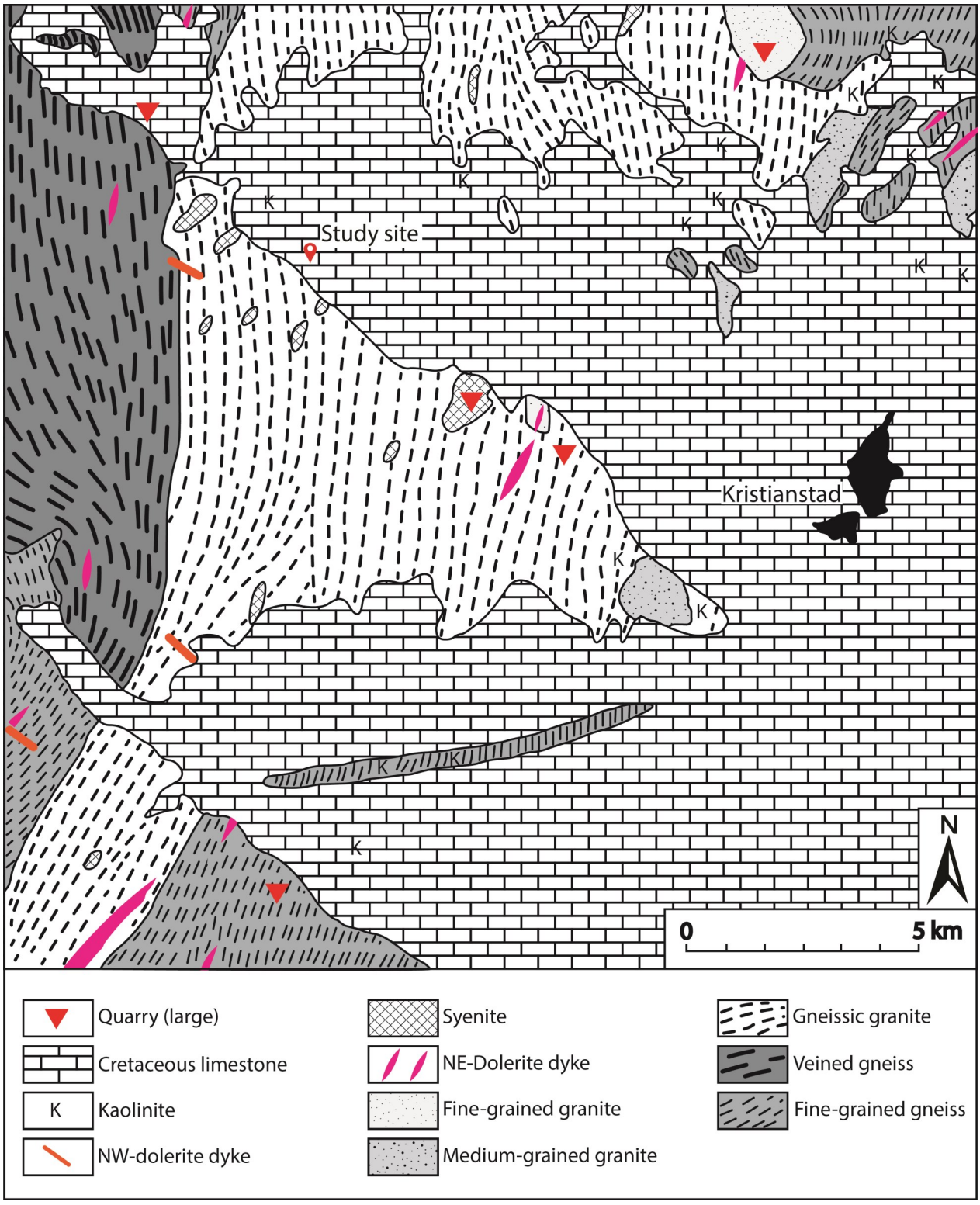

Figure 5: Spatial distribution of the Pre-Quaternary bedrock. Modified from Ringberg (1991).

2.1.2 Regional Quaternary conditions

2.1.2.1 Palaeo-ice-flow indicators

Palaeo-ice-flow directional structures have a long history of being studied within the regional area and have been studied by researchers such as Lindström (1877), Karlsson (1879), and De Geer (1889). Ringberg (1991) describes two generations of striae indicative of the palaeo-ice-flow directions in the area (Fig. 6). The younger striae exhibit a general direction from the NE (10°-30°) on the southern flank and middle section of the Nävlingeåsen Horst and from the NE (5°-20°) at its NE slope and further towards the NE. The exposed bedrock containing these striae is described by Ringberg (1991) to have generally defined, smooth, and well-rounded stoss-sides towards the NE and defined steeply plucked lee-sides in the opposite direction to-

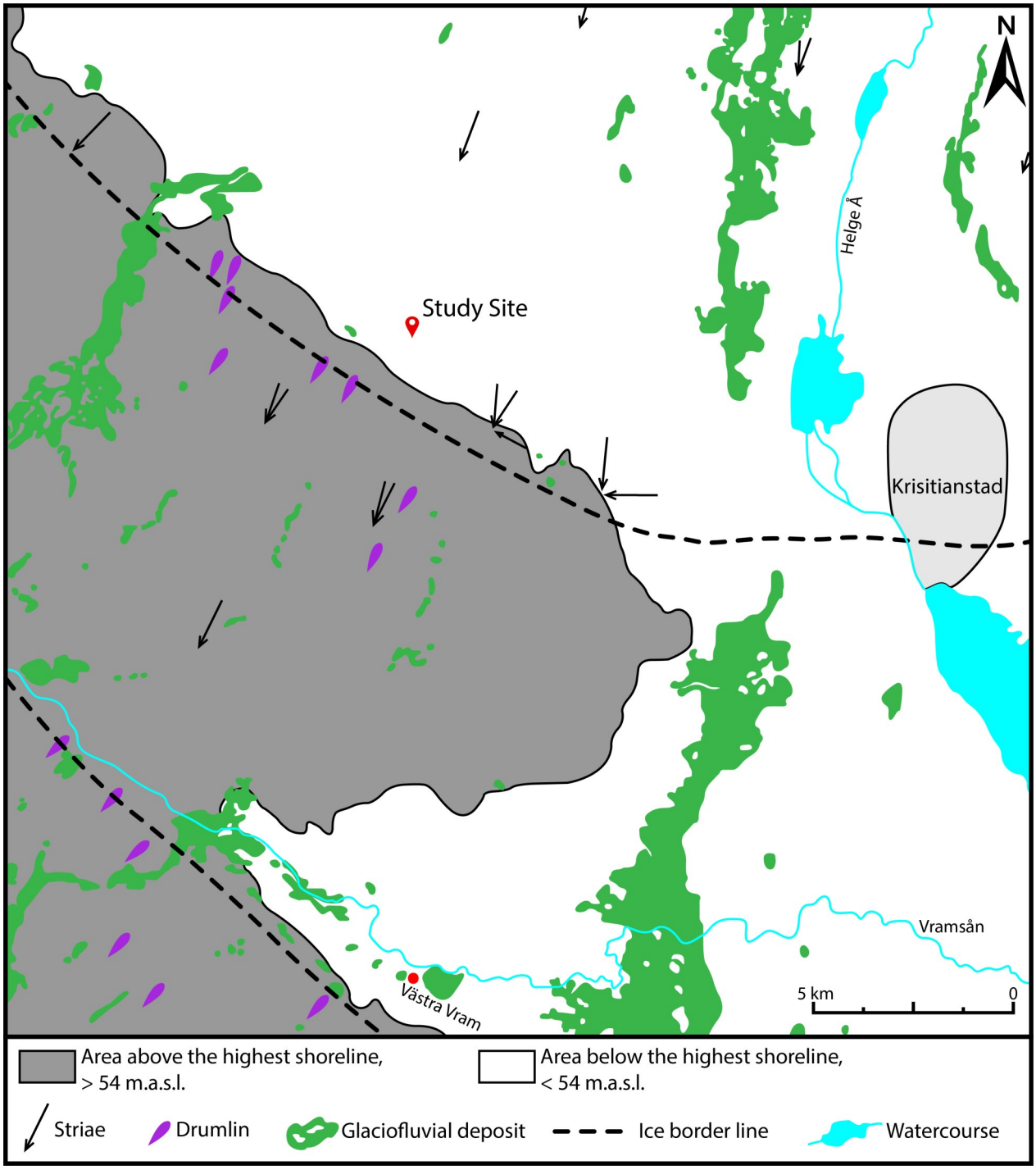

Figure 6: Map of the area surrounding the study site displaying the spatial distribution of areas above and below the highest shoreline. In addition, the location and spatial orientation of striae, drumlins, glaciofluvial deposits, watercourses, and locations of interest are marked. Modified from Ringberg (1991).

wards the SW. The older generation of striae has a E-W or WNW-ESE direction. In addition, Ringberg (1991) describes that the area exhibits drumlins with a similar orientation to the younger generation of striae and it is worth noting that the glaciofluvial deposits also share this orientation (Fig. 6). However, how the relative ages of the striations were determined is not presented by Ringberg (1991).

Analysis of elongated medium-sized sand particles deposited as part of a subglacial till during active ice movement also gives an indication of the palaeo-ice-flow direction in the area. Ringberg (1991) analysed such particles in an exposure situated at Tollarp, 1.3 km ENE of Västra Vram church (Fig. 6). The analysis of particle a-axis orientations display a trend towards the NE (Fig. 7). The orientations of these particles are thus consistent with a palaeo-ice-flow direction from the NE (Ringberg 1991), which is coherent with most of the glacial landforms and structures mentioned above. However, the methods used to measure the orientations of these particles are not mentioned by Ringberg (1991). This is interesting due to the inherent difficulty of conducting structural measurements of a-axis orientations of particles that size.

2.1.2.2 Quaternary sediments, thicknesses & stratigraphy

The sediment thickness within the area surrounding the study site has been described by Ringberg (1991) as highly variable. Upon the Linderödsåsen Horst the thickness typically lies between 0 and 5 m, rarely exceeding 10 m. Upon the Nävlingeåsen Horst, the thickness lies between 0 and 10 m but reach thicknesses of 15-25 m within local fractures. Within the igneous bedrock area north of the Kristianstad Basin (Fig. 5) the sediment thickness ranges between 0 and 10 m but can locally reach 15 m (Ringberg 1991). In these areas the stratigraphy typically consists of till deposited on the igneous or metamorphic bedrock, which in turn is locally overlain by glaciofluvial sediments. These glaciofluvial deposits can also be found directly overlying the igneous/metamorphic bedrock in certain areas (Ringberg 1991).

The greatest sediment thicknesses are recorded within the area of the Kristianstad Basin (Fig. 5) below the highest shoreline, which is situated 50-55 m.a.s.l. (Fig. 6) (Agrell 1976; Ringberg 1991). These sediments typically reach thicknesses of 10-20 m but thicknesses of 40-65 m have been reported (Ringberg 1991). Within the extent of the Kristianstad Basin, beneath the highest shoreline, the stratigraphy often consists of the aforementioned limestone with an upwards progression series of till, glaciofluvial sediments, glacial fines/clay, and sediments reworked by wave action at the top (Ringberg 1991). Sediment cores have shown that up to three distinct till deposits, separated by clay, silt, sand, or gravel, overlie the limestone bedrock within the basin. The cores also show that the glaciofluvial deposits often directly overlie the limestone (Ringberg 1991).

The dominant sediment type within the area surrounding the study site is till, as described by Ringberg (1991). As shown by sediment cores, these sedimentary bodies range in thickness from 0.5 to 55 m, where the thinnest deposits coexist with exposed bedrock. These thinner deposits, typically 5-10 m, are predominantly situated on the Linderödsåsen and Nävlingeåsen Horsts, whilst the thicker deposits, 10-55 m, are situated within the Kristianstad Basin (Fig. 5). It is worth noting that the till is often absent beneath the glaciofluvial deposits (Ringberg 1991). On the NE slopes of the horsts, the till has been reported to form drumlins, crag and tail structures, and other similar landforms (Fig. 6) (Lidmar-Bergström et al.

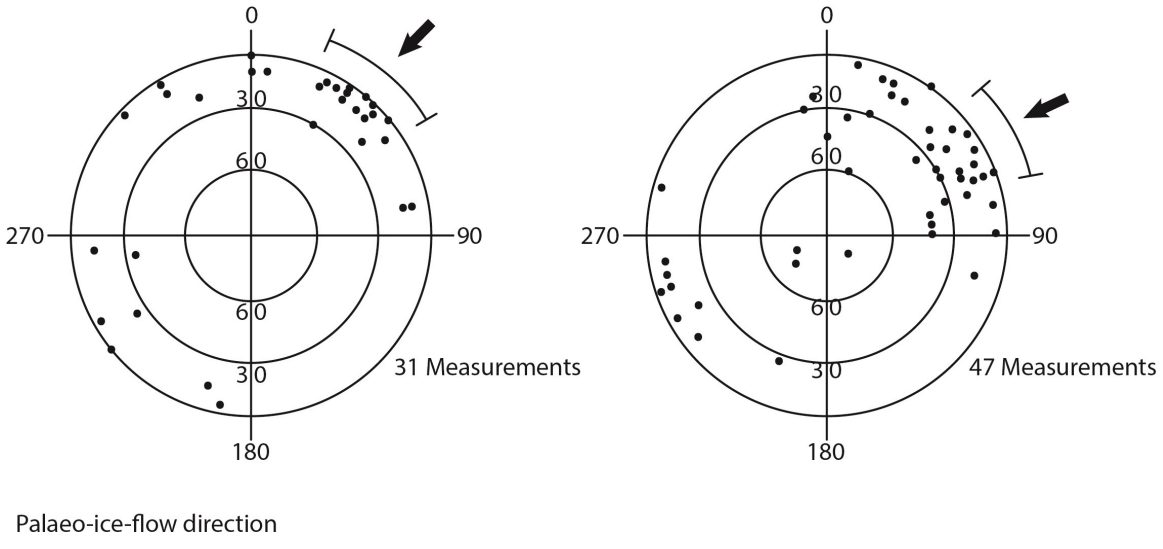

Figure 7: Structural measurements of a-axis orientations of long stretched middle-sized sand particles in till deposits located 1.3 km ENE of Västra Vram's church (Fig. 6). Modified from Ringberg (1991).

1991; Ringberg 1991). The remainder of the horsts are covered with a hummocky till interpreted by Ringberg (1991) to have been produced by dead-ice melt out over the underlying bedrock topography. The till situated within the Kristianstad Basin is on the contrary smoothly undulating as a result of the limestone topography and sediment reworking from when the area was occupied by the *Baltic ice lake* (Ringberg 1991).

Several glaciofluvial landforms run through the area (Fig. 6). The glaciofluvial sediments situated above the highest shoreline upon the horsts follow the major fracture valleys. These glaciofluvial deposits are relatively continuous within these valleys and become more sporadic beyond them (Ringberg 1991). Beneath the highest shoreline, 50-55 m.a.s.l., the glaciofluvial deposits follow the pre-existing topography along the horst edges and upon the limestone surface (Fig. 6). These deposits are characterised by wide ridges and intense reworking by wave action (Ringberg 1991).

In addition, Ringberg (1991) describes the local and/or sporadic existence of glacial lake sediments, glacial fine sediments, fine-grained lake sediments, flood sediments, aeolian sediment, as well as peat and clay within the area. Ringberg (1991) also mentions that the area beneath the highest shoreline is characterised by wave action reworking. This shoreline (Fig. 6) is most noticeable along the northern slope of the Nävlingeåsen Horst. Wave action reworked sediments with thicknesses of 1-7 m occur below this shoreline in the form of gravels, sands, and silts that overlie till, glaciofluvial sediments, and glacial clay. However, they are predominantly situated overlying till along the northern slope of the Nävlingeåsen Horst (Ringberg 1991).

3 Methods

To achieve the aims presented in the introduction (chapter 1) the following methods were applied. A remote geomorphological mapping was conducted for the study area (Fig. 3). The map was produced to identify the regional geological setting in which the study site is located and to provide a context for the subsequent geological findings. This was followed by field work conducted at the study site (Fig. 3 & 4) during which the exposure was logged to enable identification and documentation of the sedimentological and structural evidence. Subsequently, structural measurements were conducted with regards to prominent directional features. This was followed by clast shape and roundness analysis as well as fine gravel analysis in an effort to identify transport pathways and potential relationships between sedimentary units. This was done following standard procedures of established best practices described by Evans & Benn (2014a). Detailed descriptions of these methods are presented in the chapters below.

3.1 Geomorphological mapping

A regional remote geomorphological mapping of the study area (Fig. 3) was conducted by adhering to the following steps, *1-Data procurement*, *2-Pre-processing*, *3-Reconnaissance*, *4-Data processing*, *5-Digital mapping*, and *6-Map production*. This was done predominantly in accordance with the workflow presented by Chandler et al. (2018). The geographical information system used for the mapping was *Esri's* software *ArcGIS Pro V. 2.6.24783* with data from the Swedish government agency Lantmäteriet (n.d.). The data used for the mapping consisted of a high-resolution *digital elevation model*, *Quaternary map data*, *bedrock map data*, and *orthophotos* from different time periods (Table 1). The map is constructed to convey the regional geomorphological conditions of the study area to better explain and enable detailed analysis of the features and conditions evident at the study site. This entails a focus on geomorphological features related to palaeo-ice-flow, former pressure dynamics, sediment-landform associations related to variable water pressures or a continuum of water pressure conditions, and topographical relationships.

Table 1: List of the datasets used during the geomorphological mapping of the study area. The datasets were provided by Lantmäteriet (n.d.).

Product	**Resolution/Map-scale**	**Year**	**Agency**
DEM (Digital Elevation Model)	2 m	2019	Lantmäteriet
JORDARTER 1:1 miljon (Quaternary deposits 1:1 million)	1:1 000 000	2020	Swedish Geological Survey
JORDARTER 1:25 000-1:100 000 (Quaternary deposits 1:25 000-1:100 000)	1:25 000-1:100 000	2020	Swedish Geological Survey
BERGGRUND 1:1 MILJON (Bedrock 1:1 million)	1:1 000 000	2019	Swedish Geological Survey
BERGGRUND 1:50 000-1:250 000 (Bedrock 1:50 000-1:250 000)	1:50 000-1:250 000	2019	Swedish Geological Survey
Historiska Ortofoton (Historical Orthophotos)	-	Prior 1995	Lantmäteriet
Ortofoto (Orthophoto)	0.16 m/pixel	2019	Lantmäteriet

3.2 Sedimentology

The field work for this study was conducted during the month of March 2021 and focused on recording the sediment-bedrock transition zone in two dimensional logs. The preliminary conditions at the study site did not allow for a clear and descriptive view of neither the loose sediments, the underlying bedrock, or the contact between the two. Thus, the exposure was excavated using a trenching tool and further cleaned using a trowel and a brush. Care was taken not to transfer material between the different bodies of sediment within the exposure to not obscure the in-situ material with material of foreign origin.

The exposure was divided into four separate overlapping log sections (*section 1*, *2*, *3*, & *4*) in order to attain a high descriptive quality whilst still producing comprehendible logs in which the spatial progression could be followed whilst reducing distortion. This was done due to the immense curvature, angle, and undulation of the exposure, which prohibited a representative merge of the different log sections from being produced.

The sections were systematically referenced according to scale and photographed. The photographs were used as backdrops for the logging procedure, which was conducted at the study site using pen and paper. This was done to minimise the risk of scale errors whilst still maintaining a high level of descriptive classification, as the exposures were readily available for reference. The subsequent logging of the sections was conducted in accordance with standard procedures of established best practices presented by Evans & Benn (2014a). Initially, the logs included the outline of major sections, unit boundaries, and prominent clasts. Subsequently, more detailed structures were recorded, such as deformation structures and laminations. The characteristics of the sedimentary units were then noted, focusing on visual properties such as grain-size and sorting. In conjunction, lithofacies codes were assigned throughout the sections in accordance with a modified version of the lithological classification system presented by Evans & Benn (2014b). Additional evident structural elements within the bedrock were recorded in the logs and were used in conjunction with the sedimentology to discern former processes and conditions that have influenced the study site. This was followed by structural measurements, sampling for clast shape and roundness analysis, and sampling for fine gravel analysis. The symbology, lithofacies codes, sampling locations, and point of interest markers used for the logs are presented in the legend below (Fig. 8). Once completed, the logs were digitized using the software *Adobe Illustrator 2021*.

3.3 Structural measurements

In order to efficiently document and discern potential trends within the structural elements identified during the logging of the sections, these were quantified by

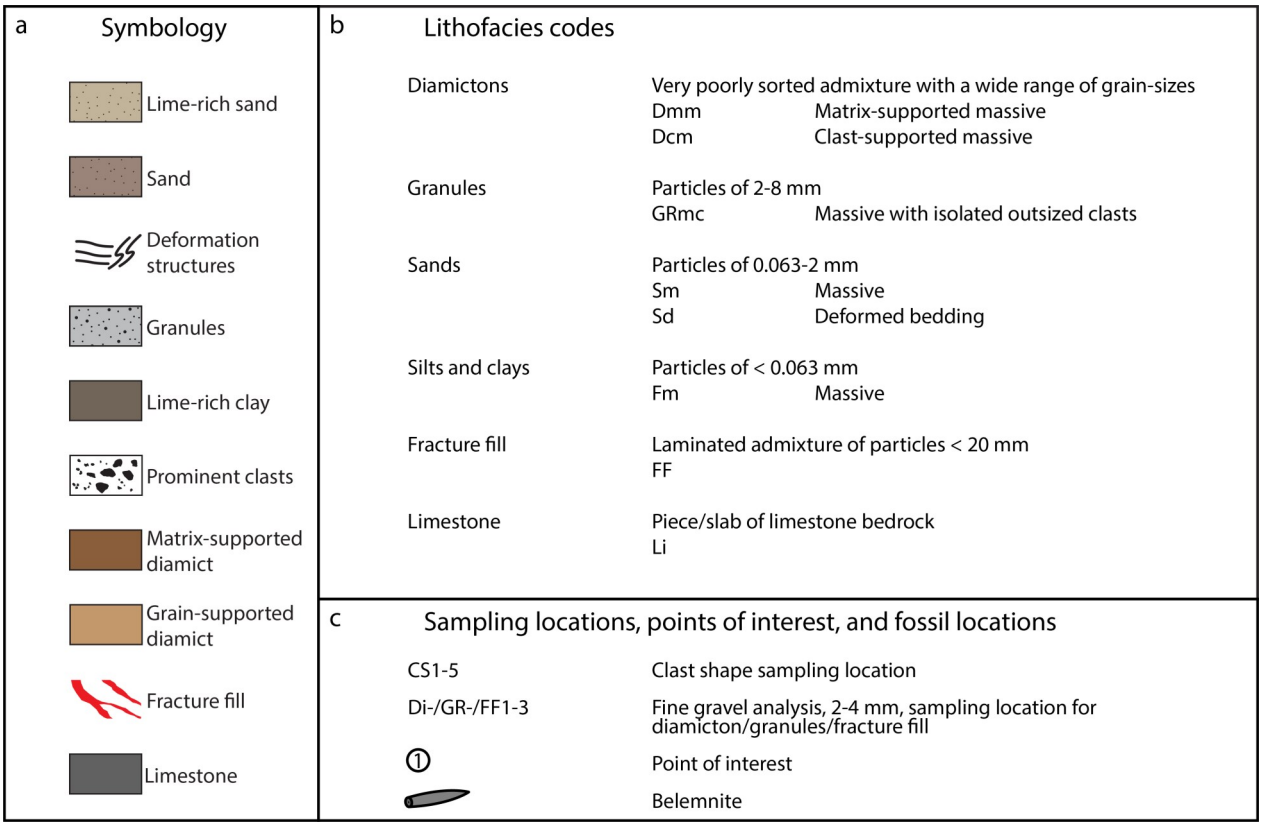

Figure 8: Legend for log section 1, 2, 3, & 4 (Fig. 14, 17, 19, & 22 respectively). a) Symbology used for the logs. b) The lithofacies codes used in the logs. These consist of a built upon version of the classification system presented by Evans & Benn (2014b). c) Markers indicating sampling locations, points of interest, and fossil locations.

taking structural measurements. This was done since structural measurements can provide valuable insights regarding glacier dynamics, such as ice-flow direction and deformational mechanisms (Holmes 1941; Derbyshire et al. 1976; Hart 1994; Benn 2014b). The measurements were recorded as dip-angle and dip-direction with regards to the orientations of the fractures identified within the limestone bedrock (Benn 2014b). This was done using a compass equipped with a clinometer and a flat board that was used as a fracture plane extension (Benn 2014b). The measurements were also supplemented with fracture thickness data that were recorded using a ruler. These measurements were taken throughout the vertical and lateral extent of the logged sections to produce measurements representative of the spatial continuum of the fractures. In addition to these measurements, dip-angle and dip-direction were recorded along the limestone section located to the north of the logged sections, where fracture planes were readily exposed. Thickness was not measured here due to an increase in bedrock cohesion, which inhibited accurate measurement of fracture thickness. The structural measurements were subsequently plotted in stereonets as both point and line features using the programme *Stereonet V. 11 © 2020* (Allmendinger et al. 2011; Cardozo & Allmendinger 2013). This was done for the logged sections and limestone section respectively. The structural measurements within the logged sections, with included thickness data, were categorised based on thickness in the stereonets to discern potential trends dependant on fracture thickness. These measurements were also plotted as points in a modified stereonet where the dip-angle was replaced with fracture thickness. This was done in an effort to further visualise potential trends dependant on fracture thicknesses. All stereonets were plotted as lower-hemisphere equal area (Schmidt net) projections (Howarth 1996) in line with current conventions within glacial sedimentology (Benn 2014b; Benn & Lukas 2021). Structural measurements within the overlying loose sediments were not possible to record due to sediment instability and clast abundance.

3.4 Clast shape & roundness analysis

Samples were collected for clast shape and roundness analysis since these techniques have been shown to enable discrimination between sediments of different genesis in glacial environments, especially when used in conjunction (Ballantyne 1982; Benn & Ballantyne 1994; Lukas et al. 2013). Thus, this technique was used to enhance the genetic classification of the sediments overlying the limestone. The samples were taken from the relevant bodies of sediment to deduct their genesis as well as to investigate potential relationships between them (Benn & Ballantyne 1994). Each sample contained 50 clasts restricted to granitic-gneissic lithologies, as mixing lithologies have been shown to have a deteriorating effect on the discriminatory capabilities of the technique, as lithology to a large extent determines clast shape (Drake 1970; Barrett 1980; Ballantyne 1982; Pérez 1986; Benn & Ballantyne 1994; Krüger & Kjaer 2008; Brook & Lukas 2012; Lukas et al. 2012; Benn 2014a). The clast long- (a), intermediate- (b), and short-(c)-axes were measured for each clast within each sample using a calliper to determine the axial ratios, (c/a), (b/a), and (a-b)/(a-c), that make up clast shape (Fig. 9) (Benn & Ballantyne 1994). The data was plotted in ternary diagrams using a modified version of *Triplot* that includes automated calculations of statistical parameters and a tab for input and plotting of roundness data (Fig. 9) (Sneed & Folk 1958; Graham & Midgley 2000; Lukas et al. 2013). In addition, the programme was used to derive the C_{40}-index of the respective samples, i.e. the percentage of clasts with a (c/a)-ratio ≤ 0.4. This was done since it has been shown to be an effective tool to distinguish blocky from elongated clast shapes and in extension enable discrimination between different transport pathways in glaciated environments (Ballantyne 1982; Benn 1992; Benn & Ballantyne 1993; Benn & Ballantyne 1994; Benn 2014a).

Roundness quantifies the characteristics of the surface textures superimposed upon clast shape (Powers 1953; Barrett 1980; Benn & Ballantyne 1994) and was determined for each clast in the respective samples. This was done in accordance with the roundness criteria produced by Benn & Ballantyne (1994) (Table 2). In addition, the presence/absence of surface textures was recorded for each clast in the respective samples and the results were subsequently plotted as frequency distributions. These percentages were used in conjunction with the clast shape data to discern the transport mechanism and depositional environment of the sampled material. The percentage of each roundness class (VA-very angular, A-angular, SA-sub-angular, SR-sub-rounded, R-rounded, and WR-well-rounded) was calculated for the respective samples and was subsequently plotted as frequency distributions using the modified version of *Triplot* (Fig. 9) (Sneed & Folk 1958; Graham & Midgley 2000; Lukas et al. 2013). For each respective sample, the summed percentages of VA and A were used as the RA-index and the summed percentages of R and WR were used as the RWR-index (Fig. 9) (Benn & Ballantyne 1994; Benn 2014a). Both parameters were used to increase the discriminatory capability regarding genesis classification (Lukas et al. 2013). This is because the RA-index and the RWR-index offer the greatest discriminatory capability for samples within their respective ends of the roundness spectrum (Lukas et al. 2013; Benn 2014a). For a certain sample, only using one of the indices could prohibit genetic classification or potentially result in an inaccurate classification. A higher RA-index tends to be indicative of frost weathering and subglacial edge-rounding, more immature material, whilst a higher RWR-index tends to be

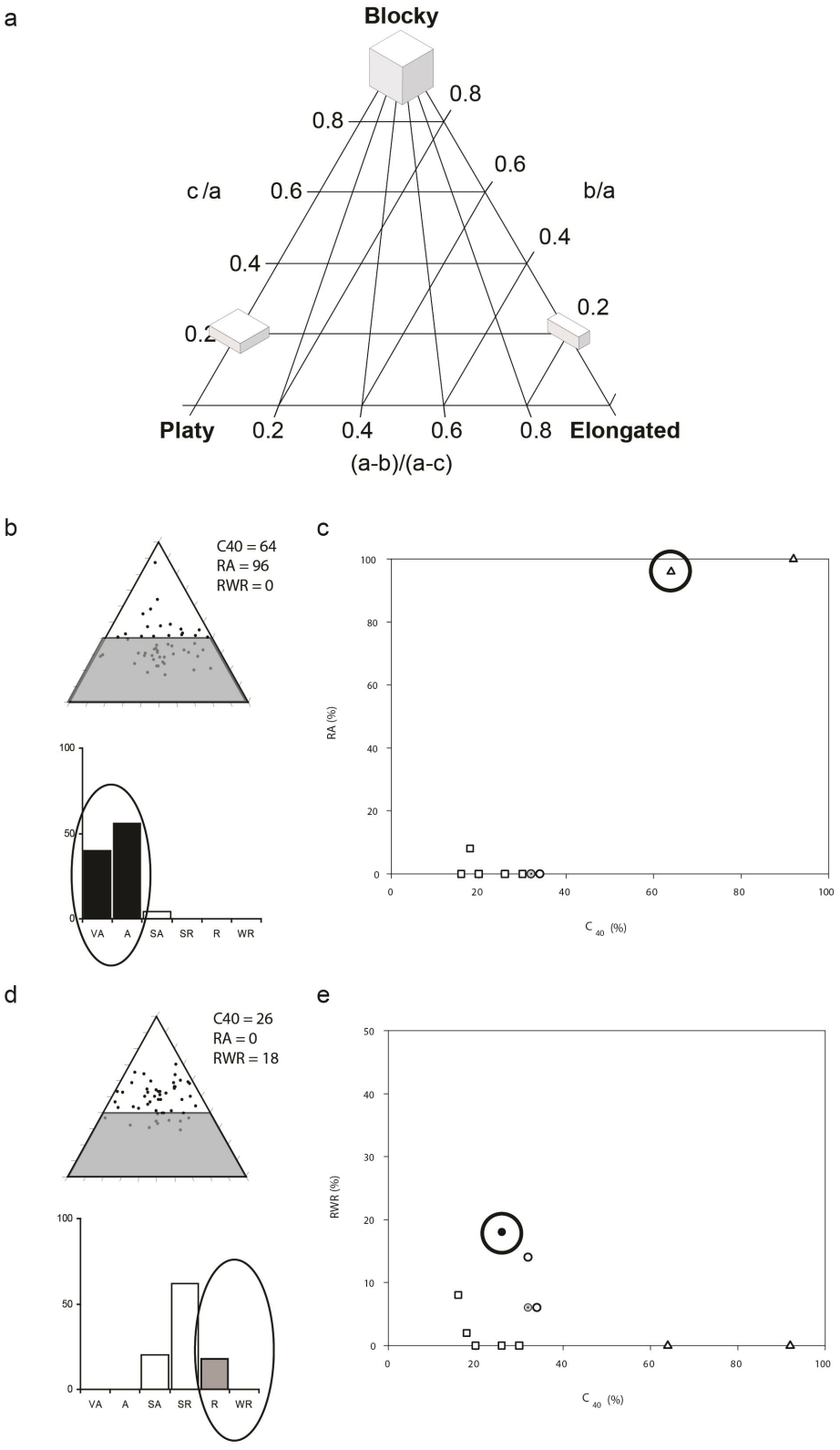

Figure 9: Example of the usage of different clast shape analysis elements, as originally designed by Benn & Ballantyne (1993) and Benn & Ballantyne (1994). a) Principal clast shape ternary diagram displaying the axial scales with the respective endmember appropriate terminology. b) Example of a supraglacial clast shape sample plotted in a ternary clast shape diagram and clast roundness frequency distribution chart. The C_{40}-index is derived from the percentage of clasts plotted in the grey area of the ternary diagram, c/a-axis ≤ 0.4. The RA- and RWR-indices are derived from the summed percentages of angular clasts (VA & A) and rounded clasts (R & WR) respectively. c) Example of a RA-C_{40}-covariance diagram. The circled data point is devised form the data in Fig. 9b. d) Example of a distal fluvial clast shape sample plotted in a ternary clast shape diagram and a roundness frequency distribution chart. e) Example of a RWR-C_{40}-covariance diagram where the circled data point is devised from the data in Fig. 9d (Lukas et al. 2013).

Table 2: Roundness classes with corresponding classification criteria according to Benn & Ballantyne (1994).

Roundness class	***Description***
Very angular (VA)	*Very acute edges and/or sharp protuberances*
Angular (A)	*Acute edges with no evidence of rounding*
Sub-angular (SA)	*Rounding confined to edges; faces intact*
Sub-rounded (SR)	*Rounding of edges and faces; often facetted*
Rounded (R)	*Marked rounding of both edges and faces; merging of edges and faces*
Well-rounded (WR)	*Distinction between faces and edges not possible*

indicative of subglacial reworking of fluvially-rounded sediment, more mature material (Lukas et al. 2013).

These two datasets, the C_{40}-indices and the corresponding RA- and RWR-values, were then plotted in RA-C_{40}-covariance and RWR-C_{40}-covariance diagrams using the modified version of *Triplot* (Fig. 9) (Sneed & Folk 1958; Graham & Midgley 2000; Lukas et al. 2013). This was done in an effort to discern the genesis of the different sediment units as well as any potential variability of these factors throughout the exposure (Benn & Ballantyne 1994; Lukas et al. 2013).

3.5 Fine gravel analysis

In an attempt to further discern potential relationships between different bodies of sediment a fine gravel analysis was conducted largely in accordance with Ehlers (1979). The samples were collected from the appropriate sediment bodies by collecting a minimum of 1 kg of sediment from the respective sampling locations. For each sample, the 2-4 mm grain-size fraction was extracted using sieves after the material had been dried and cleaned from clay particles by using sodium pyrophosphate ($Na_4P_2O_7$) as a deflocculant (Bates et al. 1978). Once cleaned and dried, the grains were analysed using a microscope and subsequently classified into one of the respective lithological categories, *Cretaceous/Tertiary limestone*, *Palaeozoic limestone*, *sandstone*, *siltstone/shale*, *quarts*, *flint*, *crystalline*, or *other*. The percentages of the different categories were then plotted as frequency distributions for visualisation and comparison.

4 Results

The results are presented in the following sections. First, the results and interpretations from the *Geomorphological mapping* are presented. This is followed by the results from the field work studies, starting with the descriptions of the *Sedimentology* that are presented in conjunction with the respective log sections. Thereafter, the results from the *Structural measurements* are presented through the produced stereonets. Lastly, the results from the *Clast shape & roundness analysis* and the *Fine gravel analysis* are presented, respectively.

4.1 Geomorphological mapping

4.1.1 Major features

From the geomorphological mapping some key features can be distinguished (Fig. 10). The two most evident features are the Linderödsåsen Horst in the SW and the Nävlingeåsen Horst in the mid-west (Lidmar-Bergström et al. 1991). These prominent features stretch through the landscape with a NW-SE orientation, with steep NE-facing slopes and low angled SW-facing slopes. The Kristianstad Basin is distinguishable on the geomorphological map as the blue coloured SE quadrant, which extends up along the NE slopes of the Nävlingeåsen and Linderödsåsen Horsts (Fig. 10) (Lidmar-Bergström et al. 1991). This is a lowland area with a relatively smooth undulating surface. It contains channels in its southern section with E-W orientations and lakes in its northern section. The flat lowland area of the Kristianstad Basin and uniform structures of the Nävlingeåsen and Linderödsåsen Horsts are clearly distinguishable from the northern part of the study area. There, the topography is more variable, and the area lacks features of the same km-scale as the horsts and the basin. Superimposed on these larger features are two distinct types of ridge features which are described and discussed below.

4.1.2 Elongated straight ridges

4.1.2.1 Description

The first type of ridge features are composed of numerous elongated, straight ridges situated on the high ground of the study area. These range in length from under 0.1 km to approximately 2 km and are primarily found on the Nävlingeåsen and Linderödsåsen Horsts as well as in the central parts of the northern mapped area, whilst being largely absent within the Kristianstad Basin. They have straight ridges, displaying predominant NE-SW orientations, with wider NE-ends that taper towards the SE, resulting in distinct teardrop shapes. It is worth noting that the orientation of these features becomes increasingly westerly towards the SW of the study area. However, deviations from the NE-SW trend do occur. This can be seen approximately 3.75 km north of the study site and approximately 7.5 km SE of the study site. At these locations, the same type of landforms display ESE-WNW orientations. Furthermore, the same type of features are found in the NE corner of the study area, displaying N-S orientations.

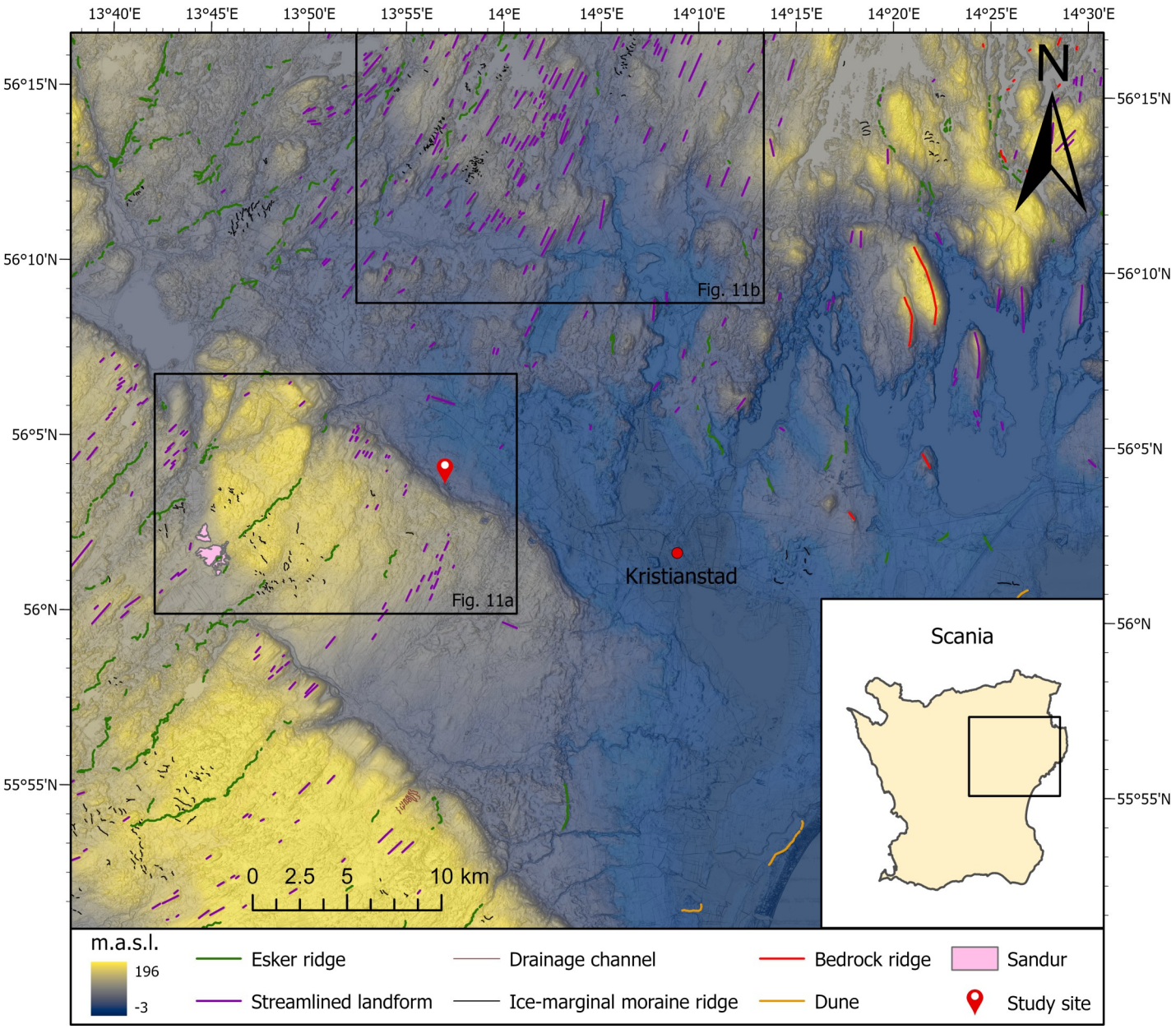

Figure 10: Regional geomorphological map of the study area displaying key features with regards to palaeo-ice-flow, former water pressure conditions, and topographical relationships. The map consists of a multidirectional hillshade model with a 10 X vertical exaggeration, which is overlain with a DEM and mapped features, respectively. The data were provided by the Swedish government agency Lantmäteriet (n.d.).

4.1.2.2 Interpretation

The teardrop-shaped landforms are interpreted as streamlined landforms due to their characteristic morphology (Fig. 10 & 11) (Clark et al. 2009; Spagnolo et al. 2011; Dowling et al. 2015; Möller & Dowling 2015). More precise classifications of these streamlined features, such as drumlins, crag and tails, and other similar landforms would require further field investigation of the individual landforms. However, it is worth noting that several of these features coincide spatially with a bedrock outcrop at their wider up-ice ends, indicating that these could be crag and tail features (Evans & Hansom 1996; Stokes et al. 2011). Furthermore, many of these streamlined landforms characteristically appear on the horst crests, which corresponds to where Ringberg (1991) identified drumlins. This could indicate that at least a part of the streamlined landforms located here are drumlins or the results of drumlinisation processes (Smalley & Unwin 1968; Ely et al. 2018). The long axes of these features are considered to represent the palaeo-ice-flow direction of the area (Clark et al. 2009; Ely et al. 2018). Thus, the palaeo-ice-flow direction has been from the NE to the SW whilst becoming increasingly westerly towards the SW. These palaeo-ice-flow indicators strongly correlate with those presented by Ringberg (1991) (Fig. 6 & 7). The streamlined landforms that instead display ESE-WNW orientations could potentially belong to the older generation of ESE-WNW palaeo-ice-flow suggested by Ringberg (1991), as

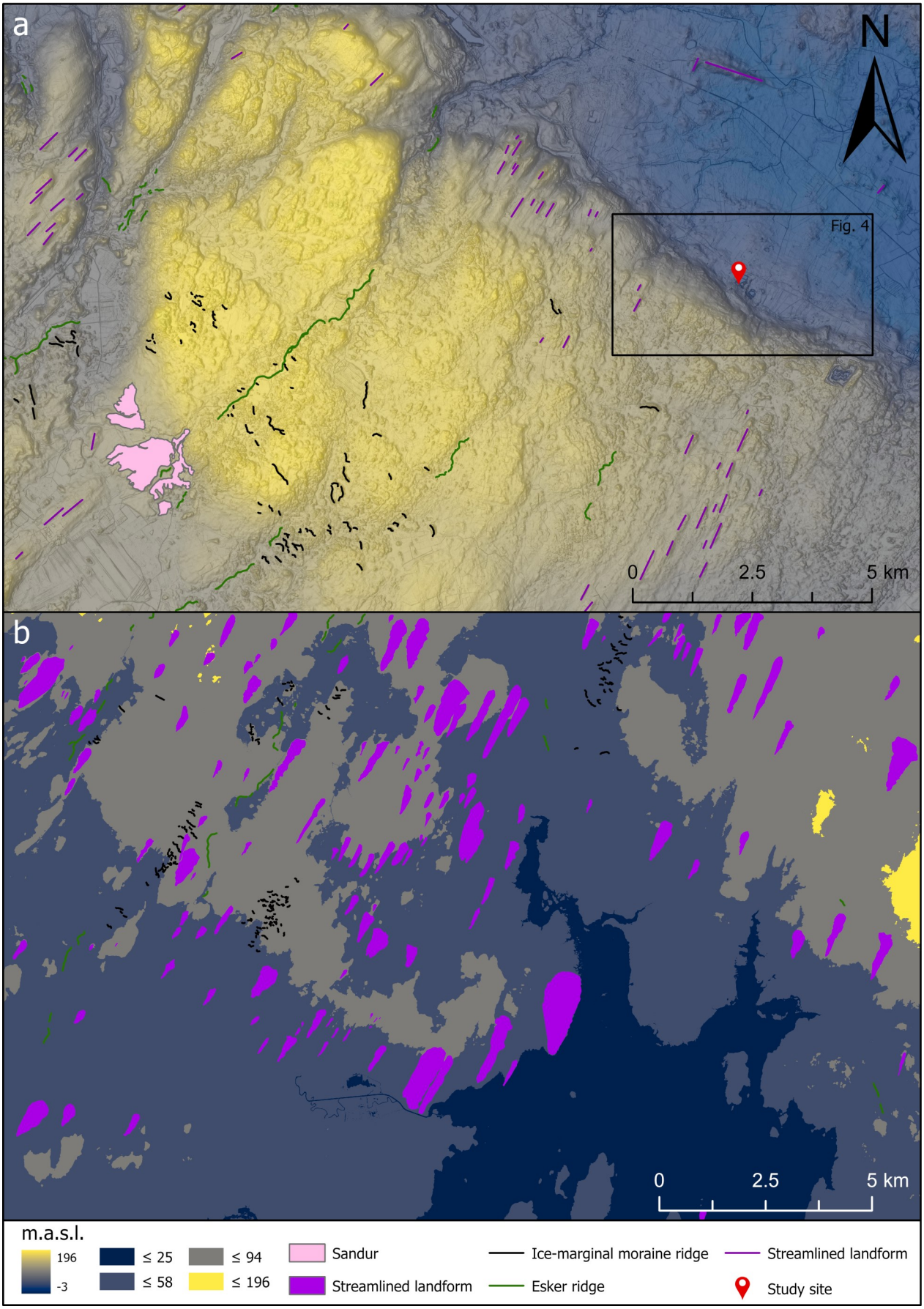

Figure 11: Enlarged areas within the geomorphological map of the study area (Fig. 10). a) Geomorphological close up displaying the characteristic horst esker spatial relationship. b) Geomorphological close up of the central northern area displaying abundant streamlined landforms. The data were provided by the Swedish government agency Lantmäteriet (n.d.).

these share the same orientation. In contrast, the N-S oriented streamlined features in the NE corner of the study area are likely related to the palaeo-glaciated terrain and palaeo-ice-flow direction typical of the county of Blekinge to the east (Persson 2000).

4.1.3 Sinuous ridges

4.1.3.1 Description

The second type of ridge features consist of ridges displaying sinuous curvatures and local instances of bifurcation. The individual segments range from tens of metres to more than 3 km in length. However, if neighbouring ridges are linked, these segments reach combined lengths of more than 10 km. Like the straight ridges addressed above, these ridge features are also predominantly located on the higher ground of the study area whilst being scarce within the lowland area of the Kristianstad Basin. These landforms, despite having a meandering planform, display general NE-SW orientations. In addition, around the horsts in the SW quadrant, these landforms exhibit a regular pattern of occurrence. Here, they are distinguishingly absent in the lowlands NE of the horsts, whilst then appearing further towards the SW on top of the horsts, past their steep NE-facing slopes. For one such ridge, it is evident how it is absent in the lowland NE of the Nävlingeåsen Horst whilst running in a NE-SW direction starting at the horst crest. Further towards the SW, this ridge terminates in a lowland area where it gives way to a flat-topped, fan-shaped deposit. Furthermore, in multiple locations these ridges characteristically occur together with sets of shorter transverse ridges on one or both sides of the larger sinuous ridge. These yet smaller accompanying ridges are typically a few hundred metres in length but can reach up to a km and have general NW-SE orientations. These smaller side ridges are often arcuate in planform.

4.1.3.2 Interpretation

The ridges displaying sinuous planforms and local instances of bifurcation are classified as esker ridges due to their characteristic morphology (Fig. 10) (Smith et al. 2006; Storrar et al. 2013; Chandler et al. 2018; Knight 2019). This interpretation is strengthened by the fact that these ridges spatially coincide with many esker ridges and glaciofluvial deposits that have previously been mapped by Ringberg (1991) and Lantmäteriet (n.d.). The predominant NE-SW orientation of these esker ridges is interpreted to be representative of the former subglacial water pressure conditions and in extension also the regional palaeo-ice-flow direction, since water pressure and ice-flow are governed by ice surface slope (Cuffey & Paterson 2010). The transverse ridges along the esker ridges are interpreted as ice-marginal moraine ridges, formed either as terrestrial moraines (Fig. 10 & 11) (Hewitt 1967; Sharp 1984; Evans & Twigg 2002) or alternatively De Geer moraines (Boulton 1986; Ottesen & Dowdeswell 2006; Todd et al. 2007) depending on their spatial relationship to the highest shoreline in the area (50-55 m.a.s.l.). This is based on the geomorphology, spatial relationships of the ridges, topographic location, spatial relationships to the esker ridges, relation to the palaeo-ice-flow direction (Ringberg 1991), and Quaternary map data (Lantmäteriet n.d.). Thus, these sets of moraine ridges seem to be indicative of ice-front oscillations within the area. The flat-topped, fan-shaped deposit is classified as a sandur due to the distinct geomorphology of the feature (Fig. 10 & 11) (Chandler et al. 2018).

4.1.4 Sparse landforms

4.1.4.1 Description

In addition, there are some sparser landforms within the area, such as lobate ridges along the SE-coast that measure approximately 120 m to 1300 m in length. In the NE corner of the study area, there are also a set of distinctly larger streamlined ridge features. These measure up to approximately 2 km in width and 4 km in length. Lastly, by the Linderödsåsen Horst's NE slope in the SE, there is a set of parallel incised channels. These are oriented NW-SE and range in length from approximately 74 m to 717 m. They are broadly equally spaced with an approximate distance of 120 m.

4.1.4.2 Interpretation

The lobate ridges along the SE coast are interpreted as dunes based on their morphology, spatial setting, and correlation with pre-existing sediment map data (Fig. 10) (Bernhardson & Alexanderson 2017; Lantmäteriet n.d.). The large ridges in the NE are interpreted as streamlined bedrock ridges due to their morphology, size, and the prevalent presence of outcropping bedrock (Fig. 10) (Lantmäteriet n.d.). These bedrock ridges mark the onset of another type of geological setting characteristic of the county of Blekinge towards the east (Persson 2000; Lantmäteriet n.d.). Lastly, the features observed on the crest of the Linderödsåsen Horst towards the SE are interpreted as lateral drainage channels due to their characteristic incised structure parallel alignment with the ice border lines of the area (Fig. 6 & 10) (Mannerfelt 1949; Ringberg 1991). These would then indicate former ice-margin positions and an active oscillatory behaviour similar to the terminal moraines addressed above (chapter 4.1.3.2) (Benn & Evans 2010).

4.2 Sedimentology

As shown from the geomorphological mapping and the description of the study site (chapter 2 & 4.1), the study site is located just down-slope of the Nävlingeåsen Horst's NE steep slope, at the periphery of the Kristianstad Basin (Fig. 4 & 10). At the study site, the exposure is situated in the SW wall of the quarry with an orientation stretching from 332° NNE to 192° SSE. The entire exposure is 42 m wide, out of

which the logged sections measure 14 m in width, ~1.8 m in height, and leans up to 46° from the vertical, although the angle and height vary throughout (Fig. 12). The logged section within the exposure have been divided into *section 1*, *2*, *3*, and *4* (Fig. 12). The calcareous bedrock in the limestone section, located to the north of the logged sections, is structurally homogenous with a near-horizontal upper surface (Fig. 12). At the transition from the limestone section into *section 1*, the bedrock surface starts to dip with an apparent orientation towards the SSW and continues to do so throughout *section 2*, *3*, and *4* (Fig. 12). The logs presented below follow the legend presented in the methods (chapter 3.2) (Fig. 8).

4.2.1 Section 1

S*ection 1* can be seen in a unaltered photograph (Fig. 13) and as a log (Fig. 14) below. This section consists of fractured limestone (Li) that has been filled with clastic sediments. The fractures, with the fracture fill material (FF), display thicknesses from < 1 mm up to 100 mm towards the upper parts of the limestone. The grain-size of the fracture fill ranges from < 0.063 mm to ~20 mm and consists of a mixture of lithologies as well as a prominent clay content. The fracture fill is typically laminated, with larger grain-sizes concentrated in the centre of the fractures whilst the finer material is concentrated along the fracture walls (Fig. 15). However, it is not uncommon that that the fracture fill displays more chaotic laminations with less clear size-dependant distributions. In addition, the fracture fill becomes progressively finer deeper into the fractures, with a concomitant decrease in fracture thickness. However, exceptions to this trend of diminishing thickness with depth do occur towards the left of the section. Here, there is a major area of fractured limestone with major infill of matrix-supported, massive diamict (Dmm) (marked ① in Fig. 14). The fractures that reach this feature widen around the point of interception (Fig. 15).

The limestone does not consist of a structurally coherent framework, but rather takes the form of individual pieces/slabs that are separated from each other by the fractures described above. These separate pieces/slabs of bedrock vary greatly in size, measuring up to 3 m in width and 0.45 m in thickness. Regardless of their size, these bedrock pieces/slabs display lenticular shapes with thicker centre sections that taper off towards the sides (see the Li pieces/slabs in Fig. 14) across the whole width of the exposure. Multiple levels of such lenticular shapes are apparent, as two minor individual lenticular bodies can be seen to constitute a larger lenticular body (marked Ⓐ & Ⓑ in Fig. 15). The bedrock surface dips towards the SSW throughout the section, which deviates from the semi-horizontal bedrock surface within the limestone section located north of *section 1* (Fig. 12).

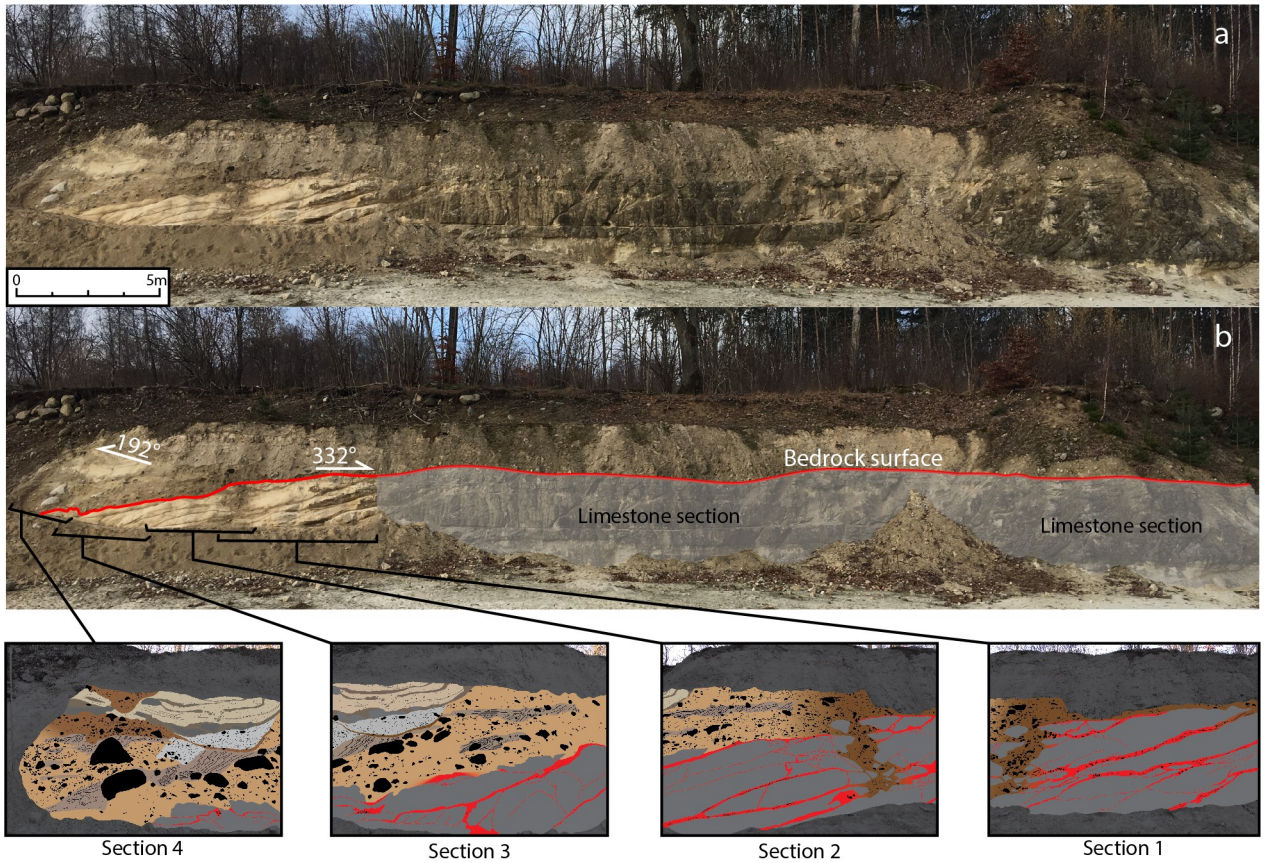

Figure 12: Overview photographs of the exposure displaying the spatial distribution of the different sections and key features. a) Photograph of the exposure. b) Modified photograph of the exposure indicating the position of the bedrock surface, the limestone section, and the orientation of the logged sections. The spatial relationships between section 1, 2, 3, and 4 are marked out.

Figure 13: Unaltered photograph of section 1.

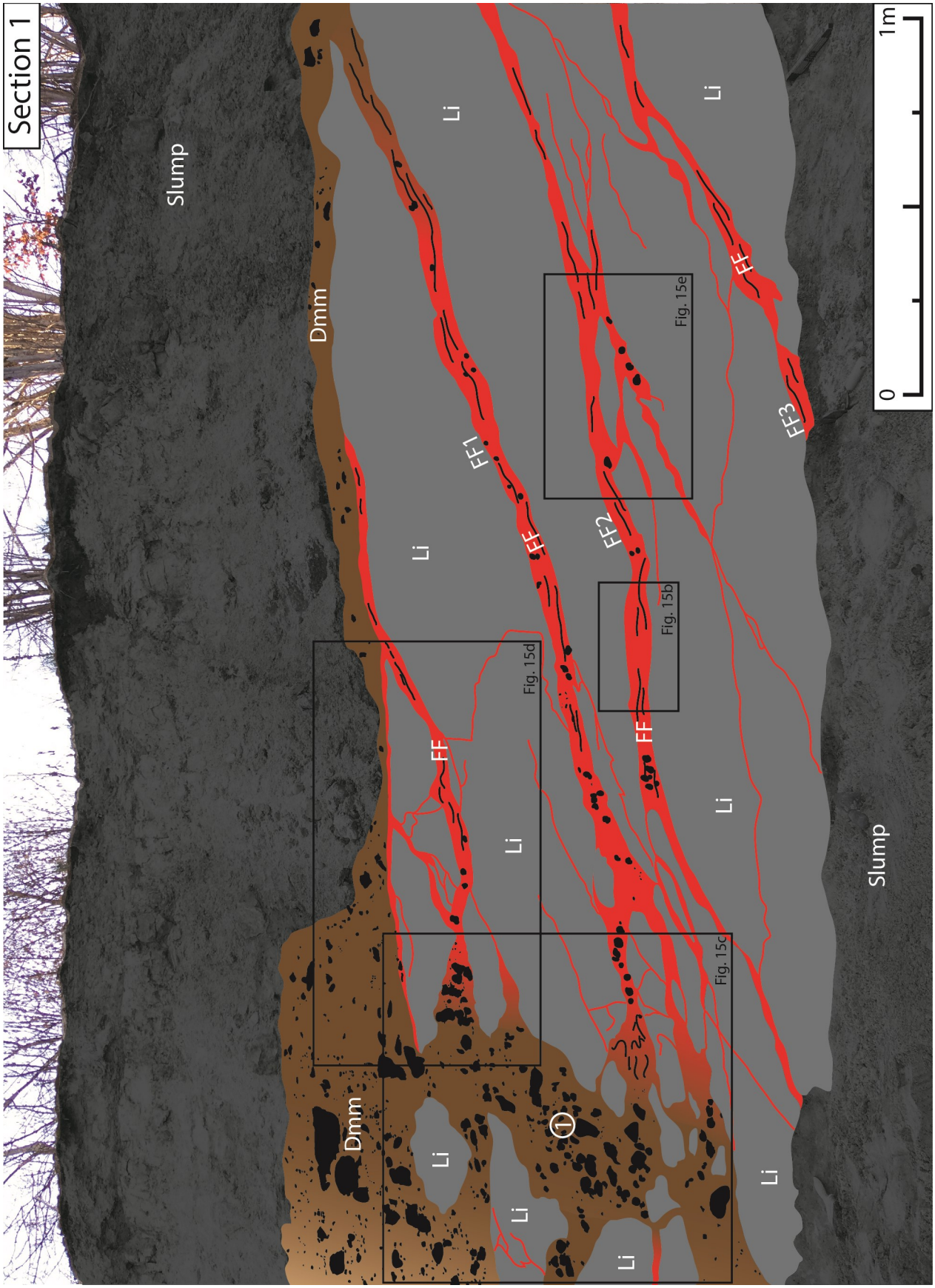

Figure 14: Sedimentary log of section 1.

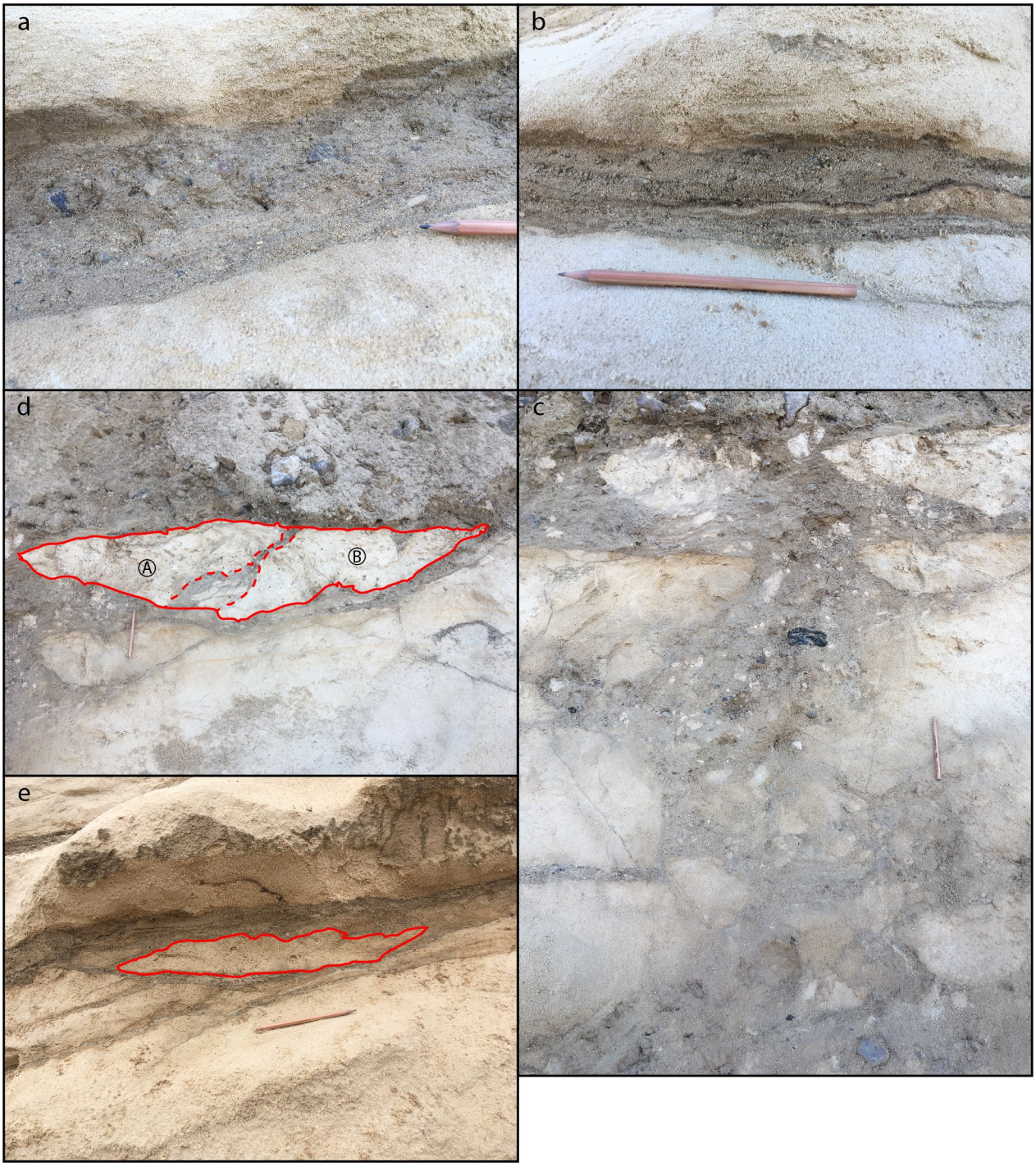

Figure 15: Close up photographs from section 1 of the logged exposure, see pencil for scale. a) Fracture fill with larger clasts (~20 mm) concentrated in the centre of the fracture and laminated fines concentrated along the fracture walls. b) Laminated fracture fill containing larger grain-sizes in the centre of the fracture. c) Major limestone breakdown (marked ⊙ in Fig. 14) with infilled matrix-supported massive diamict. d) Multiple levels of lenticular shapes displayed by the slabs of limestone. The individual lenticular slabs marked Ⓐ and Ⓑ can be seen to have constituted a larger lenticular slab prior to disintegration. e) Highlighted, liberated, lenticular piece of limestone enveloped by fractures containing fracture fill material.

The limestone is overlain by a matrix-supported, massive diamict of similar composition as the diamict located within the fractured bedrock (marked ① in Fig. 14). It is highly unsorted with a clay-rich, sand-dominated matrix and contains abundant clasts with a-axes up to ~22 cm in length. The majority of the clasts are sub-rounded as determined through visual inspection and surface textures such as striae, facets, and bullet-shapes are common. Furthermore, the matrix-supported, massive diamict is homogeneous and lacks evident structural elements. The material extends towards the right in the section whilst gradually changing to a clast-supported, massive diamict (Dcm) through a diffuse contact further towards the left in *section 2*. The vertical extent is unknown due to coverage of slumped material. It is worth noting that within the centre of the section, there is an intermediate layer of fracture fill separating the limestone and the diamict. Here, the fracture fill reaches a maximum thickness of ~4 cm and displays sharp boundaries to the surrounding material.

4.2.2 Section 2

In *section 2*, the major area of fractured limestone (marked ① in Fig. 14) is again visible towards the right (Fig. 16 & 17). As in *section 1*, the fractures continue with the same apparent orientation and contain the same laminated fracture fill (FF). Also here, the bedrock consists of liberated pieces/slabs of lenticular shapes that are separated from each other by the fracture network. The upper limestone surface continues with an apparent dip towards the left (SSW) throughout the section. The thickness of the fractures diminishes with depth, which is concomitant with the fracture fill becoming progressively dominated by fines. This takes the form of clay dominating the fracture tips, with fewer clasts present compared to in the wider upper parts of the fractures. However, it is worth noting that the thickness of certain fractures increases at depth, at certain points. This can be seen where two separate fractures merge into one (marked ② Fig. 17).

The material directly overlying the limestone, except for in the left part of the section, consists of a layer of fracture fill up to ~4 cm thick that displays sharp boundaries to the surrounding material. Above this layer, the material shifts from the matrix-supported, massive diamict (Dmm) introduced in *section 1* into a clast-supported, massive diamict (Dcm) towards the centre of the section through a diffuse contact (Fig. 17). The upper vertical extent of the clast-supported, massive diamict is unknown due to coverage of slumped material, but it is seen to extend towards the left throughout *section 2*. Based on field observations, this clast-supported, massive diamict contains abundant clasts and a clay-rich, sand-dominated matrix. The prominent clasts display faint laminations that have an apparent dip towards the left (SSW) throughout the section. The clasts have a-axes up to ~20 cm and are visually determined to be predominantly sub-rounded. In addition, the clasts commonly display striae, facets, and bullet-shapes.

Furthermore, the clast-supported, massive diamict contains inclusions of two deformed sand lenses (Sd) within this section (Fig. 17). The upper lens measures ~150 cm wide with a maximum thickness of ~13 cm, whilst the lower measures ~80 cm wide and up to ~15 cm in thickness. The orientations of these lenses are coherent with the lamination of the prominent clasts in the surrounding clast-supported, massive diamict. Furthermore, the lenses are highly deformed, displaying boudinage, inclined asymmetric folds, shear planes, and truncated bedding. These lenses consist of poorly sorted, clay-rich material with a wide range of grain-sizes, up to granules, and contain outsized clasts measuring up to ~15 cm in a-axis. Lastly, in the uppermost left corner of the section, a lime-rich, massive sand lens is visible (Sm). This material is further described in *section 3*.

4.2.3 Section 3

Section 3 is presented below as an unaltered photograph and a sedimentary log, respectively (Fig. 18 & 19). Here, both the fractures and the bedrock surface continue with an apparent dip towards the left (SSW) throughout the section. The fractures, compared to in the previous sections, are smaller and the fracture fill (FF) is finer, more clay-dominated, and larger clasts are less common. As in the previous sections, the fracture fill becomes finer deeper into the fractures, with a concomitant decrease in fracture thickness. The limestone (Li) is sporadically overlain by layers of fracture fill. Despite these layers of material having previously displayed sharp boundaries towards the limestone and overlying diamicts, here they display a laterally diffuse boundary towards the clast-supported, massive diamict (Dcm) in the centre of the section.

Towards the lower left in the limestone, there is a characteristic pocket of infilled material (marked ③ in Fig. 19). This pocket contains distinctly larger clasts, up to ~2 cm, which is not found in the surrounding fractures in this section. In addition, these clasts are concentrated to the left within this pocket, whilst the right part primarily consists of clay-rich sand (Fig. 20a). The fractures that are connected to this sediment pocket are smaller and only reach thicknesses of a few millimetres. Similar sediment pockets have been identified in *section 2* and *section 4* (marked ④ & ⑤ in Fig. 17 & 22 respectively).

The overlying clast-supported, massive diamict stretches throughout the entire section. The upper spatial extent of the diamict is still unknown in the right part of the section due to coverage of slumped material. However, towards the left the diamict is overlain by sediments, enabling measurements of the thickness that progressively tapers down to ~30 cm

Figure 16: Unaltered photograph of section 2.

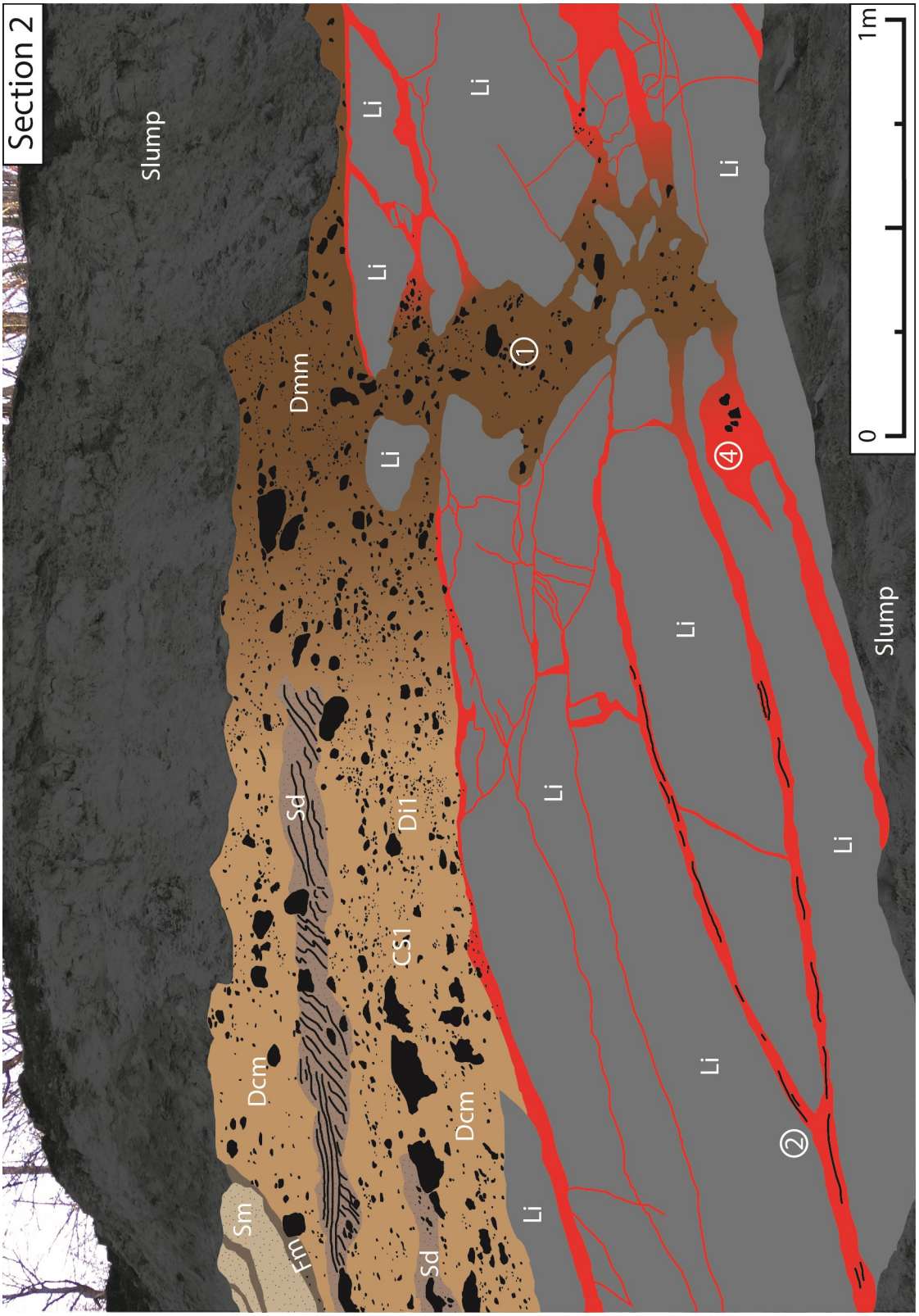

Figure 17: Sedimentary log of section 2.

Figure 18: Unaltered photograph of section 3.

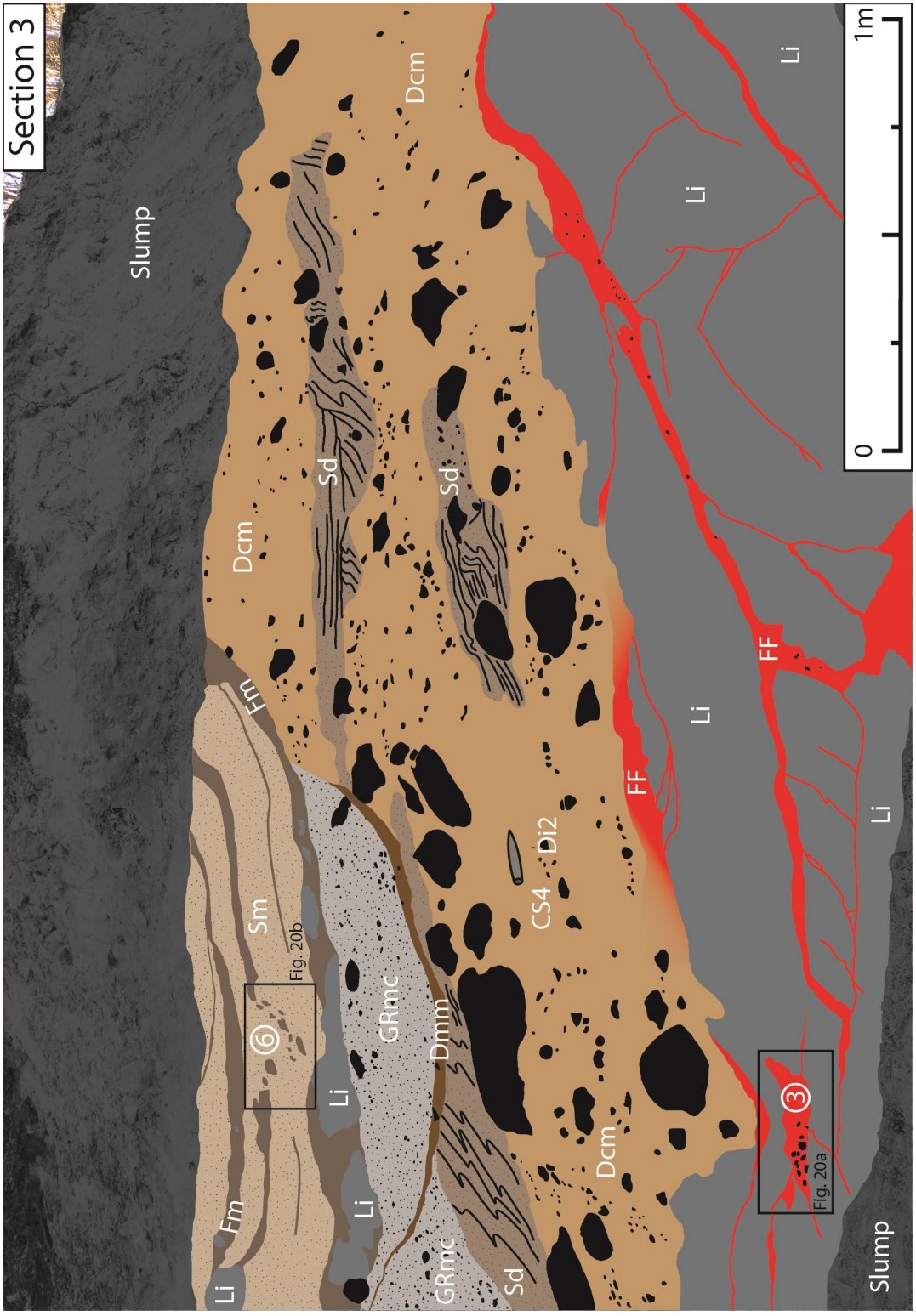

Figure 19: Sedimentary log of section 3.

(Fig. 19). The faint lamination displayed by the prominent clasts within the diamict continues throughout this section as well. The clasts are visually determined to be predominantly sub-rounded, they commonly display striae, facets, and bullet-shapes, and they display a-axes up to ~40 cm long. Furthermore, the larger clasts typically have a-axis orientations aligned parallel with the clast lamination. In addition, it is worth noting that belemnite fossils were found within the central part of the diamict (Fig. 19).

The deformed sand lenses (Sd) described above for *section 3* (Fig. 17) are here seen in their entirety with a less distorted point of view that better visualises their deformed structures (Fig. 19). To the left in the section, there is a third lens of deformed sand with similar composition and structures, i.e. poorly sorted, clay-rich, up to granule-sized material displaying boudinage, inclined asymmetric folds, shear planes, and truncations. The lens measures ~200 cm wide, has a maximum thickness of ~35 cm, and contains outsized clasts measuring up to ~13 cm.

In turn, the lens is overlain by a pair of poorly sorted, massive, augen-shaped granule lenses with isolated outsized clasts measuring up to ~10 cm (GRmc) (Fig. 19). A thin layer of matrix-supported, massive diamict (Dmm), with similar composition to the diamict described in *section 1*, separate these granule lenses. The left granule lens measures ~63 cm wide and ~36 cm thick and the right lens measures ~130 cm wide and ~25 cm thick.

A larger body of lime-rich, sorted, massive sand (Sm) overlies the granule lenses. This sand unit contains multiple horizons of clay-rich, massive fines (Fm), ranging in thickness from < 0.1 cm up to ~15 cm at the bottom of the massive sand unit. Furthermore, the horizons of massive fines contains sporadic, loosely consolidated, elongate limeclasts measuring up to ~40 cm in length. The horizons are deformed and fragmented with evident boudinage structures. The deformed state is most evident in the V-shaped, fragmented section (marked ⑥ in Fig. 19) of one of the middle horizons (Fig. 20b). The upper part of the massive sand unit is covered by slumped material, resulting in an unknown vertical extent (Fig. 19).

4.2.4 Section 4

Section 4 can be seen as an unaltered photograph and as a sedimentary log below (Fig. 21 & 22). In this section, the limestone (Li) bedrock continues with an apparent dip towards the left (SSW) until it is no longer visible due to coverage of slumped material. The fractures in the limestone are more diffuse here with regards to their apparent orientation and they are thinner compared to their previous counterparts. They reach thicknesses of a few mm and the fracture fill (FF) predominantly consists of clay-rich to clay-dominated sediments. Also here, they envelop pieces/slaps of limestone.

Overlying the limestone, the segment of clast-supported, massive diamict (Dcm) continues towards the left (SSW). In addition, its thickness increases from ~30 cm up to ~100 cm towards the left, if the inclusions of minor deformed sand lenses (Sd) are disregarded (Fig. 22). Here, the lamination of prominent clasts is fainter, although still present. In this section, the clast-supported, massive diamict contains considerably larger clasts than seen in the previous sections. This is most evident towards the left where clasts measure up to ~60 cm in size. As in the previous sections, the clasts are predominantly sub-rounded and commonly display striae, facets, and bullet-shapes.

The continuation of the leftmost deformed sand lens described in *section* 3 (Fig. 19) can here be traced with a continued dip towards the left (SSW). The continuation of this lens also displays boudinage,

Figure 20: Close up photographs taken within section 3, see pencil for scale. a) Sediment pocket within the limestone in which larger clasts (~2 cm in size) are concentrated in the left half of the pocket, whilst clay-rich sand dominates in the right half. b) Deformed, V-shaped, fragmented horizon of massive, clay-rich fines situated in massive, sorted, lime-rich sand.

Figure 21: Unaltered photograph of section 4.

Figure 22: Sedimentary log of section 4.

asymmetric inclined folds, truncated bedding, shear planes, and outsized clasts as described in *section 3* (Fig. 23). In addition, inclusions of sand lenses of similar composition (Sd) occur further to the left within the clast-supported, massive diamict in this section. These lenses also display deformation structures in the form of boudinage, inclined asymmetric folds, truncation, and shear planes, with the addition of clast pavements. However, the two minor sand lenses towards the left in the section lack internal deformation structures whilst still displaying overall deformed shapes, such as boudinage. The lower minor lens measures ~50 cm wide and up to ~5 cm thick and the upper minor lens measures ~25 cm wide and up to ~8 cm thick. The lowermost deformed sand lens on the left measures ~75 cm wide and has a maximum thickness of ~36 cm. In its central part, a structure is evident that can most accurately be described as augen-shaped (marked ⑦ in Fig. 22). The lithology of the material composing this augen structure is coherent with that of the encompassing deformed sand lens. The top left deformed sand lens measures ~156 cm wide. Its highly deformed shape makes the thickness highly variable and irregular, resulting in what is best described as a partly transposed bedding, at least in its left half. In addition, the lens displays inclined asymmetric folds, truncated bedding, shear planes, and recumbent folds in the lower left tip. Overlying the right deformed sand lens is the thin layer of matrix-supported, massive diamict (Dmm) and granule lenses (GRmc) described in *section 3*. However, here the matrix-supported diamict can be traced further towards the left (SSW) where it increases considerably in thickness, up to ~40 cm, until it reaches the underlying clast-supported diamict through a diffuse contact. Further towards the left, the diamicts are covered by slumped material, marking the termination of *section 4*. Overlying the matrix-supported diamict and the granule lenses is the continuation of the lime-rich, massive sand (Sm) with horizons of limeclast-bearing, massive fines (Fm) described above for *section 3*. In the left half of the massive sand unit another unit of matrix-supported, massive diamict intrudes from above, drastically reducing the thickness of the massive sand down to ~10 cm. The intruding diamict is homogenous with no evident structural elements. Its upper spatial extent is unknown due to coverage of slumped material.

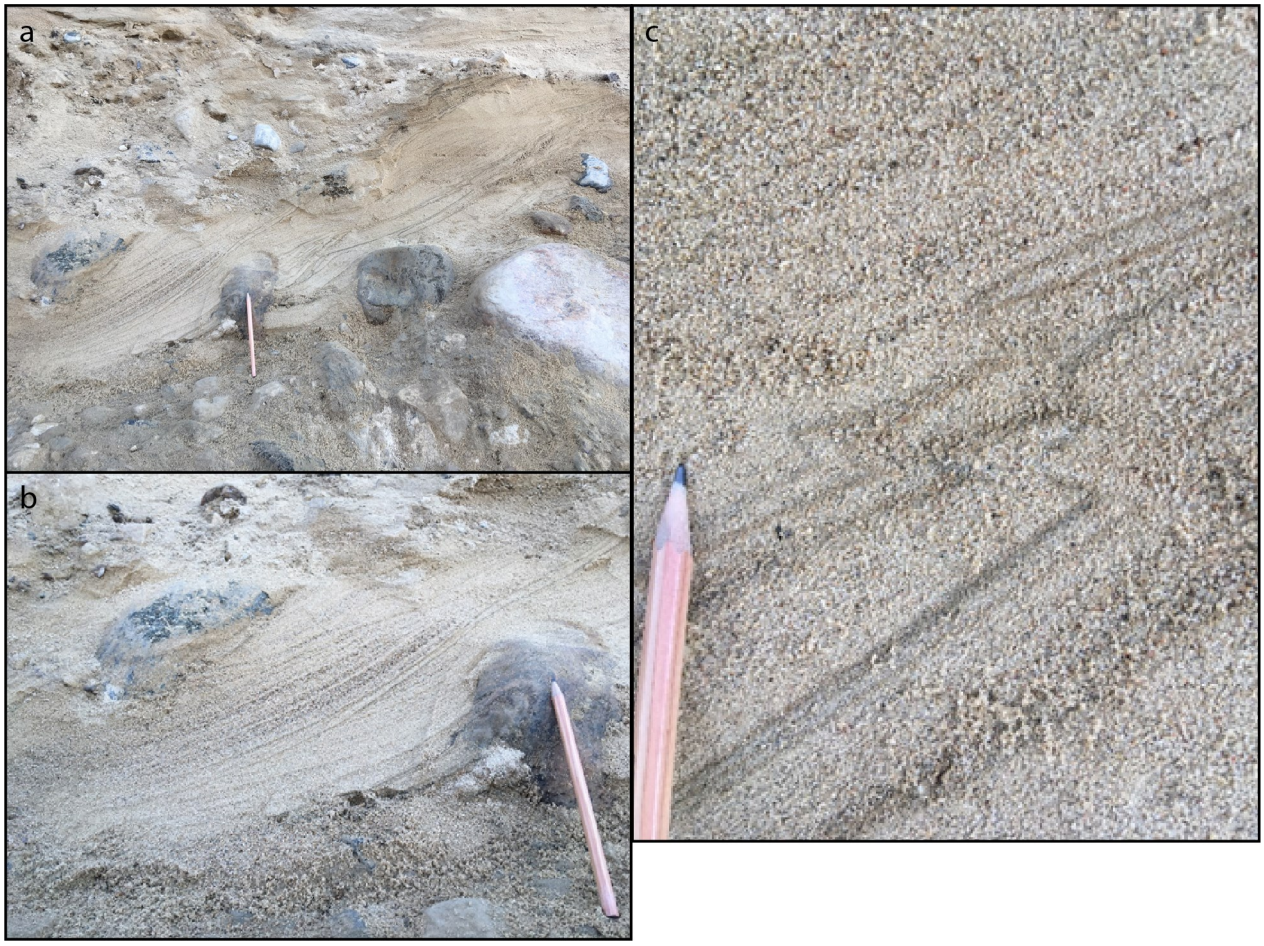

Figure 23: Close up photographs from section 4, see pencil for scale a) Deformed sand lens displaying boudinage structures. b) Truncated bedding and shear planes. c) Asymmetric inclined folds.

4.3 Structural measurements

The characteristic fractures situated within the exposure display clear inherent orientational structures and have therefore been documented through structural measurements. These measurements were recorded throughout the exposure and were subsequently plotted on lower-hemisphere stereonets with equal area (Schmidt net) projections (Allmendinger et al. 2011; Cardozo & Allmendinger 2013). This enables both quantification and visualisation of the structural data, which in turn enables further analysis. Dip-angle, dip-direction, and fracture thickness were recorded within the logged section (Fig. 24), the results of which are presented in traditional pole-to-plane stereonets as both lines and planes (Fig. 25). The major fractures (thickness > 10 mm) display clear trends towards the SW whilst the minor fractures (thickness < 10 mm) are more sporadic, displaying less clear trends towards the SE.

The results of the structural measurements from the logged sections are additionally plotted in modified stereonets (Fig. 24). These stereonets have been modified to show fracture thickness instead of dip-angle. Thus, it is important to be aware that these do not constitute traditional pole-to-plane stereonets (Howarth 1996). These highlight how the major fractures (thickness > 10 mm) almost exclusively dip towards the SW (Fig. 26).

The structural measurements from the readily exposed fracture planes, within the limestone section of the exposure (Fig. 24), are plotted in traditional pole-to-plane stereonets as both lines and planes (Fig. 27). Note that these measurements only contain dip-angle and dip-direction data and do not contain any form of fracture thickness data. This is due to increased bedrock cohesion within the limestone section (Fig. 24), which inhibited accurate measurements of fracture thickness. These stereonets display clear trends towards the SW, with data exclusively plotting within the SW quadrant (Fig. 27).

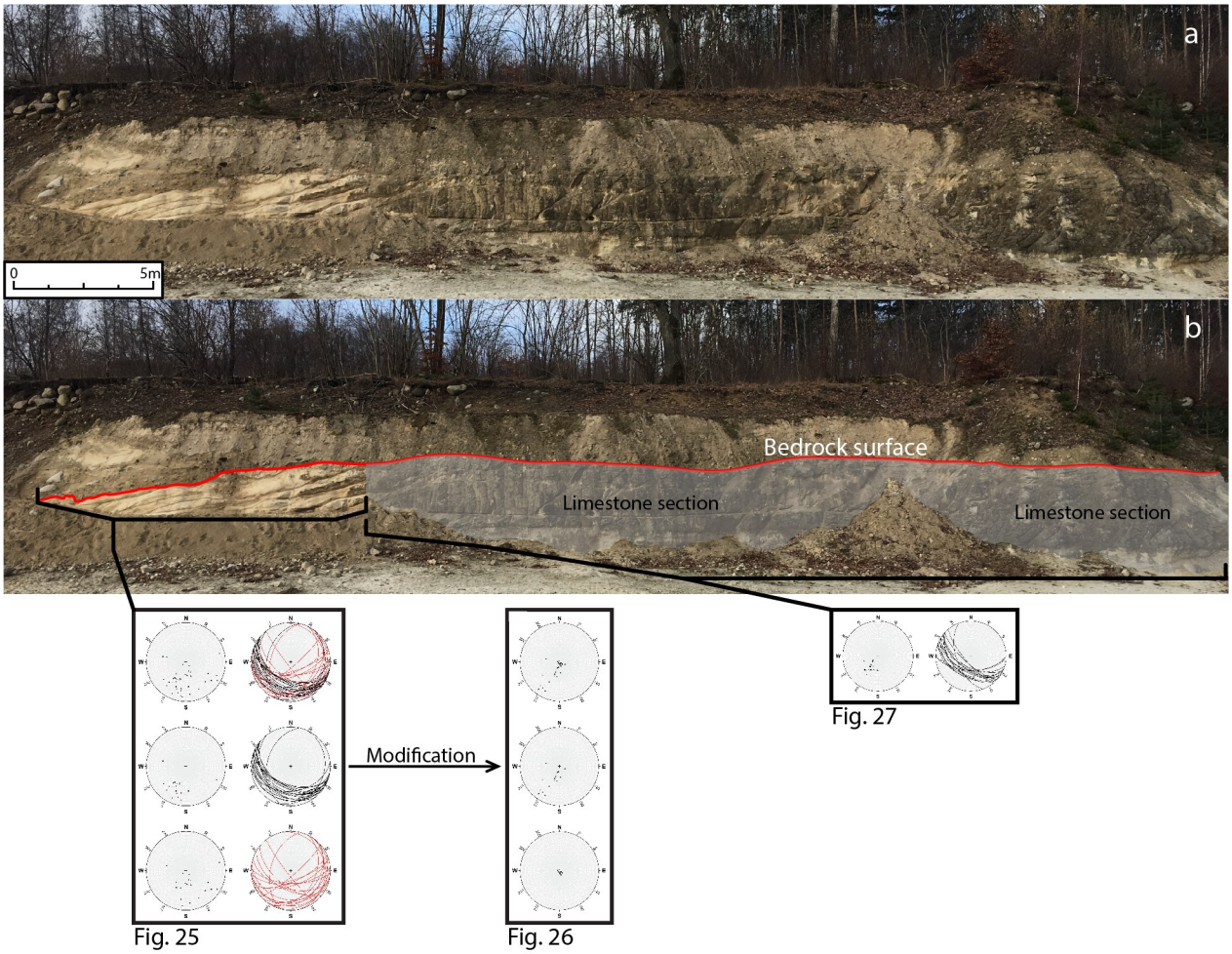

Figure 24: a) Unaltered overview photograph of the exposure. b) Overview photograph of the exposure indicating the sections of structural measurements for the respective stereonets. Measurements from the logged section produced the stereonets presented in Fig. 25, which were subsequently modified, the results of which are presented in the modified stereonets in Fig. 26. Structural measurements of readily exposed fracture planes were conducted within the limestone section, resulting in the stereonets presented in Fig. 27.

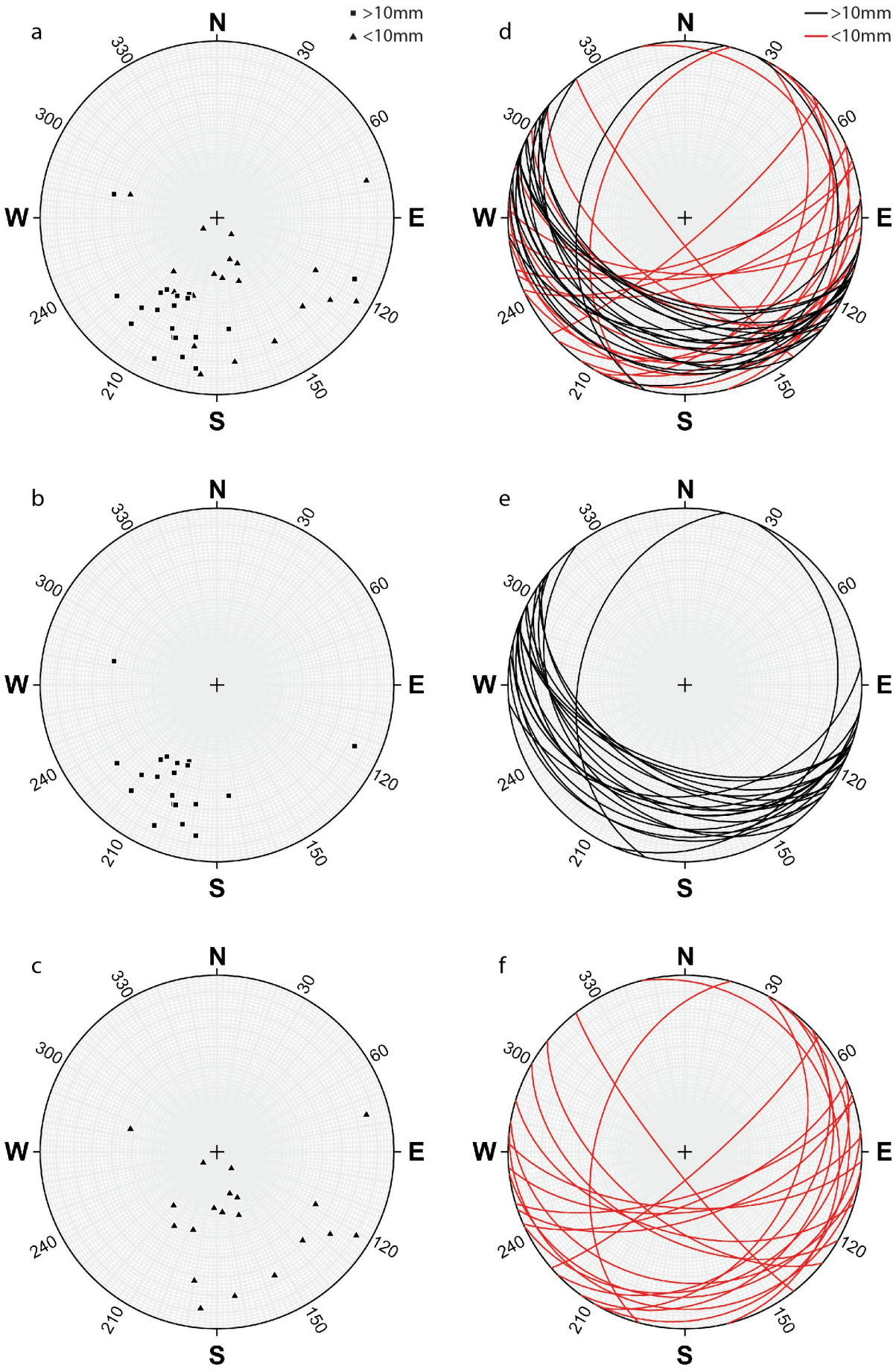

Figure 25: 41 structural measurements of fractures situated within the logged sections of the exposure (Fig. 24). These display dip-angle, dip-direction, and fracture thickness data plotted on lower-hemisphere stereonets with equal area (Schmidt net) projections. a) All fracture measurements plotted as lines. b) Major fractures (thickness > 10 mm) plotted as lines. c) Minor fractures (thickness < 10 mm) plotted as lines. d) All fracture measurements plotted as planes. e) Major fractures (thickness > 10 mm) plotted as planes. f) Minor fractures (thickness < 10 mm) plotted as planes.

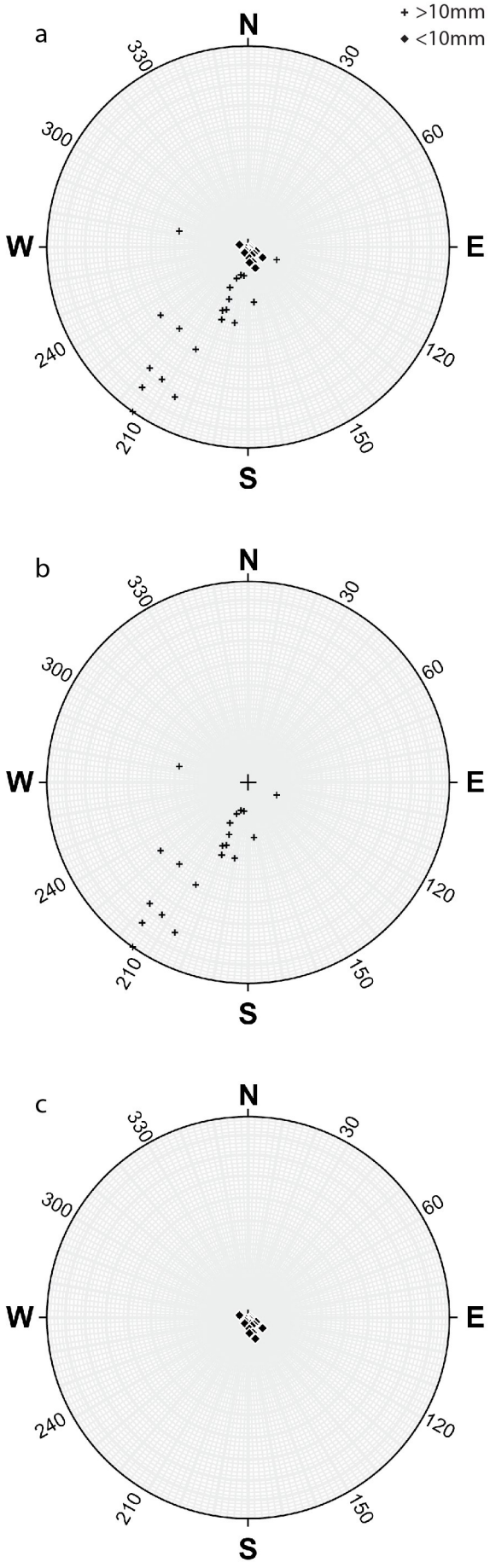

Figure 26: Lower-hemisphere stereonets with equal area (Schmidt net) projections that have been modified to plot dip-direction against fracture thickness instead of dip-angle. The centre point of the stereonets represents a thickness of 0 mm and the circular edge represents a thickness of 100 mm. Thus, it is important to recognise that these do not represent traditional pole-to-plane stereonets. These stereonets plot the same 41 measurements as presented above (Fig. 25). a) All fracture measurements plotted as lines. b) Major fractures (thickness > 10 mm) plotted as lines. c) Minor fractures (thickness < 10 mm) plotted as lines.

4.4 Clast shape & roundness analysis

Five samples (*CS1*-5) were collected from the diamicts for clast shape and roundness analysis. The exact sampling locations are marked out in the logs for *section 1*, *2*, *3*, and *4* (chapter 4.2). From these samples, clast shape and respective roundness distributions were measured and plotted in ternary diagrams and as frequency distributions, respectively. In addition, these were used to produce the respective C_{40}-, RA-, and RWR-indices for each sample. The results from these operations are presented below (Fig. 28). C_{40}-indices range between 4 and 12%, RA-indices range between 2 and 14%, and RWR-indices range between 24 and 40%. The results of the respective samples were plotted in the RA/RWR-C_{40}-covariance diagrams presented below (Fig. 29). The occurrence of striae, facets, and bullet-shapes were noted for each clast within the samples and the results are presented as frequency distributions (Fig. 30). Between the samples, the percentage of clasts showing striae range between 48 and 66%, clasts displaying facets range between 44 and 90%, and clasts displaying bullet-shapes range between 32 and 44%.

4.5 Fine gravel analysis

Nine fine gravel analysis samples were obtained from the logged section of the exposure, three from the diamicts (Di1-3), three from the granule lenses (GR1-3), and three from the fracture fill sediments within the limestone (FF1-3). The sampling locations are marked in the logs for *section 1*, *2*, *3*, and *4* (chapter 4.2). The results of the fine gravel analysis are presented below (Fig. 31). All samples predominantly consist of *crystalline* material and *Cretaceous/Tertiary limestone* but the distributions vary within the sets of samples, i.e. within the diamict, fracture fill, and granule samples, respectively.

5 Interpretations of results

The results presented above are interpreted and discussed in the following sections. First, the results of the *Sedimentology* are addressed with regards to the fracture network and the overlying unconsolidated sediments, respectively. Subsequently, the interpretations of the stereonets produced from the *Structural measurements* are analysed. Following this, the respective interpretations of the *Clast shape & roundness analysis* and *Fine gravel analysis* will be brought forth. Due to the interwoven nature of the results and subsequent interpretations, cross-referencing between these categories are utilised where required. Furthermore, all interpretations are made within the context of the *Geomorphological mapping*, which have already been interpreted with regards to mapped landforms and structures (chapter 4.1).

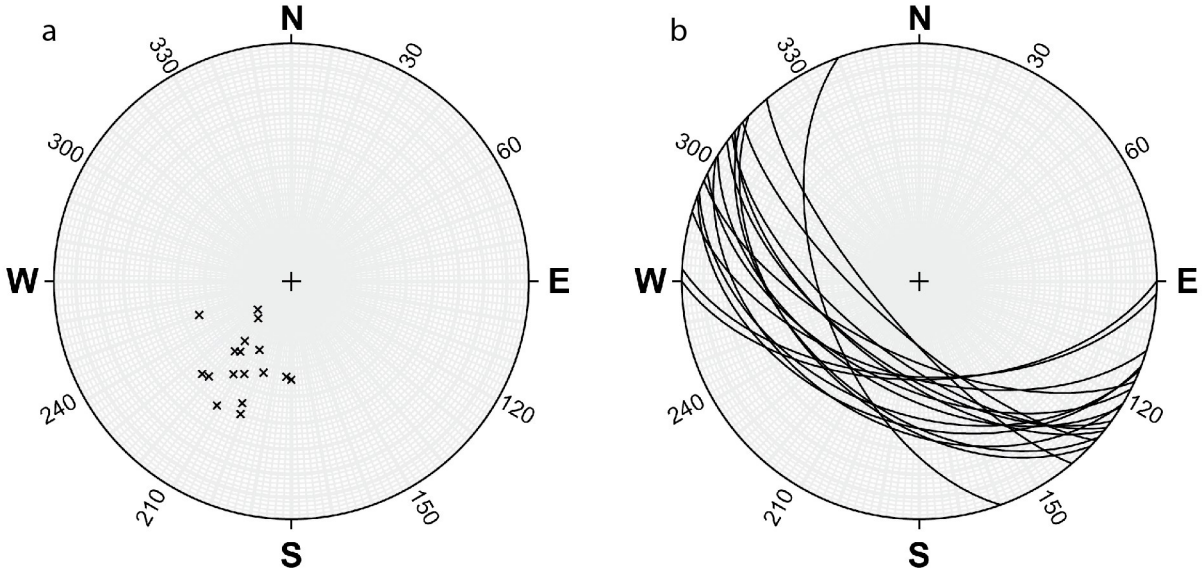

Figure 27: Dip-angle and dip-direction measurements of exposed fracture planes from the limestone section (Fig. 24) plotted on lower-hemisphere stereonets with equal area (Schmidt net) projections. a) Fractures plotted as lines. b) Fractures plotted as planes.

5.1 Sedimentology - *Section 1*, *2*, *3*, & *4*

Even though four different logs have been produced, this has only been done for practical representation and qualitative preservation purposes. The different log sections, *section 1*, *2*, *3*, and *4*, still constitute a continuous exposure and will therefore be addressed in unison regarding their related interpretations that are presented below.

5.1.1 Fracture network

The most prominent set of features within the exposure is the sediment-filled fracture network that runs through the entirety of the exposure. This network also permeates throughout the limestone section to the right (N) of the logged sections (Fig. 12) as well as the other readily visible parts of the quarry. The relative orientation and progression of these fractures and the characteristics of the fracture fill (FF) display striking similarities with the hydrofractures and clastic injections described by authors such as Phillips et al. (2013) and Ravier et al. (2015). Therefore, these fractures are interpreted as hydrofractures, which indicates that the area has been subjected to elevated porewater pressures at the point of formation (Evans et al. 2006a; van der Meer et al. 2009; Phillips et al. 2013). In addition, the abundance and interrelation of these hydrofractures seem to indicate that they make up a part of a greater hydrofracture system that likely reaches beyond the extent of the quarry. How widespread this network is and if it is constrained to the limestone bedrock is currently unknown. As earlier findings suggest, the hydrofractures have been infilled with clastic sediments in conjunction with the fracturing process (Phillips et al. 2013). This has resulted in clearly defined, liberated, lenticular pieces/slabs of bedrock. The nature of the infilled material is coherent with the findings of Phillips et al. (2013) and Ravier et al. (2015) who describe hydrofractures in which fines dominate the fracture tips and fracture walls, whilst coarser material constitute the central wider sections of fractures, all of which is indicative of hydrofracturing with concomitant infill of loose sediments. Alternatively, the fractures could have already been predefined within the bedrock, and the clastic sediment infill injected along such planes of weakness without concomitant hydrofracturing (Phillips et al. 2013). However, this explanation is deemed unlikely due to the characteristic orientation of the fracture network, as indicated by the structural measurements (Fig. 25-27), and the clear correlation with the palaeo-ice-flow directional indicators evident in the sediment landform record reviewed above (Fig. 10).

Furthermore, the characteristic sediment-filled pockets situated throughout the fracture network constitute a distinct feature of unknown genesis. From their visual appearance, they lack the characteristic angular, elongate shapes typically associated with hydrofracturing (Phillips et al. 2013). Rather, it looks like they have formed through radial dissolution/ disintegration of the surrounding bedrock walls. However, the sorting of clast sizes seen within these pockets still seems to indicate influence of sediment injection as clasts appear to essentially have been pushed to one side (Fig. 20a) (Ravier et al. 2015).

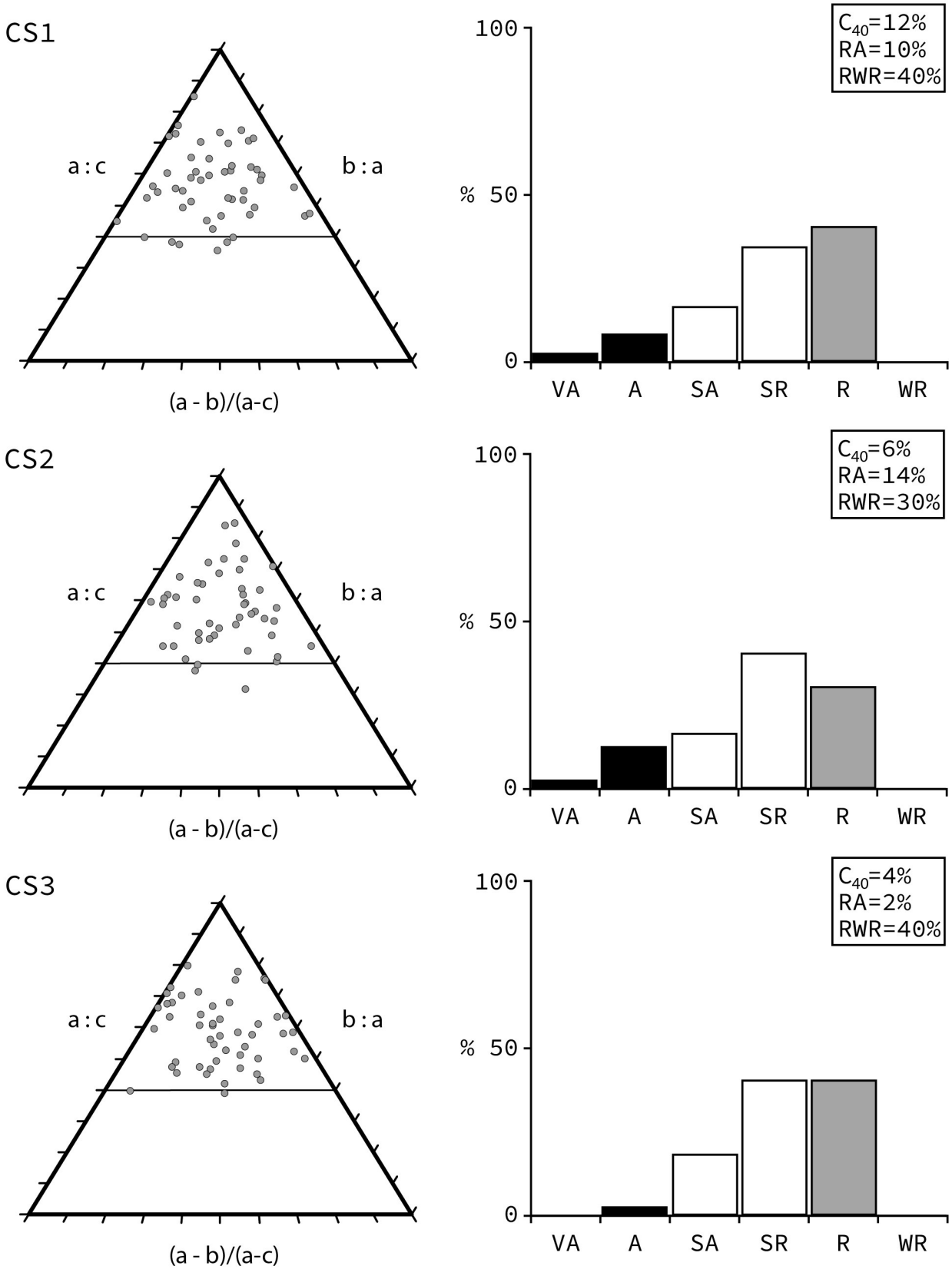
CS1
a:c
b:a
(a - b)/(a-c)
100
% 50
0
VA
A
SA
SR
R
WR
C40=12%
RA=10%
RWR=40%
CS2
a:c
b:a
(a - b)/(a-c)
100
% 50
0
VA
A
SA
SR
R
WR
C40=6%
RA=14%
RWR=30%
CS3
a:c
b:a
(a - b)/(a-c)
100
% 50
0
VA
A
SA
SR
R
WR
C40=4%
RA=2%
RWR=40%

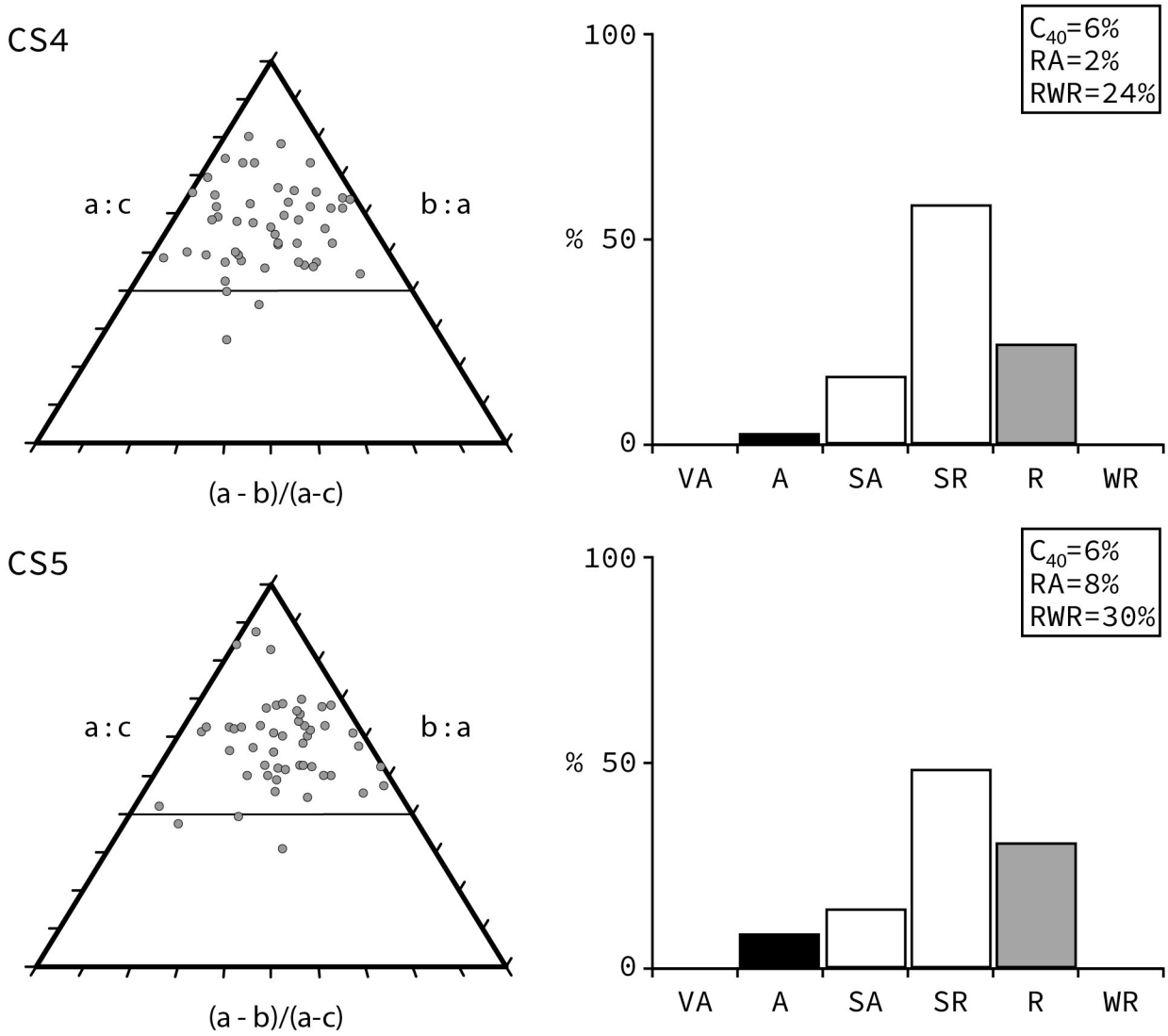

Figure 28: Ternary clast shape diagram and frequency distributions of roundness classes for the respective samples (CS1-5). The resulting C_{40}-, RA-, and RWR-indices are presented for each sample.

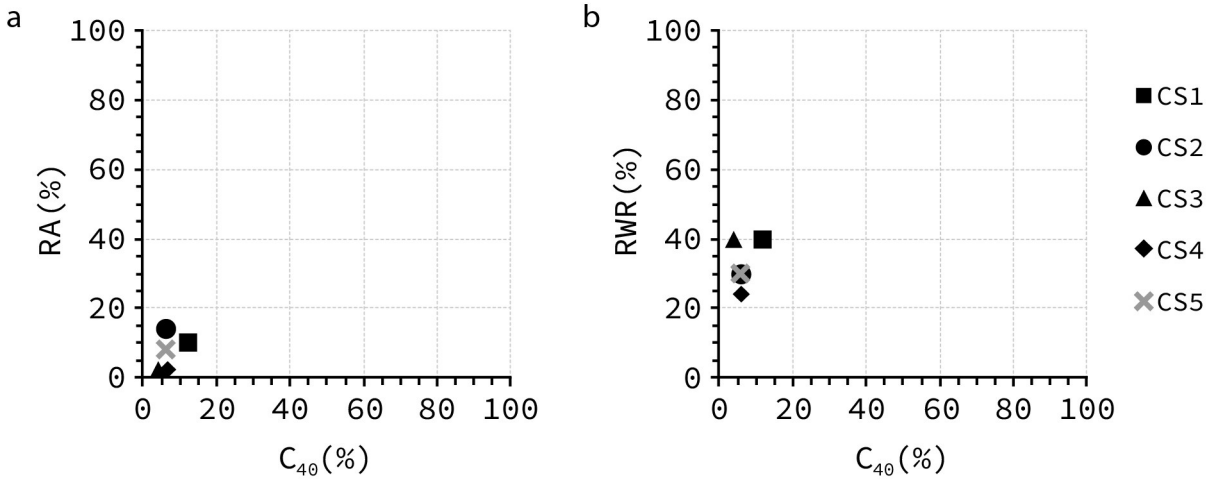

Figure 29: a) RA-C_{40}-covariance diagram in which the clast shape samples are plotted (CS1-5). b) RWR-C_{40}-covariance diagram in which the clast shape samples are plotted (CS1-5).

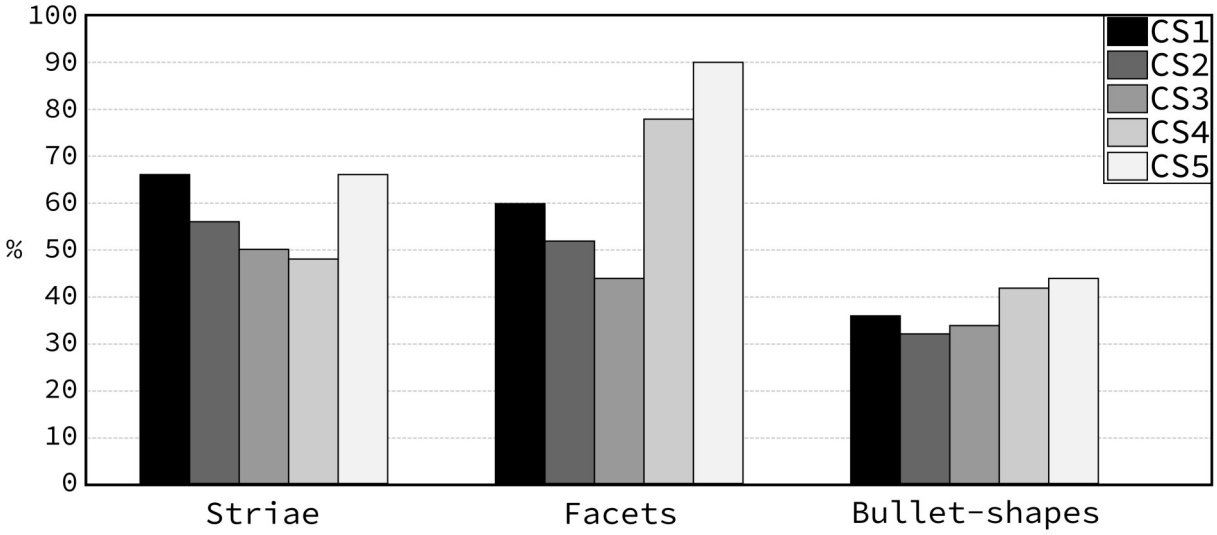

Figure 30: Distributions of surface textures for the respective clast shape samples (CS1-5).

5.1.2 Unconsolidated sediments

The loose sediments overlying the bedrock display prominent features indicative of glacitectonites (Benn & Evans 1996; Evans et al. 2006b; Benn & Evans 2010). For instance, the laminations of the prominent clasts within the clast-supported, massive diamict (Dcm) indicates attenuation and shear of the material (Roberts & Hart 2005). Interestingly, this lamination is not shared with the matrix-supported, massive diamict (Dmm), potentially indicating that these parts of the diamict have undergone more intense deformation resulting in greater homogenisation (Benn & Evans 1996). Alternatively, the lamination is merely harder to identify in these areas since the matrix-supported diamicts are located towards the edges of the logged part of the exposure. The attenuation of the clast-supported, massive diamict is shared by the lenses of deformed sand (Sd) located throughout the sections, as indicated by their boudinage structures that align with the orientation of the diamict clast lamination. Furthermore, these deformed sand lenses display deformation structures that penetrate and overprint their original sedimentary structures, indicative of a low-strength, high-strain glacitectonite (*Type A*) (Benn & Evans 1996; Evans 2018). This is seen as penetration of diamicts and prominent clasts into the deformed sand lenses and as asymmetric inclined folds, shear planes, and truncated bedding of the lenses (Benn & Evans 1996; Evans & Benn 2014a). Thus, these lenses mark the presence of both brittle and ductile deformation. It is interesting to note that the overlying massive granule lenses (GRmc) do not exhibit as pronounced deformation structures. This is coherent with the findings of authors such as Hart & Roberts (1994), Benn & Evans (1996), Evans (2000), and Roberts & Hart (2005), that present how finer-grained glacitectonite units deform more readily than coarser-grained units due to variations in material response to stress, primarily resulting from contrasts in sediment frictional strength and permeability. Therefore, coarser units form stiffer pods that display streamlined forms that record erosion and deformation of their edges during shear within more rapidly deforming material. This relationship is strikingly similar to that of the massive granule lenses and deformed sand lenses. The evident deformation structures of the massive fines (Fm), such as boudinage structures and fragmented bedding, further support a glacitectonite classification (Benn & Evans 1996; Roberts & Hart 2005).

In summary, the overwhelming glacitectonite imprint points to the material having been deposited in a subglacial setting characterised by high strain (Benn & Evans 1996; Evans et al. 2006b). In addition, deposition within the subglacial realm is given further support by both the structural measurements and the clast shape analysis (chapter 5.2 & 5.3). The two diamicts have likely been incorporated within the glacitectonite as subglacial traction till based on their massive, unsorted structure (Evans et al. 2006a; Evans & Benn 2014a). The lenses of deformed sand and massive granules have likely been incorporated into the subglacial realm as pre-deformational material during ice advances, during which they have deformed into their current state, as indicated by the apparent deformation structures, i.e. boudinage, augen shapes, inclined asymmetric folds, recumbent folds, truncations, and shear planes (Benn & Evans 1996). However, the original characteristics of these lenses are still evident. Despite their poor sorting, they are interpreted to have been deposited in a fluvial environment due to their relatively limited range in grain-size and distinguishable bedding (Evans & Benn 2014a; Möller & Murray 2015). This is also supported by the results of the clast shape and roundness analysis (chapter 5.3). Furthermore, the lime-rich, massive sand (Sm) and massive fines (Fm) with incorporated limeclasts display strik-

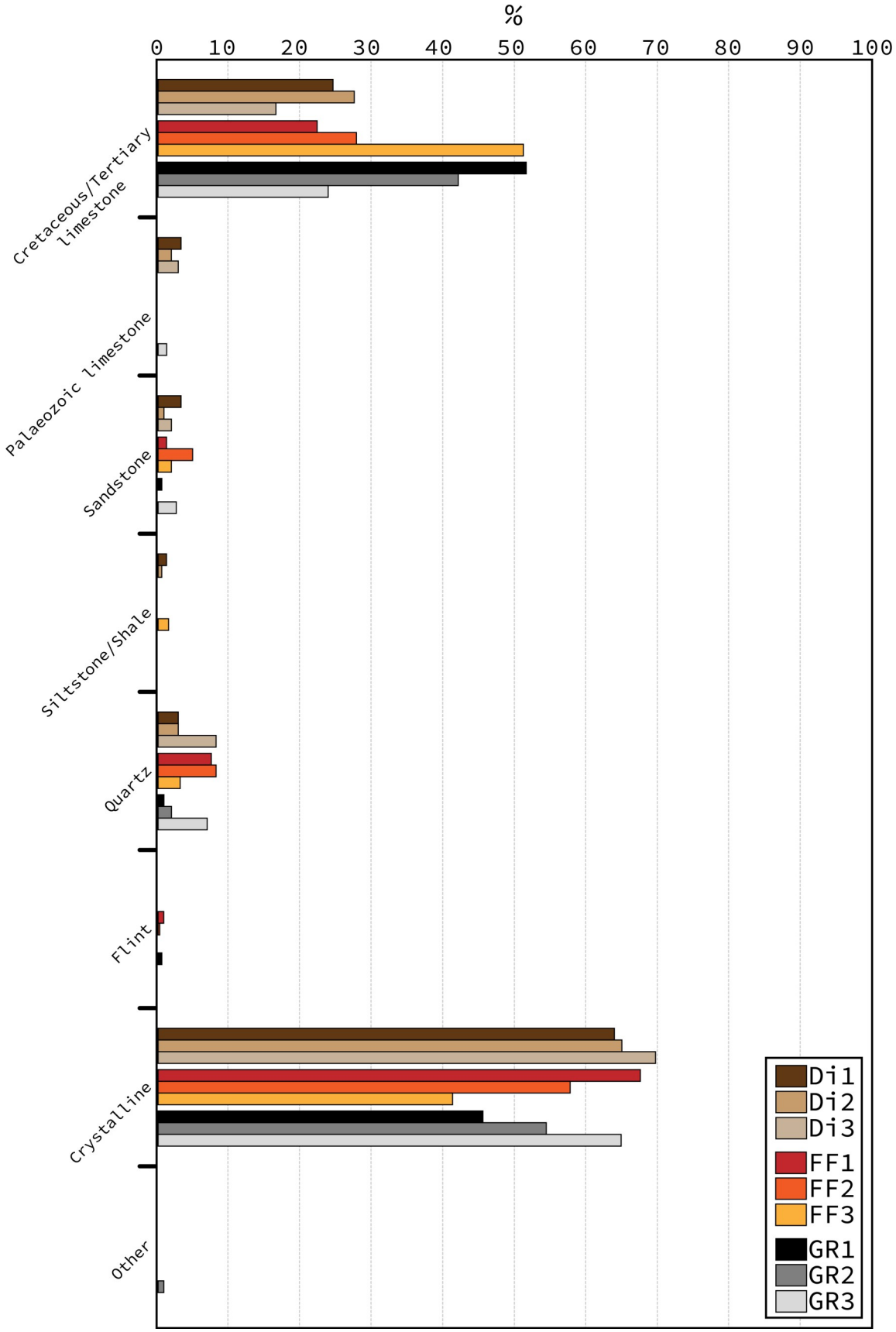

Figure 31: Results of the fine gravel analysis displaying the lithological distributions for the diamict samples (Di1-3), fracture fill samples (FF1-3), and granule samples (GR1-3).

ing similarities to the underlying limestone (Li), based on visual inspection of grain-size distributions and carbonate content. This could indicate that these sediment segments consist of broken-down pieces/slabs of underlying limestone bedrock. This is supported by the presence of belemnite fossils within the clast-supported, massive diamict, which indicates that there has been incorporation of calcareous material into the glacitectonite. Furthermore, the dip of the bedrock surface throughout the logged section of the exposure could indicate the presence of bedrock plucking (Krabbendam & Glasser 2011; Evans et al. 2021), which also would have resulted in incorporation of calcareous material into the glacitectonite. However, further investigation of the lime-rich, massive sand and the limeclasts within the massive fines should be conducted to discern potential relationships with greater certainty.

5.2 Structural measurements

The orientation of the hydrofractures, in the logged sections and the limestone section to the right (N) in the exposure (Fig. 24), display clear trends towards the SW (Fig. 25-27), especially with regards to the major hydrofractures (thickness > 10 mm). The coherency of the hydrofracture orientations with the palaeo-ice-flow presented by Ringberg (1991) (Fig. 6 & 7) as well as the palaeo-ice-flow indicators identified from the geomorphological mapping (Fig. 10) is striking. Since hydrofractures form in response to subglacial pressure conditions (Phillips et al. 2013; Ravier et al. 2015), it is not surprising that these have formed parallel to the palaeo-ice-flow direction since both ice-flow direction and hydrofracture propagation are governed by ice surface slope (Evans et al. 2006b; Cuffey & Paterson 2010; Ravier et al. 2015). This would indicate that the hydrofractures are downwards going (*per descensum*) dykes, rather than upwards going (*per ascensum*) dykes, which in turn suggests that they formed in a subglacial environment (Phillips et al. 2013; Ravier et al. 2015). It is worth mentioning the alignment of the hydrofractures and the orientations of belemnite rostra within the limestone presented by Sandström (2001). Potentially, these internal structures have created favourable conditions for hydrofracture formation as they constitute potential planes or lines of weakness within the limestone (Phillips et al. 2013).

The difference in orientation with regards to the major and minor hydrofractures is worth further attention (Fig. 25). Since hydrofractures form in response to the subglacial pressure-gradient (Cuffey & Paterson 2010; Phillips et al. 2013) the easiest explanation would be that the gradient has been redirected to the SE, as indicated by the orientation of the minor hydrofractures (thickness < 10 mm) (Fig. 25). However, this is not supported by the landforms identified during the geomorphological mapping of the study area or by the findings of Ringberg (1991), with the potential exception of a few streamlined landforms. Alternatively, the major fractures have been choked/sealed with sediments (Phillips et al. 2013), resulting in a redirection of continued fracture propagation towards local low-pressure areas. Another possibility could be that the tensile strength of the igneous material composing the Nävlingeåsen Horst is too great to enable hydrofracture propagation, resulting in a similar redirection towards local low-pressure areas. Furthermore, it is interesting that the minor hydrofractures primarily propagate towards the SE as this area consists of the topographic lowland of the Kristianstad Basin (Fig. 10).

5.3 Clast shape & roundness analysis

The results from the clast shape analysis gave C_{40}-indices ranging from 4 to 12%, RA-indices from 2 to 14%, and RWR-indices from 24 to 40%. As indicated by the low C_{40}-indices, the diamicts consist of predominantly blocky material, indicative of active shaping in the subglacial traction zone (Boulton 1978; Benn & Ballantyne 1993; Lukas et al. 2013). Such shaping seems to have had a large influence which is considered likely due to the location of the study site. The potential transport distances during glaciations would likely result in mature material with low C_{40}-indices (Kleman et al. 2008; Benn 2014a). Furthermore, this is also coherent with the intense deformation structures observed in the glacitectonite.

Comparison to the clast shape analysis results for gneiss control samples presented by Lukas et al. (2013) enable further insight into the transport history of the material (Fig. 32). When comparing the sample envelope for CS1-5 to the gneiss control samples for RA-C_{40}-covariance, they present the strongest correlation to the subglacial control samples (Fig. 32) (Lukas et al. 2013). This suggests that the sampled material has been deposited in a subglacial setting. In addition, the high percentages of facetted, striated, and bullet-shaped clasts (Fig. 30) provides further support for a subglacial deposition (Boulton 1978; Finlayson & Bradwell 2008). If correct, it correlates with the loose sediments in the exposure constituting a glacitectonite as well as the hydrofractures constituting downwards going (*per descensum*) dykes. Contrary, comparison of the sample envelope with the control samples for RWR-C_{40}-covariance does not show a clear correlation with either of the two closest clusters of control samples, neither subglacial nor fluvial (Fig. 32). This could potentially be explained by an intermingling of both processes, or by incorporation of fluvial material into the subglacial system. Such incorporation and entrainment are considered highly likely due to the potential transport distances between the closest ice sheet origin and the location of the study site, as mentioned above (Kleman et al. 2008). Along this path, various lithologies of different genesis have likely been incorporated into the subglacial realm, modifying both RA- and RWR-values. In addition, the results

from the sedimentology (chapter 4.2) indicate that incorporation of pre-deformational sediments has occurred, as indicated by the lenses of deformed sand and massive granules. However, such modification of RA- and RWR-values does raise questions regarding the accuracy and use of this technique for genetic classification in palaeo-glaciated settings. With that said, it is important to be aware that the technique has specifically been designed for use in glaciated environments (Lukas et al. 2013). Nonetheless, the genetic classification corresponds well to those of the sedimentology and structural measurements.

5.4 Fine gravel analysis

The results from the fine gravel analysis enable some interesting observations, both with regards to the overall distribution of lithologies for the different sample sets (Di, FF, & GR) and the internal distributions for the respective lithologies. From the results it is deemed possible that the fracture fill material originates from the overlying diamicts. The overall percentage distributions, predominantly *Cretaceous/Tertiary limestone* and *crystalline* material, are similar for both the diamict and the fracture fill samples (Fig. 31). Furthermore, the fracture fill samples display a noteworthy progression. Sample FF1 is located high up in the fracture and sample FF2 and FF3 are located progressively deeper into their respective fractures (Fig. 14). Thus, the fine gravel analysis indicates that there is an increase in *Cretaceous/Tertiary limestone* material coupled with a decrease in *crystalline* material progressively deeper into the fractures. The wider upper parts of the fractures have likely been exposed to more extensive sediment infill and can also hold more sediments with a greater range of grain-sizes (Phillips et al. 2013; Ravier et al. 2015). In comparison, the deeper parts of the fractures have been exposed to less infill and can hold a more limited range of grain-sizes (Phillips et al. 2013), resulting in less grains of *crystalline* material (Ravier et al. 2015). However, the limestone fraction likely consists of material liberated from the fracture walls rather than having been injected from above. This is probably contributing to the increase of the limestone fraction deeper into the fractures, as the fracture wall material can be incorporated along the entire length of the fractures. Thus, such material would potentially also accumulate further towards the fracture tips. Conversely, other lithologies must be injected from above the bedrock surface, resulting in a gradual decrease of these lithologies further into the fractures due to diminishing fracture thickness and sediment input (Phillips et al. 2013; Ravier et al. 2015). However, it must be pointed out that only three samples have been collected from the fracture fill and the diamicts, so these should only be viewed as potential indicators of the true compositions, and care should be taken with regards to interpretation of the results. The same is true for the granules which display the same overall percentage distributions, predominantly *Cretaceous/Tertiary limestone* and *crystalline* material (Fig. 31). However, the percentages for these samples vary more significantly than those of the fracture fills and diamicts. The coherence of the overall percentage distributions could potentially be attributed to homogenisation during deformation (Benn & Evans 1996; Evans et al. 2006b).

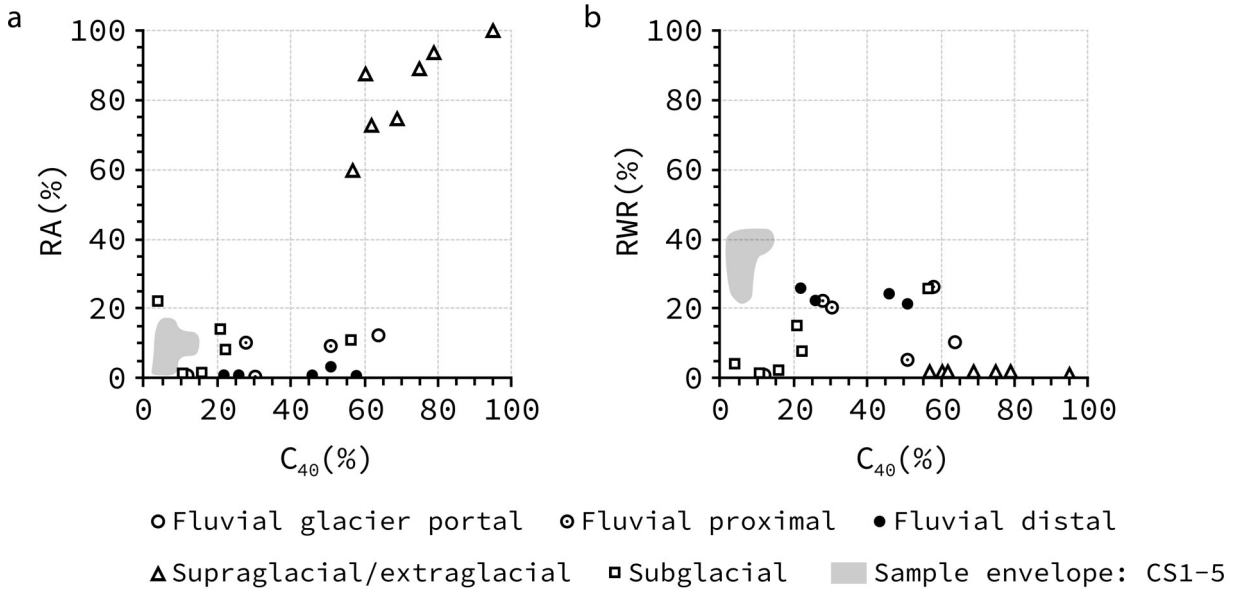

Figure 32: Envelopes of the clast shape samples (CS1-5) in comparison to gneiss control samples of different genesis. a) RA-C_{40}-covariance diagram comparing the sample envelope to the control samples for gneiss lithologies presented by Lukas et al. (2013). b) RWR-C_{40}-covariance diagram comparing the sample envelope to the control samples for gneiss lithologies presented by Lukas et al. (2013).

6 Discussion

In the following chapters, the implications of the results and related interpretations are discussed to address their significance in a wider context. First, the regional geological setting and glacial landforms are examined with regards to their spatial relationships. Thus, this is heavily based on the results and interpretations of the geomorphological mapping in relation to the pre-existing literature. Secondly, this concept is widened to include the spatial relationships of major geological structures and the hydrofracture network by including the results and consequent interpretations attained in relation to conducted field work. Thirdly, these results and interpretations are discussed within the context of the implications of hydrofracturing for bedrock disintegration, plucking, and sediment production. Lastly, areas of complementary research that could add valuable insight to the discussion are addressed.

6.1 Spatial relationships between large geological structures and glacial landforms

The spatial relationships of the esker ridges and the Nävlingeåsen and Linderödsåsen Horsts are of particular interest. As addressed above (chapter 4.1), esker ridges are scarce within the lowlands NE of the horsts whilst appearing upon the horsts further SW, past their steep NE-facing slopes (Fig. 10). This relationship is clearly identified along the Nävlingeåsen Horst where an esker ridge is distinguishably absent in the NE lowland whilst then appearing upon the Nävlingeåsen Horst towards the SW. Upon the horst it can be traced in a SW direction into a lowland where it gives way to a sandur (Fig. 11). The spatial relationship indicates that the horsts may exert a controlling factor regarding esker ridge formation. Potentially, the horsts act as thresholds, producing elevated subglacial water pressures as they block or reduce effective transportation of subglacial water (Benn & Evans 2010; Cuffey & Paterson 2010; Ravier & Buoncristiani 2018; Hewitt & Creyts 2019). This effect could potentially be heightened by the fact that the horsts are positioned roughly perpendicular to the palaeo-ice-flow direction, resulting in a sudden blockade rather than a mere diversion with regards to subglacial water transport, as typical cryostatic potential gradients are disrupted (Ravier & Buoncristiani 2018). Furthermore, these elevated subglacial water pressures could then trigger esker ridge formation upon the horsts as water pressure decreases and the energy is dissipated down-ice past the horst threshold, resulting in a concomitant decrease in carrying capacity and thus deposition of glaciofluvial sediments (Hooke & Fastook 2007; Hebrand & Åmark 2008; Cuffey & Paterson 2010; Livingstone et al. 2015; Beaud et al. 2018; Hewitt & Creyts 2019). Interestingly, the formation of the sandur in the SW lowland, down-ice of the major esker ridge (Fig. 11), could represent how these elevated pressures have decreased to the point where they are insufficient to support esker ridge formation (Gorrell & Shaw 1991; Cuffey & Paterson 2010; Beaud et al. 2018; Hewitt & Creyts 2019). In that case, topography seems to have been a controlling factor for esker ridge formation within the area (Cuffey & Paterson 2010). Furthermore, an alternative reason for the absence of esker ridges, in the lowlands NE of the horsts, could be attributed to sediment reworking below the highest shoreline (Fig. 6) (Ringberg 1991). Wave action below this shoreline could potentially have erased any trace of these esker ridges and related glaciofluvial deposits. However, that begs the question why glaciofluvial deposits have been preserved in the eastern sections of the Kristianstad Basin but not in the aforementioned lowlands (Fig. 6). Thus, if the absence of esker ridges and glaciofluvial sediments is due to sediment reworking beneath the highest shoreline, this would suggest that the reworking has been more intense along the periphery of the Kristianstad Basin compared to in its eastern parts, possibly due to less intense reworking beneath the wave base (Ringberg 1991; Bosence et al. 2003; Hebrand & Åmark 2008). Alternatively, the glaciofluvial deposits along the periphery could originally have been minor in comparison to their eastern counterparts. Another possibility would be that the material has simply been covered by glaciolacustrine sediment when the area was deglaciated. However, mere sedimentation would not erase existing esker ridge topography and can therefore not explain the absence of these ridges in the lowland. Sedimentation could however hide glaciofluvial deposits not accompanied by esker ridges.

6.2 Spatial relationships between large geological structures and the hydrofracture network

In addition to the spatial relationships between large geological structures and esker ridges, the spatial relationship of the hydrofracture network and the Nävlingeåsen Horst is worth further attention. The examined hydrofracture network is located just downslope of the horst's steep NE-slope. As discussed above, the horst has potentially acted as a threshold, resulting in elevated subglacial water pressures and esker ridge formation. The same circumstances of elevated water pressures have previously been determined as a crucial factor for hydrofracture generation (Boulton et al. 1993; Le Heron & Etienne 2005; Phillips et al. 2013; Ravier et al. 2015; Ravier & Buoncristiani 2018). Thus, as for the esker ridges addressed above, topography could have constituted a controlling, if not determining, factor for hydrofracture generation and propagation. Furthermore, if the increase in topography by the Nävlingeåsen Horst has

resulted in the increased subglacial water pressures required for hydrofracturing (Evans et al. 2006b; Phillips et al. 2013; Ravier et al. 2015), it is interesting to note the orientation of the minor hydrofractures post potential sediment choking or redirection due to the Nävlingeåsen Horst as discussed above (chapter 5.2). Although these minor hydrofractures display more diffuse orientations, they still trend towards the lowland area of the Kristianstad Basin (Fig. 10 & 25). Since hydrofractures form in the direction of lower pressure (Evans et al. 2006b; Phillips et al. 2013; Ravier et al. 2015) this would provide further support for a topographical control on hydrofracture propagation and in extension highlight the importance of topography for subglacial pressure dynamics (Cuffey & Paterson 2010; Ravier & Buoncristiani 2018). Furthermore, if topography does exert a control on hydrofracture generation and propagation, hydrofractures could be expected along the NE-slope of the Nävlingeåsen Horst as well as along the NE-slope of the Linderödsåsen Horst.

6.3 Implications of hydrofracturing for bedrock disintegration, plucking, and sediment production

When viewed with a holistic approach, the correlation between the examined hydrofracture network, bedrock structures, sedimentology, and geomorphology yield interesting insights into bedrock liberation, plucking, and sediment production. The bedrock surface in the exposure can be traced semi-horizontally throughout the limestone section until it reaches *section 1* from where it starts to dip towards the SSW. The bedrock surface continues to dip throughout the remaining sections until it is completely covered by slumped material (Fig. 12). In addition, the orientation of the dipping limestone surface is predominantly shared by the major hydrofractures within the limestone (Fig. 26). Furthermore, the sedimentological investigation of the exposure revealed that the dipping limestone surface is sporadically overlain by a layer of fracture fill indicative of hydrofracturing (Phillips et al. 2013; Ravier et al. 2015). Thus, the evidence suggests that a former continuous semi-horizontal limestone surface has been disintegrated through hydrofracturing, forming liberated lenticular pieces/slabs of bedrock that have been plucked by the overriding ice, leaving behind a dipping limestone surface that aligns with the palaeo-ice-flow direction of the area (Fig. 10) (Ringberg 1991; Evans et al. 1998; Evans et al. 2021). The occurrence of lime-rich, massive sand and loosely consolidated limeclasts within the overlying glacitectonite provides further support for the occurrence of plucking of the underlying limestone. In extension, this would indicate that hydrofracturing could be an important process regarding bedrock disintegration, plucking, and early-stage sediment production, potentially constituting a crucial role within the till continuum and the evolution of landscapes (Evans et al. 2006b; Juliusson 2019; Evans et al. 2021). A potentially limiting factor for the importance of hydrofracturing in this regard concerns the environments in which they have been documented. To the authors knowledge, the only studies explicitly documenting hydrofracturing have either been conducted within exposures of loose sediments or sedimentary bedrock. Hence, the recent findings of Krabbendam et al. (2021) are of particular interest, as they describe sediment injections reminiscent of those produced during hydrofracturing, but within crystalline basement rocks.

6.4 Areas of complementary research

As experienced throughout the mapping of the study area, the potential capabilities and further research regarding geomorphological mapping are vast. The implementations of modern geographical information systems and new high-resolution datasets enable new insights to be gained from areas previously thought to have been exhausted of research potential. Thus, further mapping and related field studies should be conducted with regards to the streamlined landforms and the terminal moraines identified during the geomorphological mapping procedure. This would undoubtedly provide valuable insights regarding the spatial distribution and precise genetic classification of these landforms, as well as contribute to the geological database of eastern Scania.

There are still more investigations that would be of interest to conduct regarding the study site as well. Primarily, it would be interesting to discern if the lime-rich, massive sand and the limeclast-bearing, massive fines consist of disintegrated and/or altered pieces/slabs of liberated limestone that originates from the underlying bedrock. This could likely be revealed through microscopy and/or geochemical analysis of the respective units. The results of such analyses would likely put forth compelling evidence that would either support or reject the importance of hydrofracturing regarding early-stage plucking and sediment production.

Furthermore, defining the true extent of the hydrofracture network would provide valuable insights into the prerequisite conditions for hydrofracture generation and propagation. If the hydrofracture network is constrained to the NE down-slope area of the Nävlingeåsen Horst, this would suggest that the topography has played a vital role, if not controlled, the build-up of subglacial water pressures and subsequent hydrofracturing (Phillips et al. 2013; Ravier & Buoncristiani 2018). Contrary, if the fracture network could be traced either further NE into the Kristianstad Basin or SW into the Nävlingeåsen Horst, it would indicate that the topography has not been responsible for the generation of the hydrofracture system. Furthermore, this would shed light on the possibility of

hydrofracturing in different bedrock environments. So far, investigations of hydrofractures have been restricted to environments of loose sediments and sedimentary bedrock (van der Meer et al. 2009; Phillips et al. 2013; Ravier et al. 2015). If the examined fracture network would be shown to continue into the adjacent crystalline environment of the Nävlingeåsen Horst, this would indicate that hydrofracturing is not limited to sedimentary environments. However, the investigation of hydrofractures in bedrock environments is heavily dependent on pre-existing exposures, which greatly reduces the investigation potential of these processes. Therefore, it must be mentioned that additional limestone quarries are situated along the NE slope of the Nävlingeåsen Horst, both at Ignaberga and at Önnestad (Fig. 3). The spatial distribution of these quarries does present a promising and potentially unique set of circumstances for further hydrofracture investigation and analysis. If utilised, such investigations could provide valuable insights into the spatial extent of the examined hydrofracture system, hydrofracture dynamics, and the implications of hydrofracturing for bedrock disintegration, plucking, and sediment production. It is worth mentioning that the limestone quarry located at Ignaberga has been observed to display features indicative of hydrofracturing (Fig. 33).

7 Conclusions

This study has presented a detailed investigation of the implications of ice-bedrock dynamics through detailed geomorphological, sedimentological, and structural analysis in relation to geological findings at the limestone quarry, commonly known as *Kalkan*, situated at Ullstorp, Scania, southern Sweden. The key findings of the study are presented below.

The palaeo-ice-flow direction towards the SW presented by Ringberg (1991) is given additional support. The number of streamlined landforms seem to be more extensive than previously documented. In addition, the spatial relationships between the Nävlingeåsen and Linderödsåsen Horsts, esker ridges, and hydrofractures indicate that the horsts have exerted an important control on subglacial water pressures. This indicates that topography can exert a controlling, if not determining, factor for both esker ridge and hydrofracture generation and propagation.

The fracture system within the investigated exposure is determined to have been formed in a subglacial environment through hydrofracturing with concomitant sediment infill originating from the overlying glacitectonite. The predominant SW orientation of the major hydrofractures has formed in response to the palaeo-pressure-gradient which aligns with the palaeo-ice-flow direction. The more sporadic orientations of the minor hydrofractures have likely formed post sediment choking of the major fractures. This resulted in minor fracture propagation towards local low-pressure areas, out of which the lowland of the Kristianstad Basin constituted the dominant low-pressure area.

Lastly, hydrofracturing seems to play a vital role with regards to the liberation of bedrock at the study site. This liberation has in turn enabled plucking of liberated bedrock pieces/slabs and subsequent breakdown and incorporation into the overlying glacitectonite. Thus, hydrofracturing seems to exert a control on bedrock liberation, plucking, and sediment production. In extension, this indicates that hydrofracturing plays a more important role within the till continuum and within landscape evolution than previously acknowledged. In summary, the examined exposure constitutes a snapshot of early-stage bedrock plucking due to hydrofracture-induced bedrock liberation.

8 Acknowledgements

First, I want to thank my advisor Sven Lukas for his continuous support, encouragement, and invaluable input throughout this project. A sincere thank you goes out to the personnel of the geo-library whose support has been nothing short of remarkable. Thanks goes out to Henrik Langkjaer and Ingrid Olsson whose generosity enabled the field work for this study. Lastly, thank you to the members of KMDG whose valuable input has increased the quality of this thesis.

- Much appreciated

Figure 33: Exposures within the limestone quarry at Ignaberga, Scania, southern Sweden, where fractures indicative of hydrofracturing have been observed.

9 References

Agrell, H., 1976: The highest coastline in south-eastern Sweden. *Boreas 5*, 143-154. doi: 10.1111/j.1502-3885.1976.tb00258.x

Allmendinger, R. W., Cardozo, N. & Fisher, D. M., 2011: *Structural geology algorithms: Vectors and tensors*. Cambridge University Press.

Åmark, M., 1986: Clastic dikes formed beneath an active glacier. *GFF 108*, 13-20. doi: 10.1080/11035898609453740

Ballantyne, C. K., 1982: Aggregate clast form characteristics of deposits near the margins of four glaciers in the Jotunheimen Massif, Norway. *Norsk Geografisk Tidsskrift - Norwegian Journal of Geography 36*, 103-113. doi: 10.1080/00291958208621960

Barrett, P. J., 1980: The shape of rock particles, a critical review. *Sedimentology 27*, 291-303. doi: 10.1111/j.1365-3091.1980.tb01179.x

Bates, C. D., Coxon, P. & Gibbard, P. L., 1978: A NEW METHOD FOR THE PREPARATION OF CLAY-RICH SEDIMENT SAMPLES FOR PALYNOLOGICAL INVESTIGATION. *New Phytologist 81*, 459-463. doi: 10.1111/j.1469-8137.1978.tb02651.x

Beaud, F., Flowers, G. E. & Venditti, J. G., 2018: Modeling sediment transport in ice-walled subglacial channels and its implications for esker formation and proglacial sediment yields. *Journal of Geophysical Research: Earth Surface 123*, 3206-3227.

Benn, D. I., 1992: The genesis and significance of 'hummocky moraine': Evidence from the Isle of Skye, Scotland. *Quaternary Science Reviews 11*, 781-799. doi: 10.1016/0277-3791(92)90083-k

Benn, D. I. 2014a: Clast morphology. *In A Practical Guide to the Study of Glacial Sediments*, 78-92. Routledge,

Benn, D. I. 2014b: Macrofabric. *In A Practical Guide to the Study of Glacial Sediments*, 107-128. Routledge,

Benn, D. I. & Ballantyne, C. K., 1993: The description and representation of particle shape. *Earth Surface Processes and Landforms 18*, 665-672. doi: https://doi.org/10.1002/esp.3290180709

Benn, D. I. & Ballantyne, C. K., 1994: Reconstructing the transport history of glacigenic sediments: a new approach based on the co-variance of clast form indices. *Sedimentary Geology 91*, 215-227. doi: 10.1016/0037-0738(94)90130-9

Benn, D. I. & Evans, D. J. A., 1996: The interpretation and classification of subglacially-deformed materials. *15*, 23-52. doi: 10.1016/0277-3791(95)00082-8

Benn, D. I. & Evans, D. J. A., 2010: *Glaciers & glaciation*. Hodder Education.

Bernhardson, M. & Alexanderson, H., 2017: Early Holocene dune field development in Dalarna, central Sweden: A geomorphological and geophysical case study. *Earth Surface Processes and Landforms 42*, 1847-1859. doi: 10.1002/esp.4141

Bosence, D. W., Angela, L., Church, K. D., Flint, S. S., Howell, J. A., Wilson, R. C. L., Dan, W., Kevin, D. & John, A., 2003: *The sedimentary record of sea-level change*. Cambridge University Press.

Boulton, G. S., 1978: Boulder shapes and grain-size distributions of debris as indicators of transport paths through a glacier and till genesis. *Sedimentology 25*, 773-799. doi: 10.1111/j.1365-3091.1978.tb00329.x

Boulton, G. S., 1986: Push-moraines and glacier-contact fans in marine and terrestrial environments. *Sedimentology 33*, 677-698. doi: 10.1111/j.1365-3091.1986.tb01969.x

Boulton, G. S., Dobbie, K. E. & Zatsepin, S., 2001: Sediment deformation beneath glaciers and its coupling to the subglacial hydraulic system. *Quaternary International 86*, 3-28. doi: https://doi.org/10.1016/S1040-6182(01)00048-9

Boulton, G. S., Slot, T., Blessing, K., Glasbergen, P., Leijnse, T. & Van Gijssel, K., 1993: Deep circulation of groundwater in overpressured subglacial aquifers and its geological consequences. *Quaternary Science Reviews 12*, 739-745.

Boyce, J. I. & Eyles, N., 2000: Architectural element analysis applied to glacial deposits: Internal geometry of a late Pleistocene till sheet, Ontario, Canada. *GSA Bulletin 112*, 98-118. doi: 10.1130/0016-7606(2000)112<98:AEAATG>2.0.CO;2

Brook, M. S. & Lukas, S., 2012: A revised approach to discriminating sediment transport histories in glacigenic sediments in a temperate alpine environment: a case study from Fox Glacier, New Zealand. *Earth Surface Processes and Landforms 37*, 895-900. doi: 10.1002/esp.3250

Cardozo, N. & Allmendinger, R. W., 2013: Spherical projections with OSXStereonet. *Computers & Geosciences 51*, 193-205. doi: 10.1016/j.cageo.2012.07.021

Chandler, B. M. P., Lovell, H., Boston, C. M., Lukas, S., Barr, I. D., Benediktsson, Í. Ö., Benn, D. I., Clark, C. D., Darvill, C. M., Evans, D. J. A., Ewertowski, M. W., Loibl, D., Margold, M., Otto, J.-C., Roberts, D. H., Stokes, C. R., Storrar, R. D. & Stroeven, A. P., 2018: Glacial geomorphological mapping: A review of approaches and frameworks for best practice. *Earth-Science Reviews 185*, 806-846. doi: 10.1016/j.earscirev.2018.07.015

Clark, C. D., Hughes, A. L. C., Greenwood, S. L., Spagnolo, M. & Ng, F. S. L., 2009: Size and shape characteristics of drumlins, derived from a large sample, and associated scaling laws. *Quaternary Science Reviews 28*, 677-692. doi: 10.1016/j.quascirev.2008.08.035

Clarke, G. K. C., 1987: A short history of scientific investigations on glaciers. *Journal of Glaciology 33*, 4-24. doi: 10.3189/s0022143000215785

Cuffey, K. M. & Paterson, W. S. B., 2010: *The physics of glaciers*. Academic Press.

De Geer, G., 1889: *Beskrifning till kartbladet Bäckaskog*. Stockholm**.**

Derbyshire, E., Mcgown, A. & Radwan, A., 1976: 'Total'fabric of some till landforms. *Earth Surface Processes 1***,** 17-26.

Dowdeswell, M. T., 1993: Water throughflow and the physical effects of deformation on sedimentary glacier beds: Murray, T; Dowdeswell, J A J Geophys ResV97, NB6, June 1992, P8993–9002. *International Journal of Rock Mechanics and Mining Sciences & Geomechanics Abstracts 30***,** A89. doi: https://doi.org/10.1016/0148-9062(93)90854-7

Dowling, T. P. F., Spagnolo, M. & Möller, P., 2015: Morphometry and core type of streamlined bedforms in southern Sweden from high resolution LiDAR. *Geomorphology 236***,** 54-63. doi: 10.1016/j.geomorph.2015.02.018

Drake, L. D., 1970: Rock texture; an important factor for clast shape studies. *Journal of Sedimentary Research 40***,** 1356-1361. doi: 10.1306/74d721b2-2b21-11d7-8648000102c1865d

Ehlers, J., 1979: Fine Gravel Analyses after the Dutch Method as Tested out on Ristinge Klint, Denmark. *Bulletin of the Geological Society of Denmark 27*.

Ely, J. C., Clark, C. D., Spagnolo, M., Hughes, A. L. C. & Stokes, C. R., 2018: Using the size and position of drumlins to understand how they grow, interact and evolve. *Earth Surface Processes and Landforms 43***,** 1073-1087. doi: 10.1002/esp.4241

Erlström, M. & Gabrielson, J., 1986: The Upper Cretaceous clastic deposits of Ullstorp, Kristianstad basin, Scania. *Geologiska Föreningen i Stockholm Förhandlingar 107***,** 241-254. doi: 10.1080/11035898609453063

Erlström, M., Gabrielson, J. & Sveriges Geologiska, U., 1992: *Petrology, fossil composition and depositional history of the Ignaberga limestone, Kristianstad basin, Scania*. Sveriges geologiska undersökning (SGU)**.**

Evans, D. J. & Benn, D. I., 2014a: *A practical guide to the study of glacial sediments*. Routledge**.**

Evans, D. J. A., 2000: A gravel outwash/deformation till continuum, skalafellsjokull, iceland. *Geografiska Annaler: Series A, Physical Geography 82***,** 499-512. doi: 10.1111/j.0435-3676.2000.00137.x

Evans, D. J. A., 2018: *Till : a Glacial Process Sedimentology*. Wiley Blackwell**.** 390 pp.

Evans, D. J. A. & Benn, D. I. 2014b: Facies description and the logging of sedimentary exposures. *In A Practical Guide to the Study of Glacial Sediments*, 11-51. Routledge,

Evans, D. J. A. & Hansom, J. D., 1996: The Edinburgh Castle crag-and-tail. *Scottish Geographical Magazine 112***,** 129-131. doi: 10.1080/14702549608554461

Evans, D. J. A., Phillips, E. R. & Atkinson, N., 2021: Glacitectonic rafts and their role in the generation of Quaternary subglacial bedforms and deposits. *Quaternary Research***,** 35. doi: doi:10.1017/qua.2021.11

Evans, D. J. A., Phillips, E. R., Hiemstra, J. F. & Auton, C. A., 2006a: Subglacial till: Formation, sedimentary characteristics and classification. *Earth-Science Reviews 78***,** 115-176. doi: 10.1016/j.earscirev.2006.04.001

Evans, D. J. A., Phillips, E. R., Hiemstra, J. F. & Auton, C. A., 2006b: Subglacial till: Formation, sedimentary characteristics and classification. *Earth Science Reviews 78***,** 115-176. doi: 10.1016/j.earscirev.2006.04.001

Evans, D. J. A., Rea, B. R. & Benn, D. I., 1998: Subglacial deformation and bedrock plucking in areas of hard bedrock. *Glacial Geology and Geomorphology***,** 1–25.

Evans, D. J. A. & Twigg, D. R., 2002: The active temperate glacial landsystem: a model based on Breiðamerkurjökull and Fjallsjökull, Iceland. *Quaternary Science Reviews 21***,** 2143-2177. doi: 10.1016/s0277-3791(02)00019-7

Finlayson, A. G. & Bradwell, T., 2008: Morphological characteristics, formation and glaciological significance of Rogen moraine in northern Scotland. *Geomorphology 101***,** 607-617. doi: 10.1016/j.geomorph.2008.02.013

Glasser, N. F. & Bennett, M. R., 2004: Glacial erosional landforms: origins and significance for palaeoglaciology. *Progress in Physical Geography: Earth and Environment 28***,** 43-75. doi: 10.1191/0309133304pp401ra

Gorrell, G. & Shaw, J., 1991: Deposition in an esker, bead and fan complex, Lanark, Ontario, Canada. *Sedimentary Geology 72***,** 285-314. doi: 10.1016/0037-0738(91)90016-7

Graham, D. J. & Midgley, N. G., 2000: GRAPHICAL REPRESENTATION OF PARTICLE SHAPE USINGTRIANGULAR DIAGRAMS: AN EXCEL SPREADSHEET METHOD. *Earth Surface Processes and Landforms 25***,** 1473–1477. doi: 10.1002/1096-9837(200012)25:13

Hadding, A., 1927: *The pre-quaternary sedimentary rocks of Sweden*. Gleerup**.**

Hart, J. K., 1994: Till fabric associated with deformable beds. *Earth Surface Processes and Landforms 19***,** 15-32.

Hart, J. K. & Roberts, D. H., 1994: Criteria to distinguish between subglacial glaciotectonic and glaciomarine sedimentation, I. Deformation styles and sedimentology. *Sedimentary Geology 91***,** 191-213. doi: 10.1016/0037-0738(94)90129-5

Hebrand, M. & Åmark, M., 2008: Esker formation and glacier dynamics in eastern Skane and adjacent areas, southern Sweden. *Boreas 18***,** 67-81. doi: 10.1111/j.1502-3885.1989.tb00372.x

Hewitt, I. J. & Creyts, T. T., 2019: A Model for the Formation of Eskers. *Geophysical Research Letters 46***,** 6673-6680. doi: 10.1029/2019gl082304

Hewitt, K., 1967: Ice-Front Deposition and the Seasonal Effect: A Himalayan Example. *Transactions of the Institute of British Geographers***,** 93. doi: 10.2307/621374

Holmes, C. D., 1941: Till fabric. *Geological Society of America Bulletin 52*, 1299-1354. doi: 10.1130/gsab-52-1299

Hooke, R. L. & Fastook, J., 2007: Thermal conditions at the bed of the Laurentide ice sheet in Maine during deglaciation: implications for esker formation. *Journal of Glaciology 53*, 646-658. doi: 10.3189/002214307784409243

Howarth, R. J., 1996: History of the stereographic projection and its early use in geology. *Terra Nova 8*, 499-513. doi: 10.1111/j.1365-3121.1996.tb00779.x

Juliusson, O., 2019: Impacts of subglacial processes on underlying bedrock. *Dissertations in Geol ogy at Lund University*, No. 573, 24 pp. 15 hp (15 ECTS credits).

Karlsson, S. V., 1879: *Beskrifning till kartbladet Linderöd*. Stockholm.

Kleman, J., Stroeven, A. P. & Lundqvist, J., 2008: Patterns of Quaternary ice sheet erosion and deposition in Fennoscandia and a theoretical framework for explanation. *Geomorphology 97*, 73-90. doi: 10.1016/j.geomorph.2007.02.049

Knight, J., 2019: The geomorphology and sedimentology of eskers in north-central Ireland. *Sedimentary Geology 382*, 1-24. doi: 10.1016/j.sedgeo.2019.01.003

Krabbendam, M. & Glasser, N. F., 2011: Glacial erosion and bedrock properties in NW Scotland: Abrasion and plucking, hardness and joint spacing. *Geomorphology 130*, 374-383. doi: https://doi.org/10.1016/j.geomorph.2011.04.022

Krabbendam, M., Palamakumbura, R., Arnhardt, C. & Hall, A., 2021: Rock fracturing by subglacial hydraulic jacking in basement rocks, eastern Sweden: the role of beam failure. *GFF*. doi: 10.1080/11035897.2021.1939776

Krüger, J. & Kjaer, K. H., 2008: A data chart for field description and genetic interpretation of glacial diamicts and associated sediments…with examples from Greenland, Iceland, and Denmark. *Boreas 28*, 386-402. doi: 10.1111/j.1502-3885.1999.tb00228.x

Lantmäteriet, n.d.: Geodata för forskning, utbildning och kulturverksamheter. Retrieved 1/02/2021, from https://www.lantmateriet.se/sv/Kartor-och-geografisk-information/geodataprodukter/geodata-for-forskning-utbildning-och-kulturverksamheter/.

Larsen, E. & Mangerud, J., 1992: Subglacially formed clastic dykes. *SGU Ca 81*, 163-170.

Le Heron, D. P. & Etienne, J. L., 2005: A complex subglacial clastic dyke swarm, Sólheimajökull, southern Iceland. *Sedimentary Geology 181*, 25-37. doi: 10.1016/j.sedgeo.2005.06.012

Lee, J. R. & Phillips, E. R., 2008: Progressive soft sediment deformation within a subglacial shear zone; a hybrid mosaic-pervasive deformation model for middle Pleistocene glaciotectonised sediments from eastern England. *Quaternary Science Reviews 27*, 1350-1362. doi: 10.1016/j.quascirev.2008.03.009

Lidmar-Bergström, K., Elvhage, C. & Ringberg, B., 1991: Landforms in Skåne, South Sweden. *Geografiska Annaler: Series A, Physical Geography 73*, 61-91. doi: 10.1080/04353676.1991.11880333

Lindström, A., 1877: *Beskrifning till kartbladet "Hessleholm"*. Stockholm.

Livingstone, S. J., Storrar, R. D., Hillier, J. K., Stokes, C. R., Clark, C. D. & Tarasov, L., 2015: An ice-sheet scale comparison of eskers with modelled subglacial drainage routes. *Geomorphology 246*, 104-112. doi: 10.1016/j.geomorph.2015.06.016

Lukas, S., Benn, D. I., Boston, C. M., Brook, M., Coray, S., Evans, D. J. A., Graf, A., Kellerer-Pirklbauer, A., Kirkbride, M. P., Krabbendam, M., Lovell, H., Machiedo, M., Mills, S. C., Nye, K., Reinardy, B. T. I., Ross, F. H. & Signer, M., 2013: Clast shape analysis and clast transport paths in glacial environments; a critical review of methods and the role of lithology. *Earth-Science Reviews 121*, 96-116. doi: 10.1016/j.earscirev.2013.02.005

Lukas, S., Graf, A., Coray, S. & Schlüchter, C., 2012: Genesis, stability and preservation potential of large lateral moraines of Alpine valley glaciers – towards a unifying theory based on Findelengletscher, Switzerland. *Quaternary Science Reviews 38*, 27-48. doi: 10.1016/j.quascirev.2012.01.022

Lundegren, A., 1934: *Kristianstadsområdets kritbildningar : Die Kreidebildungen des Kristianstadsgebietes*. Norstedt.

Mannerfelt, C. M. S., 1949: Marginal drainage channels as indicators of the gradients of Quaternary ice caps. *Geografiska Annaler 31*, 194-199.

Meriano, M. & Eyles, N., 2009: Quantitative assessment of the hydraulic role of subglaciofluvial interbeds in promoting deposition of deformation till (Northern Till, Ontario). *Quaternary Science Reviews 28*, 608-620. doi: 10.1016/j.quascirev.2008.08.034

Möller, P. & Dowling, T. P. F., 2015: The importance of thermal boundary transitions on glacial geomorphology; mapping of ribbed/hummocky moraine and streamlined terrain from LiDAR, over Småland, South Sweden. *GFF 137*, 252-283. doi: 10.1080/11035897.2015.1051736

Möller, P. & Murray, A. S., 2015: Drumlinised glaciofluvial and glaciolacustrine sediments on the Småland peneplain, South Sweden – new information on the growth and decay history of the Fennoscandian Ice Sheets during MIS 3. *Quaternary Science Reviews 122*, 1-29. doi: 10.1016/j.quascirev.2015.04.025

Ottesen, D. & Dowdeswell, J. A., 2006: Assemblages of submarine landforms produced by tidewater glaciers in Svalbard. *Journal of Geophysical Research 111*. doi: 10.1029/2005jf000330

Pérez, F. L., 1986: Talus texture and particle morphology in a North Andean paramo. *Zeitschrift für Geomorphologie*, 15-34.

Persson, M., 2000: *Beskrivning till jordartskartan 3E Karlshamn NV= Description to the quaternary map 3E Karlshamn NW*. Sveriges Geologiska Undersökning.

Phillips, E., Everest, J. & Reeves, H., 2013: Micromorphological evidence for subglacial multiphase sedimentation and deformation during overpressurized fluid flow associated with hydrofracturing. *Boreas 42*, 395-427. doi: 10.1111/j.1502-3885.2012.00261.x

Piotrowski, J. A., 2007: *Groundwater Under Ice Sheets and Glaciers*. John Wiley and Sons. 50 -60 pp.

Piotrowski, J. A. & Kraus, A. M., 1997: Response of sediment to ice-sheet loading in northwestern Germany: effective stresses and glacier-bed stability. *Journal of Glaciology 43*, 495-502. doi: 10.3189/S0022143000035103

Piotrowski, J. A., Larsen, N. K. & Junge, F. W., 2004: Reflections on soft subglacial beds as a mosaic of deforming and stable spots. *Quaternary Science Reviews 23*, 993-1000. doi: 10.1016/j.quascirev.2004.01.006

Powers, M. C., 1953: A New Roundness Scale for Sedimentary Particles. *SEPM Journal of Sedimentary Research Vol. 23*. doi: 10.1306/d4269567-2b26-11d7-8648000102c1865d

Ravier, E., Buoncristiani, J.-F., Menzies, J., Guiraud, M. & Portier, E., 2015: Clastic injection dynamics during ice front oscillations: A case example from Sólheimajökull (Iceland). *Sedimentary Geology 323*, 92-109. doi: 10.1016/j.sedgeo.2015.04.013

Ravier, E. & Buoncristiani, J. F. 2018: Glaciohydrogeology. *In*, 431-466. Elsevier,

Ringberg, B., 1991: *Jordartskartan [Kartografiskt material]. 3D Kristianstad SO. Beskrivning till jordartskartan Kristianstad SO = Description to the quaternary map Kristianstad SO*. Sveriges Geologiska Undersökning, Uppsala.

Roberts, D. H. & Hart, J. K., 2005: The deforming bed characteristics of a stratified till assemblage in north East Anglia, UK: investigating controls on sediment rheology and strain signatures. *Quaternary Science Reviews 24*, 123-140. doi: 10.1016/j.quascirev.2004.03.004

Sandström, O., 2001: Depositional environment of the Campanian (Upper Cretaceous) strata at Maltesholm, Scania, southern Sweden. *GFF 123*, 51-54. doi: 10.1080/11035890101231051

Sharp, M., 1984: Annual Moraine Ridges at Skàlafellsjökull, South-East Iceland. *Journal of Glaciology 30*, 82-93. doi: 10.3189/s0022143000008522

Smalley, I. J. & Unwin, D. J., 1968: The Formation and Shape of Drumlins and their Distribution and Orientation in Drumlin Fields. *Journal of Glaciology 7*, 377-390. doi: 10.3189/s0022143000020591

Smith, M. J., Rose, J. & Booth, S., 2006: Geomorphological mapping of glacial landforms from remotely sensed data: An evaluation of the principal data sources and an assessment of their quality. *Geomorphology 76*, 148-165. doi: 10.1016/j.geomorph.2005.11.001

Sneed, E. D. & Folk, R. L., 1958: Pebbles in the Lower Colorado River, Texas a Study in Particle Morphogenesis. *The Journal of Geology 66*, 114-150. doi: 10.1086/626490

Spagnolo, M., Clark, C. D., Hughes, A. L. C. & Dunlop, P., 2011: The topography of drumlins; assessing their long profile shape. *Earth Surface Processes and Landforms 36*, 790-804. doi: 10.1002/esp.2107

Stokes, C. R., Spagnolo, M. & Clark, C. D., 2011: The composition and internal structure of drumlins: Complexity, commonality, and implications for a unifying theory of their formation. *Earth-Science Reviews 107*, 398-422. doi: 10.1016/j.earscirev.2011.05.001

Storrar, R. D., Stokes, C. R. & Evans, D. J. A., 2013: A map of large Canadian eskers from Landsat satellite imagery. *Journal of Maps 9*, 456-473. doi: 10.1080/17445647.2013.815591

Todd, B. J., Valentine, P. C., Longva, O. & Shaw, J., 2007: Glacial landforms on German Bank, Scotian Shelf: evidence for Late Wisconsinan ice-sheet dynamics and implications for the formation of De Geer moraines. *Boreas 36*, 148-169. doi: 10.1111/j.1502-3885.2007.tb01189.x

Van Der Meer, J. J. M., Kjaer, K. H. & Krueger, J., 1999: Subglacial water-escape structures and till structures, Slettjokull, Iceland. *JQS. Journal of Quaternary Science 14*, 191-205.

Van Der Meer, J. J. M., Kjær, K. H., Krüger, J., Rabassa, J. & Kilfeather, A. A., 2009: Under pressure: clastic dykes in glacial settings. *Quaternary Science Reviews 28*, 708-720. doi: https://doi.org/10.1016/j.quascirev.2008.07.017

Van Der Meer, J. J. M., Menzies, J. & Rose, J., 2003: Subglacial till: the deforming glacier bed. *Quaternary Science Reviews 22*, 1659-1685. doi: https://doi.org/10.1016/S0277-3791(03)00141-0

Tidigare skrifter i serien ”Examensarbeten i Geologi vid Lunds universitet”:

574. Sartell, Anna, 2019: Metamorphic paragenesis and P-T conditions in garnet amphibolite from the Median Segment of the Idefjorden Terrane, Lilla Edet. (15 hp)
575. Végvári, Fanni, 2019: Vulkanisk inverkan på klimatet och atmorsfärcirkulationen: En litterarurstudie som jämför vulkanism på låg respektive hög latitud. (15 hp)
576. Gustafsson, Jon, 2019: Petrology of platinum-group element mineralization in the Koillismaa intrusion, Finland. (45 hp)
577. Wahlquist, Per, 2019: Undersökning av mindre förkastningar för vattenuttag i sedimentärt berg kring Kingelstad och Tjutebro. (15 hp)
578. Gaitan Valencia, Camilo Esteban, 2019: Unravelling the timing and distribution of Paleoproterozoic dyke swarms in the eastern Kaapvaal Craton, South Africa. (45 hp)
579. Eggert, David, 2019: Using Very-Low-Frequency Electromagnetics (VLF-EM) for geophysical exploration at the Albertine Graben, Uganda - A new CAD approach for 3D data blending. (45 hp)
580. Plan, Anders, 2020: Resolving temporal links between the Högberget granite and the Wigström tungsten skarn deposit in Bergslagen (Sweden) using trace elements and U-Pb LA-ICPMS on complex zircons. (45 hp)
581. Pilser, Hannes, 2020: A geophysical survey in the Chocaya Basin in the central Valley of Cochabamba, Bolivia, using ERT and TEM. (45 hp)
582. Leopardi, Dino, 2020: Temporal and genetical constraints of the Cu-Co Vena-Dampetorp deposit, Bergslagen, Sweden. (45 hp)
583. Lagerstam Lorien, Clarence, 2020: Neck mobility versus mode of locomotion – in what way did neck length affect swimming performance among Mesozoic plesiosaurs (Reptilia, Sauropterygia)? (45 hp)
584. Davies, James, 2020: Geochronology of gneisses adjacent to the Mylonite Zone in southwestern Sweden: evidence of a tectonic window? (45 hp)
585. Foyn, Alex, 2020: Foreland evolution of Blåisen, Norway, over the course of an ablation season. (45 hp)
586. van Wees, Roos, 2020: Combining luminescence dating and sedimentary analysis to derive the landscape dynamics of the Velická Valley in the High Tatra Mountains, Slovakia. (45 hp)
587. Rettig, Lukas, 2020: Implications of a rapidly thinning ice-margin for annual moraine formation at Gornergletscher, Switzerland. (45 hp)
588. Bejarano Arias, Ingrid, 2020: Determination of depositional environment and luminescence dating of Pleistocene deposits in the Biely Váh valley, southern foothills of the Tatra Mountains, Slovakia. (45 hp)
589. Olla, Daniel, 2020: Petrografisk beskrivning av Prekambriska ortognejser i den undre delen av Särvskollan, mellersta delen av Skollenheten, Kaledonska orogenen. (15 hp)
590. Friberg, Nils, 2020: Är den sydatlantiska magnetiska anomalin ett återkommande fenomen? (15 hp)
591. Brakebusch, Linus, 2020: Klimat och väder i Nordatlanten-regionen under det senaste årtusendet. (15 hp)
592. Boestam, Max, 2020: Stränder med erosion och ackumulation längs kuststräckan Trelleborg - Abbekås under perioden 2007 -2018. (15 hp)
593. Agudelo Motta, Laura Catalina, 2020: Methods for rockfall risk assessment and estimation of runout zones: A case study in Gothenburg, SW Sweden. (45 hp)
594. Johansson, Jonna, 2020: Potentiella nedslagskratrar i Sverige med fokus på Östersjön och östkusten. (15 hp)
595. Haag, Vendela, 2020: Studying magmatic systems through chemical analyses on clinopyroxene - a look into the history of the Teno ankaramites, Tenerife. (45 hp)
596. Kryffin, Isidora, 2020: Kan benceller bevaras över miljontals år? (15 hp)
597. Halvarsson, Ellinor, 2020: Sökande efter nedslagskratrar i Sverige, med fokus på avtryck i berggrunden. (15 hp)
598. Jirdén, Elin, 2020: Kustprocesser i Arktis – med en fallstudie på Prins Karls Forland, Svalbard. (15 hp)
599. Chonewicz, Julia, 2020: The Eemian Baltic Sea hydrography and paleoenvironment based on foraminiferal geochemistry. (45 hp)
600. Paradeisis-Stathis, Savvas, 2020: Holocene lake-level changes in the Siljan Lake District – Towards validation of von Post’s drainage scenario. (45 hp)
601. Johansson, Adam, 2020: Groundwater flow modelling to address hydrogeological response of a contaminated site to remediation measures at Hjortsberga, southern Sweden. (15 hp)
602. Barrett, Aodhan, 2020: Major and trace element geochemical analysis of norites in the Hakefjorden Complex to constrain magma source and magma plumbing systems. (45 hp)
603. Lundqvist, Jennie, 2020: ”Man fyller det

med information helt enkelt": en fenomenografisk studie om studenters upplevelse av geologisk tid. (45 hp)

604. Zachén, Gabriel, 2020: Classification of four mesosiderites and implications for their formation. (45 hp)
605. Viðarsdóttir, Halla Margrét, 2020: Assessing the biodiversity crisis whitin the Triassic-Jurassic boundary interval using redox sensitive trace metals and stable carbon isotope geochemistry. (45 hp)
606. Tan, Brian, 2020: Nordvästra Skånes prekambriska geologiska utveckling. (15 hp)
607. Taxopoulou, Maria Eleni, 2020: Metamorphic micro-textures and mineral assemblages in orthogneisses in NW Skåne – how do they correlate with technical properties? (45 hp)
608. Damber, Maja, 2020: A palaeoecological study of the establishment of beech forest in Söderåsen National Park, southern Sweden. (45 hp)
609. Karastergios, Stylianos, 2020: Characterization of mineral parageneses and metamorphic textures in eclogite- to high-pressure granulite-facies marble at Allmenningen, Roan, western Norway. (45 hp)
610. Lindberg Skutsjö, Love, 2021: Geologiska och hydrogeologiska tolkningar av SkyTEM-data från Vombsänkan, Sjöbo kommun, Skåne. (15 hp)
611. Hertzman, Hanna, 2021: Odensjön - A new varved lake sediment record from southern Sweden. (45 hp)
612. Molin, Emmy, 2021: Rare terrestrial vertebrate remains from the Pliensbachian (Lower Jurassic) Hasle Formation on the Island of Bornholm, Denmark. (45 hp)
613. Höjbert, Karl, 2021: Dendrokronologi - en nyckelmetod för att förstå klimat- och miljöförändringar i Jämtland under holocen. (15 hp)
614. Lundgren Sassner, Lykke, 2021: A Method for Evaluating and Mapping Terrestrial Deposition and Preservation Potential-for Palaeostorm Surge Traces. Remote Mapping of the Coast of Scania, Blekinge and Halland, in Southern Sweden, with a Field Study at Dalköpinge Ängar, Trelleborg. (45 hp)
615. Granbom, Johanna, 2021: En detaljerad undersökning av den mellanordoviciska "furudalkalkstenen" i Dalarna. (15 hp)
616. Greiff, Johannes, 2021: Oolites from the Arabian platform: Archives for the aftermath of the end-Triassic mass extinction. (45 hp)
617. Ekström, Christian, 2021: Rödfärgade utfällningar i dammanläggningar orsakade av *G. ferruginea* och *L. ochracea* - Problemstatistik och mikrobiella levnadsförutsättningar. (15 hp)
618. Östsjö, Martina, 2021: Geologins betydelse i samhället och ett första steg mot en geopark på Gotland. (15 hp)
619. Westberg, Märta, 2021: The preservation of cells in biomineralized vertebrate tissues of Mesozoic age – examples from a Cretaceous mosasaur (Reptilia, Mosasauridae). (45 hp)
620. Gleisner, Lovisa, 2021: En detaljerad undersökning av kalkstenslager i den mellanordoviciska gullhögenformationen på Billingen i Västergötland. (15 hp)
621. Bonnevier Wallstedt, Ida, 2021: Origin and early evolution of isopods - exploring morphology, ecology and systematics. (15 hp)
622. Selezeneva, Natalia, 2021: Indications for solar storms during the Last Glacial Maximum in the NGRIP ice core. (45 hp)
623. Bakker, Aron, 2021: Geological characterisation of geophysical lineaments as part of the expanded site descriptive model around the planned repository site for high-level nuclear waste, Forsmark, Sweden. (45 hp)
624. Sundberg, Oskar, 2021: Jordlagerföljden i Höjeådalen utifrån nya borrningar. (15 hp)
625. Sartell, Anna, 2021: The igneous complex of Ekmanfjorden, Svalbard: an integrated field, petrological and geochemical study. (45 hp)
626. Juliusson, Oscar, 2021: Implications of ice-bedrock dynamics at Ullstorp, Scania, southern Sweden. (45 hp)

LUNDS UNIVERSITET

Geologiska institutionen
Lunds universitet
Sölvegatan 12, 223 62 Lund